Influence of porosity on fatigue of additive manufactured titanium alloy Ti-6Al-4V

Akgun, Emre

Award date:
2023

Awarding institution:
Coventry University

Influence of porosity on fatigue of additive manufactured titanium alloy Ti-6Al-4V

by

Emre Akgun

December 2022

A thesis submitted in partial fulfilment of the University's requirements for the Degree of Doctor of Philosophy

Certificate of Ethical Approval

Applicant:	Emre Akgun
Project Title:	Critical defect size in additive manufactured metallic components - development of structural integrity assessment methods through novel experimentation and computer modelling

This is to certify that the above named applicant has completed the Coventry University Ethical Approval process and their project has been confirmed and approved as Low Risk

Date of approval:	12 Apr 2021
Project Reference Number:	P121515

Acknowledgements

This work was undertaken at TWI Ltd as part of the National Structural Integrity Research Centre (NSIRC) programme and was partially funded by the Lloyd's Register Foundation and Coventry University; hence my sincerest thanks to everyone involved in NSIRC.

First and foremost, I would like to thank my academic supervisor Prof. Xiang Zhang for her support, guidance, thoughtful comments, and being very generous with her time throughout this work. Afterwards, I would also like to thank my industrial supervisors Dr. Matthew Doré and Dr. Yanhui Zhang for their time, feedback, and more specifically introducing me to the replica method and providing technical discussions when I needed. Then, I would like to thank Katri Kakko of EOS Finland Oy and Miriam Rau of EOS GmbH for being interested in my project and manufacturing the samples, it is suffice to say without their help majority of the experimental work wouldn't have been possible.

Almost every PhD student faces some kind of adversity during their project, and my case was no exception. Although facing a global pandemic in the middle of my work was daunting, I would like to thank everyone involved for keeping the project moving. Especially, Marcus Young with the organisation when my lab access was restricted, Ramin Taheri for finalising the surface preparations of remaining fatigue samples, Craig Moss and Jerry Godden for assisting me with fatigue testing, Dr. Tristan Lowe for conducting the X-ray Computed Tomography for my remaining samples. At this point, I would like to thank my fellow NSIRC students as well for their collegiality.

Finally, I would like to thank my wife, Merve, for her understanding when I shared my interest in pursuing a PhD and for her support when I eventually resigned from my full-time position to follow this path. Last but not least, I am forever grateful to my parents for providing me the educational foundation that made it possible in the first place to pursue a higher degree.

Abstract

Process-induced defects have been identified as one of the principal failure sources in metal additive manufacturing (AM) under cyclic loading; yet, understanding how they impact fatigue behaviour, such as S-N curves, fatigue crack growth rates remains open. In this work, the high-cycle fatigue behaviour under constant amplitude, axial loading was studied for an AM titanium alloy Ti-6Al-4V that fails from sub-mm size, porosity type defects. More specifically, the dispersion of fatigue life due to porosity and the propagation behaviour of cracks initiated from pores were investigated.

Two different AM processes, namely wire+arc additive manufacturing and laser powder-bed fusion, were used to manufacture titanium alloy Ti-6Al-4V used in this work. A trade-off was made by working with process-induced defects, e.g. defect morphologies were representative of real case scenarios, but the dimensions of defects were uncontrolled. A targeted experimental programme was developed to concentrate on the influence of defects by circumventing other parameters that might impact the fatigue life such as the surface roughness, build direction and more. Size and spatial distribution of process-induced defects were measured using a laboratory scale X-ray Computed Tomography prior to fatigue testing. Load-controlled fatigue testing was conducted by repeating tests at the selected stress levels in order to obtain statistically significant data. Furthermore, fatigue crack growth rates were measured for cracks initiating directly from surface pores using the replica technique. After each fatigue test, the crack initiating pore size was quantified by analysing the fracture surface using a scanning electron microscope. The experimental results were analysed both from a linear elastic fracture mechanics perspective and a total life perspective using the local elastic stresses in the vicinity of a pore. Key findings are summarised below.

A popular approach to evaluate defect criticality is assuming a volumetric defect as a planar crack by projecting its area to the plane perpendicular to the applied load direction. This planar crack is then assessed using a Kitagawa-Takahashi diagram or similar since cracks at the sub-mm scale could grow below the threshold value of stress intensity factor range (ΔK_{th}). It was found that the analogy of assuming pores as cracks was lost after a certain transition size and fatigue life reduction saturated despite the increase of crack initiating pore diameter roughly by a factor of four.

Total fatigue life of AM Ti-6Al-4V could vary up to three orders of magnitude for nominally similar test specimens, as seen in the exploratory literature studies. Defects are considered as one of the causes of this scatter and in this work, defect location, e.g. embedded or surface, was found to be the dominant factor rather than the defect size. In fact, within a same defect category, such as the surface pores, the scatter of fatigue life due to the variation in crack initiating defect size was less than a conventional manufactured Ti-6Al-4V, where the scatter assumed to be related to the distribution of unfavourably oriented surface grains.

Individual fatigue life stages were also investigated by following surface cracks initiated from pores using the replica technique. First detected cracks were less than 50 μm length and occupied roughly 50% of the total fatigue life. This suggests that the crack initiation stage was significant and it should be accounted in fatigue life prediction approaches, noting that the measurements were limited to surface observations. During the crack propagation stage, small cracks could grow faster than the long crack growth measurements at the same nominal ΔK value, i.e. the so-called small crack behaviour. Such a behaviour was observed near the threshold region, however, it was less significant compared to conventional manufactured counterparts. Finally, a similitude to long crack growth rates was achieved, when the measured crack size added to the crack initiating pore size.

Keywords

fatigue of defects; small crack behaviour; additive manufacturing; titanium alloys

Dissemination

- Akgun et al., "*Fatigue of wire+arc additive manufactured Ti-6Al-4V in presence of process-induced porosity defects*", IJF 150, September 2021, 106315, https://doi.org/10.1016/j.ijfatigue.2021.106315
- Akgun et al., "*Fatigue of laser powder-bed fusion additive manufactured Ti-6Al-4V in presence of process-induced porosity defects*", EFM 259, January 2022, 108140, https://doi.org/10.1016/j.engfracmech.2021.108140
- Fatigue 2021: Engineering Integrity Society (EIS) International Conference on Durability and Fatigue
- Fourth International Symposium on Fatigue Design and Material Defects, May 2020
- 2020 National Structural Integrity Research Centre (NSIRC) Annual Conference
- 2019 National Structural Integrity Research Centre (NSIRC) Annual Conference

Table of contents

List of figures

List of tables

Nomenclature

Roman Symbols

a	Crack depth
c	Half width (length) of a semi-elliptical crack
a_{eff}	Effective crack length
a_0	Empirical constant in Eq. 2.5 that enables a smooth transition between small and large cracks
K_f	Fatigue notch factor
K_t	Stress concentration factor
N_f	Number of cycles to failure
$2N_f$	Load reversals to failure
P_i	Individual probability of a fatigue life at a given fatigue strength
R	Stress ratio

Greek Symbols

ΔK	Range of stress intensity factor
ΔK_{th}	Range of threshold value for stress intensity factor
σ_{w0}	Plain sample fatigue strength at 10^7 cycles
σ_w	Fatigue strength at 10^7 cycles in presence of defects
σ_N	Plain sample fatigue strength at N cycles
σ_{Nc}	Fatigue strength at N cycles in presence of a crack

σ_{Np} Fatigue strength at N cycles in presence of porosity

ϑ Poisson's ratio

σ_{local} Local elastic stress component

σ^{∞} Applied far-field stress

δ Critical distance value for averaging peak elastic stress

Other Symbols

$\sqrt{area}$ Square root of the projected area of a volumetric defect

Acronyms / Abbreviations

AM Additive manufacturing

L-PBF Laser powder-bed fusion

WAAM Wire+arc additive manufacturing

μXCT X-ray Computed Tomography at micron scale

Chapter 1

Introduction

1.1 Overview

Metal additive manufacturing (AM), which is referred as "3D printing" in some context, is a near-net shape manufacturing technique that could enhance our conventional processes. For instance, it enables manufacturing of complex designs such as components with internal cooling channels [1], topology optimised brackets [2], composite lattice structures that can be tough and strong simultaneously [3], and 4D materials that change their properties with respect to an external stimuli like time or temperature [4]. Yet, depending on the application, conventional manufacturing routes might be still superior; for example casting is economically more viable compared to AM for the case of a mass production that is commonly seen in automotive industry [5]. Therefore, despite the current hype, it is arguably more valuable to consider AM as part of our manufacturing capabilities rather than as a technology that will replace the current methods.

Titanium alloys, such as Ti-6Al-4V used in this work, are an opportunity for AM as it eliminates high machining costs of titanium and reduce lead times compared to procuring a wrought material. Furthermore, since AM is a near-net shape approach, it can reduce the bulk material cost significantly, e.g. the so-called buy-to-fly ratio of a wrought material is estimated as 20:1, which means 20 times more raw material (billet) is required to produce each kilogram of a final component, and this ratio could be reduced to 3:1 using AM as discussed in [6]. These economic factors combined with the possibility of a higher design freedom should make AM an exciting option for producing components fabricated from titanium alloys in the future.

This thesis is related to recent efforts of transitioning AM from building prototypes to load-bearing components, hence it has a structural integrity focus rather than the process. It is motivated not just by the new products that AM technology may provide, but also from

a fundamental fatigue research perspective since it offers a niche problem to study: the influence of small volumetric defects on high cycle fatigue.

1.2 Motivation, scope and objectives

Currently, AM metals predominantly fail from process-induced defects under cyclic loading in the polished surface condition. This work aims contributing to our understanding of fatigue failure in presence of process-induced defects, which are a subset of material defects, i.e. metallurgical discontinuities in the lower end of the micron scale and usually comparable to grain size. As mentioned in the classic fatigue textbook from Suresh ([7], page 152, Section 4.9), the crack initiation in presence of material defects is alloy dependent, as can be anticipated due to their length scale. Therefore, alloy and process specific research is needed in this topic, especially considering that the microstructure as a result of the AM process differ significantly from conventional manufacturing as discussed later in Chapter 2.4.

Transition radii, bolt holes, and other design features are often the source of fatigue failures, however, they might be neglected in engineering practice if their size is less than $\sim$1 mm, particularly for ductile metals based on the notch sensitivity diagrams. On the other hand, for high-strength materials like bearing steels, even inclusions less than 10 μm in diameter could be detrimental to the reference strength, see for instance [8]. Titanium alloy Ti-6Al-4V and process-induced defects in AM, which are generally below 100 μm for this alloy, belong to the latter case; the literature clearly demonstrates that defects act as the main source of failure under cyclic loading after the as-built surface roughness. It is conceivable that as the AM industry advances, process-induced defects will become a rarity; a similar observation can be made from the steel-making industry where the inclusion content significantly reduced with time [9, 10]. Yet, defects can still emerge either due to randomness or poor workmanship. Thus, developing assessment procedures are essential for a pass/fail decision instead of discarding the component outright, as well as deciding on whether to perform an additional post-processing such as hot isostatic pressing, which is a popular thermo-mechanical treatment in the AM industry. Well-established engineering assessment procedures such as BS 7910 [11] are mainly intended for macroscopic, planar defects in the mm-scale; hence not directly applicable for the case of process-induced defects in AM.

There are two main types of defects in AM, or three if the as-built surface roughness is also considered as a defect. The scope of this thesis is limited to porosity type defects only, considering that pores are inherent to the process, whereas reducing surface roughness is a standard procedure for cyclic loaded components and lack-of-fusion defects could be avoided

by optimising process parameters as discussed in [12, 13, 14]. A further distinction between gas pores and keyholes was not made in the remainder, but pores with irregular morphology were marked, which might indicate keyhole type defects.

Two different AM processes were used in this thesis, namely wire+arc additive manufacturing (WAAM) and laser powder-bed fusion (L-PBF). L-PBF was considered as the main process, and was investigated in Chapter 2 - Literature Review, then expanded in Chapter 3 - Experimental Programme. WAAM scope was limited to using the remaining samples from a previous PhD work [15], hence the experimental details were reviewed briefly in Chapter 3.11, but a separate literature review specific to WAAM process was not conducted; the reader is referred to the referenced thesis for this purpose.

From a mechanics point of view, a constant amplitude axial loading in the high cycle fatigue regime was used due to its simplicity, which allowed focusing on pores without the additional complexity of multiaxial loading. All fatigue tests were conducted in air and at room temperature using a stress ratio (R) of 0.1.

As discussed in the beginning of this section, the ultimate aim of this work is to improve our understanding of fatigue failure in presence of porosity type defects. In this regard, the main objectives can be summarised as follows:

- Develop a controlled experimental programme that circumvents factors other than porosity such as surface roughness, build direction, post heat-treatment, and more that might influence the fatigue performance.
- Study the effect of process-induced porosity on fatigue endurance of L-PBF Ti-6Al-4V and WAAM Ti-6Al-4V by using the developed experimental programme.
- Investigate fatigue crack propagation in L-PBF Ti-6Al-4V by measuring growth rate of fatigue cracks initiated from surface porosity and comparing them to fatigue crack growth rates obtained by standardised measurements of long, through thickness cracks.
- Discuss, analyse and interpret the experimental results from an engineering design perspective to support future design guidelines for fatigue assessment of volumetric defects in AM.

1.3 Assumptions and terminology

The term “defect” is used frequently in the engineering literature, for instance atomic disarrangements like dislocations, manufacturing artefacts like non-metallic inclusions and in-service incidents like foreign object damage. In this work, the defect terminology is used

only for process-induced porosity, which is a subset of material defects. Some design codes distinguish defect and flaw, where the flaw refers to non-critical defects that have negligible influence on fatigue life; this custom was not followed.

In polycrystals such as Ti-6Al-4V, each individual grain has its own stress response to the applied loading. This is often disregarded in engineering practice based on the statistical understanding and a homogeneous material response is assumed. However, the homogeneous response could be invalid when the feature of interest is at the same length scale as grain size. Crack initiating pores in this work, which are given in Table A.3, were around 40 times larger than the grain size, i.e. individual α lath thickness as referenced in Section 2.4; hence a homogenised response in the vicinity of pores was assumed. Furthermore, engineering approaches that rely on nominal stresses were used in this work; thus the notch local plasticity was neglected given that the macroscopic response was strictly in the elastic regime.

Although all AM technologies rely on layer-by-layer building, due to the differences in feedstock material, heat source and more, the resulting microstructure could be reasonably different. Therefore, it was strictly avoided to compare different AM processes and any literature comparison was made within the same AM sub-process. Furthermore, titanium alloy Ti-6Al-4V in the main text was often preceded with an abbreviation, e.g. AM, L-PBF or WAAM that indicates the manufacturing method. The abbreviations might seem inconsistent, yet this was deliberate to highlight whether a statement can be generalised to entire AM process or limited to a specific subset such as L-PBF or WAAM. Finally, given that AM is still a developing technology, statements with regards to AM implicitly means the "current" technological maturity level and can be changed in the future.

1.4 Thesis structure

Literature review in Chapter 2 starts with a concise information about the process, formation of porosity, and AM specific features of Ti-6Al-4V microstructure. The aim of these concise sections is to inform fatigue researchers on AM, and make a self-contained document. Building upon this foundation, Section 2.5 outlines the main parameters in AM that influence the fatigue performance. Afterwards, a more targeted discussion starts by introducing the state-of-the-art in fatigue of defects followed by their application in AM Ti-6Al-4V so far.

Chapter 3 describes the experimental programme and the approach for studying the influence of porosity on fatigue performance of AM Ti-6Al-4V. This Chapter explains the methods used, along with a justification for using that particular approach. Care has been taken to provide enough details so that the work can be reproducible. As mentioned in the scope, the main feature was the L-PBF process.

Chapter 4 aims to present the raw experimental results in a way that contributes to understanding the phenomenology of the problem; i.e. fatigue behaviour in presence of material defects. For this reason the chapter is mostly descriptive, and comparative with respect to conventional manufactured counterparts. It also includes a Section on local elastic stresses in the vicinity of a pore, which includes stress concentration factor based on analytical formulation and a finite element model to supplement the analytical formulations and to visualise the problem.

Chapter 5 provides fatigue design interpretations in presence of porosity. In practice, the fatigue design is often depends on the application, i.e. some components are designed to resist a large number of cycles (durability), whereas some parts are designed to be replaced depending on crack dimensions detected during service intervals (damage tolerant). Similarly in Chapter 5, the fatigue of porosity problem was investigated from the standpoint of a durability and damage tolerant approaches.

Finally, Chapter 6 presents a summary of main contributions and conclusions from this thesis, along with recommendations for future work.

Chapter 2

Background and literature review

2.1 Introduction

This Chapter starts with a brief introduction to metal additive manufacturing (AM) in order to make this work self-contained; more in-depth reading can be found in review papers [13, 16] or books [17, 18] on the subject. Afterwards, supporting topics are introduced such as the porosity formation (Section 2.3), microstructure specific to AM (Section 2.4), including the implications for fatigue of an $\alpha + \beta$ titanium alloy Ti-6Al-4V. Sections 2.2 through 2.4 should help interpreting the fatigue behaviour that is discussed later on. Section 2.5 is based on the exploratory fatigue testing results available in literature and outlines the critical parameters for fatigue behaviour of AM Ti-6Al-4V. Finally from Section 2.6 and onwards the state-of-the-art in fatigue of defects and its applications on AM Ti-6Al-4V are reviewed.

2.2 Metal additive manufacturing

In AM technologies relying on melting, a small layer (thickness) of a feedstock material is melted at a specific location with respect to the computer model of a desired component. The manufactured component consists of many layers that are typically either 30 μm or 60 μm thickness for the case of Ti-6Al-4V. Since the feedstock material is melted, almost fully dense components can be achieved, e.g. bulk density above 99%. Despite many subsets of AM, some shared elements can be defined as shown in Table 2.1.

A typical AM process consists of (1) a computer model of the desired component, which eliminates the need of 2D shop drawings, (2) a feedstock material, (3) a strategy to handle the feedstock, and (4) a heat source for melting. Depending on the specific AM technology, these shared elements are realised differently as listed in Table 2.1. In this work, laser

Table 2.1 Shared elements of additive manufacturing relating to melting processes

Part model	Feedstock	Approach	Heat source
3D CAD	Wire Powder	Deposition Fusion	Electric Laser Electron beam

powder-bed fusion (L-PBF) and wire+arc additive manufacturing (WAAM) technologies were used, which are discussed further in the following.

As the name suggests, L-PBF technology seen in Figure 2.1a deals with metal powders as the feedstock material. The powder is evenly distributed over a substrate that is often a thick plate made from forged counterpart. Then, a laser heat source melts the powder layer selectively depending on the computer model of a desired component. Next, the build platform is lowered and a fresh layer of powder is spread for the next layer. This sequence continues until the part is completely manufactured. In contrast, for the case WAAM technology, Figure 2.1b, the feedstock material is a wire and the wire is not spread but rather deposited selectively over a substrate depending on the computer model of a desired component. Furthermore, the heat source that melts the feedstock is also different and is made of electric energy, i.e. wire or plasma arc. In summary, although the steps of AM process are shared, these steps are performed differently depending on the specific AM technology.

It might be desirable to seek global mechanical properties for AM Ti-6Al-4V, however, the differences in processing discussed so far leads to reasonably different microstructures, e.g. coarse versus fine α lath thickness, that ultimately cause different mechanical properties. Consequently, there is an entire separate body of research work available that compares the mechanical properties of different AM techniques, such as electron beam melting versus L-PBF [19, 20, 21]. As discussed in Section 1.2, the aim of this study was to understand fatigue in presence of process-induced porosity, hence a comparison of different AM processes was considered as out of the scope. For understanding the differences of mechanical properties between the available AM processes, the reader is referred to above referenced works.

2.3 Origin of porosity

Pores are volumetric defects caused by the manufacturing process and their size is typically below 100 μm for the case of titanium alloy Ti-6Al-4V. Two main categories of pores are

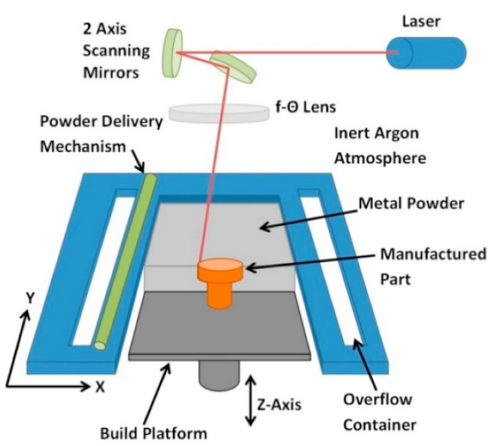

(a) Laser powder-bed fusion

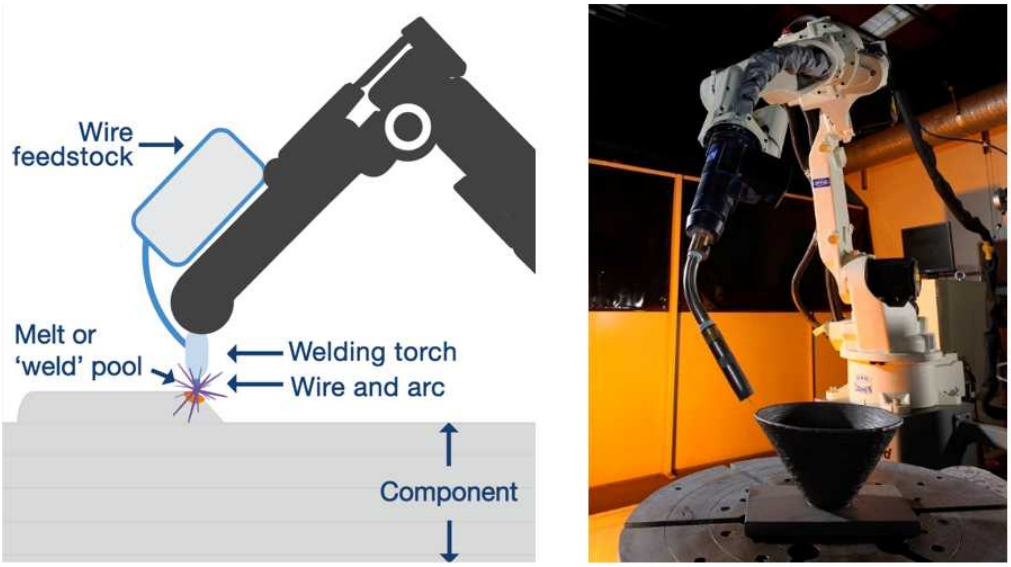

(b) Wire+arc additive manufacturing

Fig. 2.1 Overview of two additive manufacturing processes used in this work. Images are courtesy of TWI Ltd.

present in metal additive manufacturing (AM): gas pores and keyholes, which are shown in Figure 2.2.

Gas pores are roughly spherical, hollow sections that have a smooth interior surface as shown in Figure 2.2(a-b). Their origin is thought to be the shielding gas used across the processing chain. Because of titanium's strong oxygen affinity, it is usual practice to use a shielding gas, which is commonly argon. For instance, argon is used during gas atomisation to produce metal powders, and traces of argon gas bubbles measured between

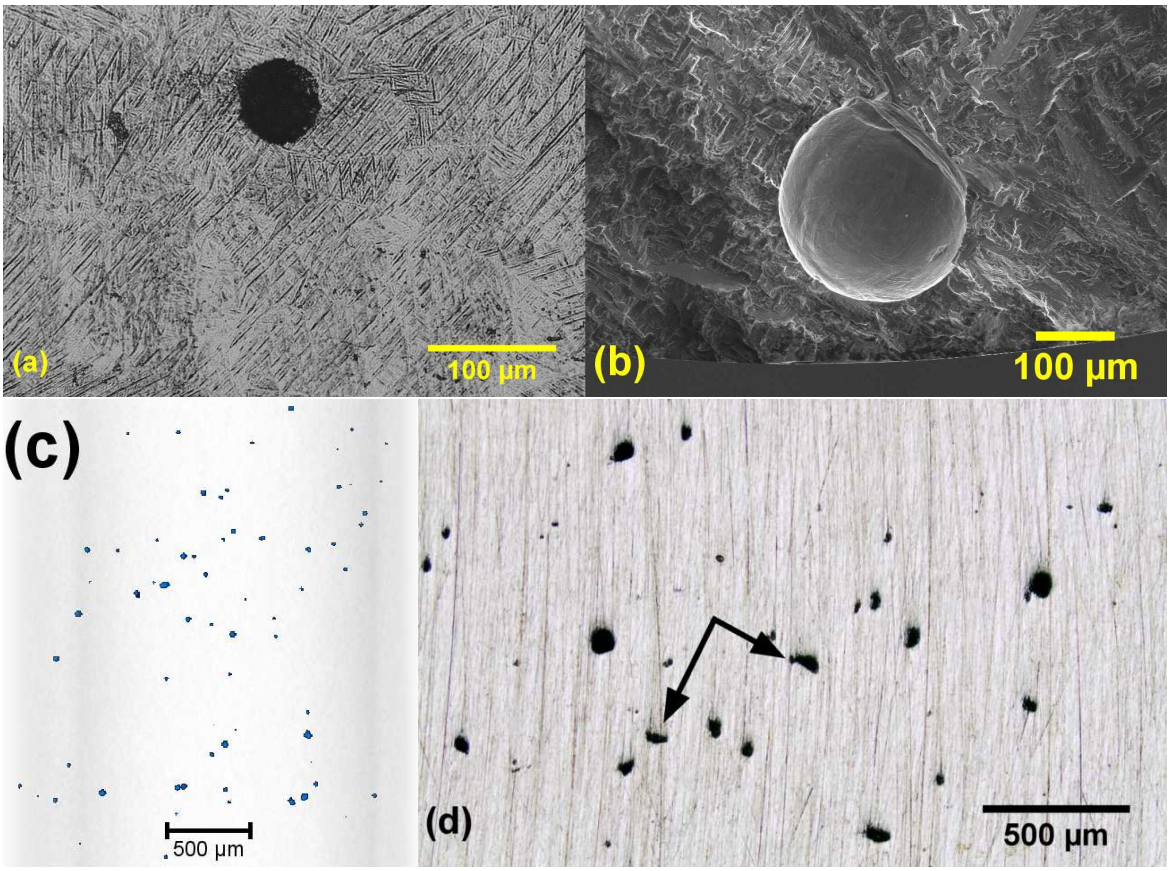

Fig. 2.2 Overview of porosity defects seen in AM Ti-6Al-4V. All images were captured as part of this work. (a) Cross-section of a gas pore using light microscopy of an etched metallographic sample (b) Gas pore as a crack initiation source obtained using scanning electron microscope from a fatigue fracture surface (c) 3D visualisation of porosity obtained using X-ray Computed Tomography (d) Keyhole pores seen on the gauge surface of a fatigue sample (marked by black arrows), obtained using light microscopy

powder particles can be perpetuated to the manufactured components [22]. In some of the AM processing techniques, argon is also used during processing to protect the build chamber against oxygen pickup. Once the feedstock material is melted, the argon gas either from processing chamber or between powder particles could submerge to the melt pool. It is believed that during solidification, some of the submerged gas bubbles are unable to escape the melt pool, hence forming spherical cavities in the manufactured part (Section 2.9.2 in [13]), which are commonly referred as the gas pore defects.

Another mechanism of porosity formation is the so-called keyholes. Keyholes are associated with lasers as the heat source, hence appear only in a subset of AM techniques. Compared to gas pores, their morphology is more complex as seen from Figure 2.2d. The formation mechanism of keyholes involves complex laser physics, however, recent works

revealed many unknowns using in-situ, synchrotron X-ray imaging of single track laser scanning; the reader is referred to these publications for an in-depth reading [23, 24, 25].

2.4 Microstructure specific to additive manufacturing

AM processing leads to distinct microstructural features that are uncommon in conventional manufactured counterparts; hence a separate Section is dedicated to introduce them. Having said that, these microstructural features are often eliminated in practice either via post heat-treatment [26] or even in-situ heat treatment by modifying process parameters [27]. Therefore, the features discussed in the following strictly refer to the as-built condition using standard processing parameters. An introductory knowledge of titanium metallurgy is assumed and will not be repeated. For this purpose, the reader is referred to textbooks such as [28, 29].

Martensitic phase

AM processes considered in this work rely on melting of metals, hence extremely high temperatures are prevalent during manufacturing; for instance the melting temperature of a pure titanium is 1670°C (Table 2.1 in [28]). In contrast, the building platform (substrate) is heated to only a meagre degree, leading to high temperature gradients; for instance during the L-PBF process the substrate is between 200°C-400°C in standard practice [16, 30]. Furthermore, melting of the feedstock material is restricted to a small volume, e.g. semi-circular melt pools with depths less than 200 μm reported in [14]. This combination of high temperature gradient and solidification of a tiny volume leads to rapid cooling. As a result of the rapid cooling, a hexagonal, acicular martensitic phase (α') is reported in [31] using the X-ray diffraction technique, noting that this approach might be inadequate to separate α and α' lattice constants [32]. Furthermore, the martensitic phase can be observed in high-resolution scanning electron microscope images by [26, 30] and in transmission electron microscope images provided by [33]. The presence of martensitic phase suggests that the cooling rate is above 1000°C/min based on the continuous cooling transformation (CCT) diagram [28]. It is also worth noting that non-equilibrium martensitic phase is considered commercially irrelevant [28], which could be attributed to limited ductility; for instance less than 5% elongation was reported as a part of tensile testing in [34, 35].

Columnar grains

Columnar prior-β grains are another characteristic feature of microstructures as a result of AM processing, examples can be seen in [26, 36]. They can be attributed to the shallow melt pools, which cause a re-melting of the previous layer and promote a unidirectional heat flow roughly parallel to build direction [13]. Thus, columnar grains are present in AM and grow in an epitaxial fashion from the previous layer. Although reconstructed columnar prior-β grains show a strong texture, acicular martensitic phase (α') that grows inside these grains show a weak texture and does not exhibit a colony structure due to the rapid cooling [37]. Thus, discussing anisotropy of mechanical properties from a microstructure point of view is challenging and it is often attributed to defects instead [26]. An example of two characteristic features discussed so far is shown in Figure 2.3.

Fig. 2.3 Characteristic features of microstructures for AM Ti-6Al-4V: (a) Columnar prior-β grains seen using light microscopy. (b) Scanning electron microscope image of the acicular martensitic α' phase without any remaining β phase (bright spots) after solidification. Images are original work of [30] and reprinted by permission from Elsevier.

Impact on fatigue

As seen in Figure 2.3, columnar prior-β grains can extend a few millimetres, whereas individual α or α' laths growing inside them are extremely fine. The average α lath thickness values for L-PBF process is between 0.5-1.5 microns [32, 38, 39] based on the intercept method as described by ASTM E112. As described in [28], this type of an extremely fine microstructure is desirable for high-cycle fatigue resistance. Given that high-cycle fatigue is usually dominated by the crack initiation stage, the fatigue performance can be related to crack nucleation resistance. In the microstructural scale, resistance to crack nucleation

depends on plastic deformation, which is associated with dislocation motion, i.e. slip. In the colony type microstructures, i.e. a set of α-grains in the same orientation, slip bands can extend across the whole colony width that could be as large as 600 μm. On the other hand, for individual α-laths as seen in AM microstructures, crack nucleation mostly occur at the longest and thickest α-lath, afterwards propagate through the matrix, where all individual martensitic plates act as a potential obstacle for crack propagation. Therefore, absence of colony structure is usually associated with better high cycle fatigue performance, which is correlated with individual α lath thickness.

Despite the extremely fine microstructure of AM Ti-6Al-4V, its high cycle fatigue performance is generally poor compared to cast or wrought counterparts as shown in review works such as [40]. This poor fatigue performance could be related to either high as-built surface roughness or to presence of manufacturing defects, which are an order of magnitude larger than the thickness of individual α plates. The defects could be suppressed by using heat treatments after manufacturing, however, such heat treatments usually coarsen the microstructure like the popular hot isostatic pressing (HIP).

2.5 High cycle fatigue of laser powder-bed fusion Ti-6Al-4V

2.5.1 Introduction

The aim of Section 2.5 is to review AM parameters that influence fatigue performance and to understand fatigue behaviour that represents current development stage of the processing technology; in this regard experimental data from L-PBF process was used for demonstration. It is hoped that Section 2.5 will set the scene for defect assessment approaches in the following section and provide explanation for some of the decisions taken whilst developing the experimental programme in this work.

2.5.2 Surface roughness

Surface roughness in the as-built condition is a serious concern for laser powder-bed fusion (L-PBF) at the moment as demonstrated in Figure 2.4: it compares the surface roughness in L-PBF Ti-6Al-4V to other near-net shape manufacturing technologies and requirements of fatigue testing standards that often aims representing the true material fatigue strength.

In Figure 2.4, surface roughness is quantified using the R_a parameter, i.e. average of valleys and peaks measured over a certain distance as per ISO 4287 standard [47], thus

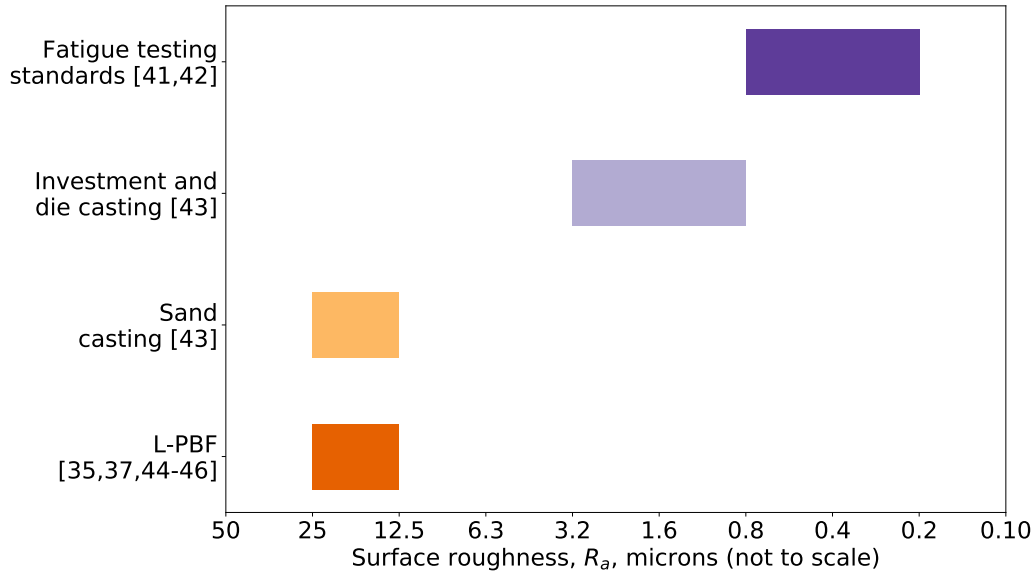

Fig. 2.4 As-built surface roughness in laser powder-bed fusion Ti-6Al-4V compared with other near-net manufacturing technologies (not necessarily correspond to Ti-6Al-4V material) and fatigue testing standards

the actual roughness could be even higher in localised regions. Having said that, even the average value of surface roughness is poor for the L-PBF process and a considerable amount of material removal is necessary to achieve a surface quality that is acceptable for applications subject to high cycle fatigue, for instance R_a value of at least 3.2 microns specified for aerospace applications in [46]. One of the main advantages of AM is near-net shape production and additional material removal to achieve desired surface quality could hinder design complexity potential of AM as special features like internal channels cannot be machined easily to achieve desired surface finish. Furthermore, the surface roughness data in Figure 2.4 corresponds to simple rectangular structures. In case of more complex geometries, for instance with overhangs, surface roughness could be even higher due to the so-called staircase effect [13, 46, 48], which is inherent to layer-by-layer manufacturing.

The next discussion point is the influence of surface roughness on fatigue performance, which is demonstrated in Figure 2.5. In this figure, fatigue data corresponds to different manufacturers, process parameters and more, but limited to the L-PBF process only.

In Figure 2.5, the surface roughness in the as-built condition is compared to a reference state in which the surface roughness was removed and a hot isostatic pressing (HIP) was performed to suppress the influence of internal defects. As seen in Figure 2.5, the surface roughness in the as-built state significantly reduces fatigue strength, for instance an average fatigue strength reduction by a factor of four at a fatigue life of one million cycles can

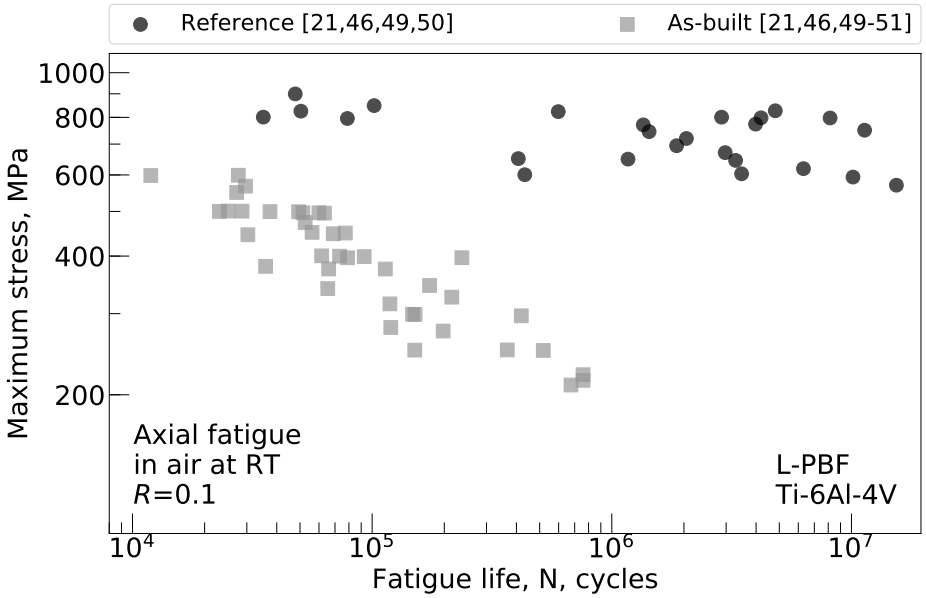

Fig. 2.5 S-N diagram plotted on a double logarithmic scale showing the influence of surface roughness on high-cycle fatigue performance for Ti-6Al-4V manufactured using the laser powder-bed fusion process. In the "reference" state surface roughness is removed and defects are suppressed via a thermo-mechanical treatment (hot isostatic pressing)

be calculated by converting the experimental data presented in Figure 2.5 into logarithmic values, then carrying out a linear regression analysis by treating the logarithm of the cycles as the dependent variable to fit S-N curves. For load-controlled, axial fatigue testing of small dog-bone samples as in Figure 2.5, fatigue is predominantly a surface phenomenon in the high-cycle fatigue regime, i.e. the dislocation motion leads to roughening of the surface (intrusions and extrusions), which then leads to crack initiation. In presence of a high surface roughness as in the L-PBF case, this roughening process is accelerated, which then leads to inferior fatigue life as seen in Figure 2.5.

2.5.3 Process-induced defects

When the as-built surface roughness is removed, fatigue performance improves markedly as seen in Figure 2.6. The fatigue data in this figure is again only limited to L-PBF process, however, include different manufacturers, powders, process parameters and more. The references provided in Figure 2.6 reports that the samples with polished surfaces fail mainly from manufacturing defects, thus the S-N diagram in Figure 2.6 represents the influence of defects on fatigue performance of L-PBF Ti-6Al-4V.

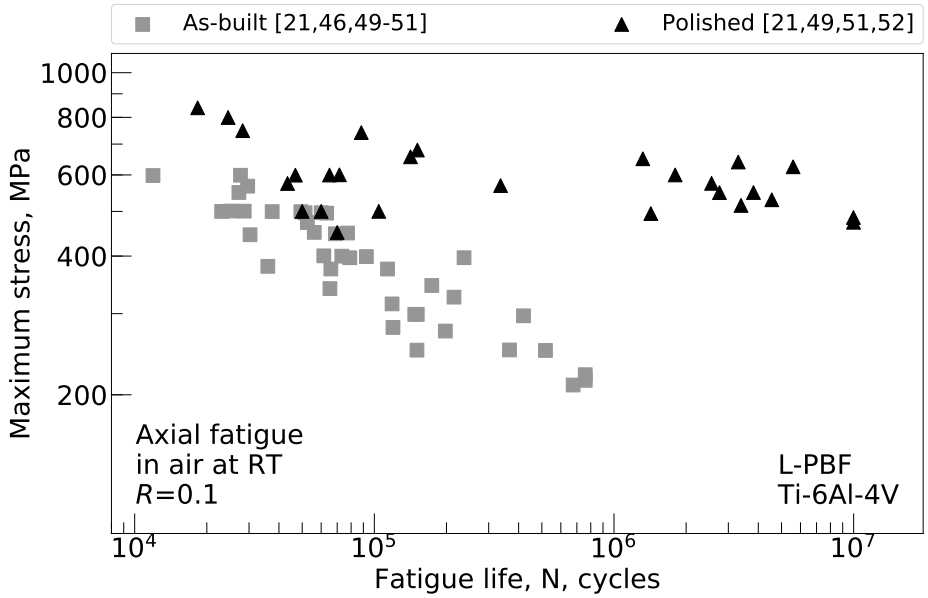

Fig. 2.6 Double logarithmic S-N diagram comparing the as-built condition with high surface roughness to samples with polished surfaces for Ti-6Al-4V manufactured using the laser powder-bed fusion (L-PBF) process

Although fatigue life was improved after removing the surface roughness, the scatter of fatigue life was significantly increased in the polished condition compared to the as-built condition; for instance at 500 MPa and 600 MPa applied maximum stresses, the scatter of fatigue life is around three orders of magnitude as seen in Figure 2.6. This scatter is commonly attributed to the presence of defects [53, 54, 49], however, crack initiation source, location, and size were undisclosed in most of the published work, which is a concern shared with other researchers as well [55]. Thus, it is challenging at this stage to understand more about the influence of defects on fatigue, apart from the scatter observed on the S-N diagram.

The literature also highlights that surface defects are more detrimental than embedded defects, which could be an expected outcome when shape factors in stress intensity factor equations are considered for surface and embedded cracks. By quantifying defect size distribution within a gauge volume of test samples prior to fatigue testing, Tammas-Williams et al. [56] reported that crack initiating pores were usually located at the surface and were consistently smaller than larger embedded pores within the gauge volume. Even more strikingly, Serrano-Munoz et al. [57] reported fatigue cracking from micron-sized small surface defects for a cast material despite the presence of a large 1 mm diameter embedded artificial defect.

Arguably, hot isostatic pressing (HIP) is the most popular solution in AM industry to suppress the influence of defects on fatigue; the improvement of fatigue performance after

HIPing can be seen in Figure 2.5. HIPing is achieved by applying simultaneous heat treatment and external pressure to the material of interest inside a chamber [28]; hence it limits the size of a component that can be manufactured and excludes porous structures. Furthermore, HIPing is performed above the recrystallisation temperature for the case of Ti-6Al-4V and leads to coarsening of the α lath grains [58]. Inspection of fracture surfaces after HIPing confirms that the root cause of failure switches from defects to microstructure [49]. There is a common misconception that HIPing closes the gas pores, see for instance [59]. Although the ideal gas law states that argon, which is the shielding gas commonly used in AM, can be infinitely compressed, the experimental evidence suggests that HIPing merely reduces the size of defects to a certain value that is not detectable by current imaging techniques. In fact, Tammas-Williams et al. [60] demonstrated re-growing pores by applying a heat treatment after HIPing. Thus, it is important to consider that HIPing should be the final post-processing step and the service conditions do not exhibit sufficiently high temperatures for pore regrowth.

2.5.4 Residual stress

In the absence of external loading, the stress distribution present in a structure is referred as the residual stress. When an external cyclic loading with a certain stress ratio (R-ratio) is applied, the residual stresses are superimposed and thus can change the R-ratio. Given that a positive or high R-ratio is associated with inferior fatigue endurance in S-N diagrams and accelerated fatigue crack propagation da/dN vs ΔK plots, tensile residual stresses can be detrimental, whereas compressive residual stresses can be beneficial concerning fatigue design.

In L-PBF process, thermally induced residual tensile stresses can be as high as 50% of the yield strength when measured on the surface [35]; this value is lower compared to arc welding in which the residual stress can be as high as the yield strength [61], but it is still sufficiently high enough to distort and warp manufactured geometry as shown in [35] and to influence fatigue crack growth resistance for the case of L-PBF Ti-6Al-4V. For instance, a clear shift in Paris region can be observed in [34] between stress-relieved and as-built samples, along with an increase in the threshold value of stress intensity factor range (ΔK_{th}) from 1.7 MPa$\sqrt{m}$ to 3.9 MPa$\sqrt{m}$. On the other hand, due to the high surface roughness in additive manufacturing, the influence of residual stresses on high-cycle fatigue strength is hardly distinguishable, when the stress-relieved condition compared to the as-built condition, see for instance the S-N diagrams given in [49].

As discussed in [62], the origin of residual stress in L-PBF is mainly attributed to two mechanisms: (1) constrained thermal expansion near the melt pool by the surrounding solid

material. (2) The thermal contraction of the melted layer due to the high temperature gradients observed during processing: for instance in current commercial applications substrate (build plate) is heated between 200°C to 400°C, whereas the melting temperature of the titanium is above 1600°C. As a solution, heating the substrate around 700°C as in the electron beam melting additive manufacturing process helps reduce the residual stresses by decreasing the temperature gradient [58]. However, this is not possible in many other AM processes.

Figure 2.7 demonstrates a representative residual stress distribution arising from an L-PBF process, which was measured using contour and neutron diffraction techniques as reported in [63, 64, 65]. It can be seen that the edges of manufactured sample are subject to tensile residual stresses, whereas compressive residual stresses are present inside the sample for self-equilibrium. It should be noted the curve steepness between compressive and residual stresses will depend on the build direction and sample geometry. Therefore, a sketch was provided only, since the absolute values of residual stress depends on the sample geometry, build direction and also by process parameters, for instance the travelling direction of the heat source, i.e. the so-called scan strategy as reported in [66]. To illustrate this point, absolute values of tensile residual stresses are provided in Figure 2.8 for different sample geometries.

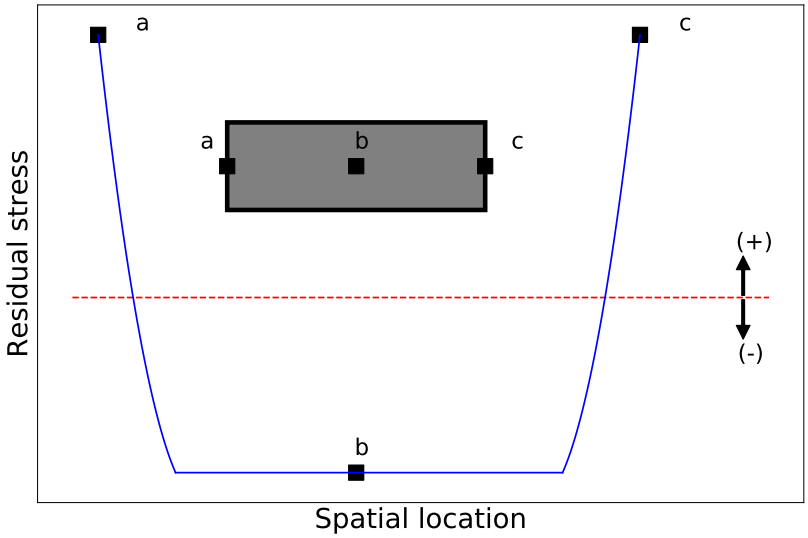

Fig. 2.7 A sketch of residual stress distribution along a specimen cross-section manufactured by laser powder-bed fusion Ti-6Al-4V. The sketch is based on the results from [63, 64, 65] and corresponds to residual stress component that is parallel to manufacturing build direction. Tensile residual stresses can be observed on the surfaces (a,c), which are balanced by the internal compressive residual stresses (b).

Figure 2.8 presents the residual stress measurements for evaluation points just beneath or at the surface using the X-ray Diffraction (XRD) technique, which was selected based on the data availability, noting that surface measurements might not be representative of the actual

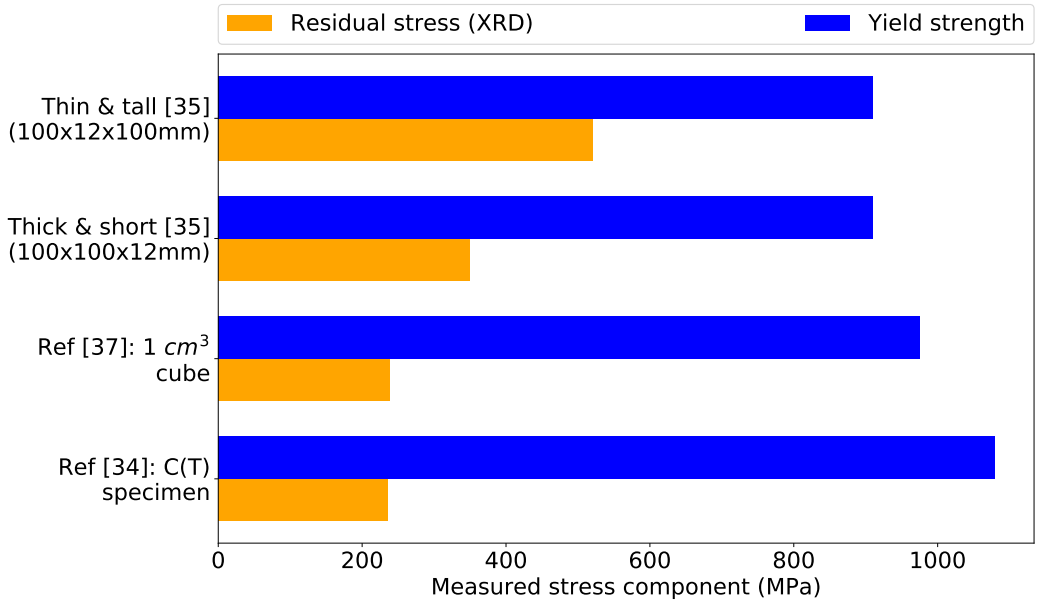

Fig. 2.8 Tensile residual stress as measured on the surface compared to yield strength for laser powder-bed fusion Ti-6Al-4V

stress state as seen in [65]. For comparison, yield strength measurements were also provided in Figure 2.8, however, it should be noted that the surface of residual stress measurements does not necessarily coincide with the cross-sectional plane of yield strength measurements. From Figure 2.8, it can be seen that the tensile residual stress component near the surface was generally higher than 20% of the yield strength, but this value depends on the build direction and manufactured geometry as well, i.e. residual stresses can increase to 50% of the yield strength for high aspect ratio samples.

2.5.5 Build direction

Additive manufacturing offers flexibility of building a design in many orientations; arguably the two main build directions are shown in Figure 2.9. A sample such as shown in Figure 2.9 can be manufactured in the vertical direction, i.e. layer-by-layer rising away from the build platform, or can be manufactured in the horizontal direction lying on the build plate. A more rigorous and comprehensive way for specifying build directions is given in ISO/ASTM 52921 standard.

Majority of the AM literature touch on a potential anisotropy in mechanical properties as a result of the changing build direction, see for instance [35, 67, 68]. The possible anisotropy is most commonly related to crystallographic texture [37], and the presence of high aspect ratio defects such as the lack-of-fusion defect that has a planar, crack like morphology [26].

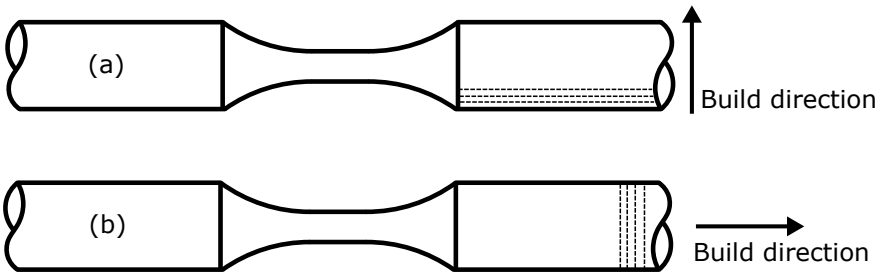

Fig. 2.9 Examples of different build directions in additive manufacturing (a) Horizontal build direction (b) Vertical build direction

Unfortunately, most of the published work report contradicting results, i.e. the existence of anisotropy [35, 68] or negligible influence of the build direction [67, 51].

Recently, works that are more comprehensive have started to appear, for instance Rans et al. [69] studied the influence of columnar prior-β grains on fatigue crack growth rate. In this referenced study, 130 mm tall single edge notched tensile (SENT) specimens were built in the same plane but with five different build directions, and afterwards all specimens were subjected a stress relief heat treatment to eliminate the effect of potentially different residual stress profiles. Resulting prior-β grains were reported to deviate between 5°-15° from the build direction and were in the order of 50 microns wide, resulting more than 10 grains in the thickness direction. Within these constraints, the study was not able to detect any influence of build direction on fatigue crack growth rate; this conclusion was established by comparing the scatter of individual build directions to all orientations, where the scatter band was defined as the 95% confidence interval of the mean experimental data.

In summary, the influence of build direction is still an active research field in metal AM and in this thesis all samples were manufactured in the same direction to circumvent any potential effect on fatigue.

2.6 State-of-the-art in fatigue of material defects

2.6.1 Introduction

The effect of sub-mm size volumetric defects on fatigue is often not covered by textbooks, and until recently, there was only one review paper available from 1994 [9], which presented the existing assessment approaches for fatigue of defects and discussed their predictive capability. In contrast, the aim of Section 2.6 is to present the theory and understanding behind the established fatigue assessment approaches for defects. Furthermore, towards the end of this PhD work, more review papers have become available [53, 70, 71, 72, 73]. As

a result, new researchers studying the fatigue of defects have now access to a variety of different resources.

2.6.2 Notch effect

Under cyclic loading, material defects like porosity often act as preferential sites for crack initiation since they cannot bear any load and increase stresses locally due to their morphology. Thus, defects can be considered as "stress raisers" or notches from a fatigue design perspective and can reduce fatigue performance significantly compared to plain (unnotched) conditions. The increase in local stresses is often quantified by the stress concentration factor (K_t), which is calculated by using Equation (2.1).

$$K_t = \sigma_{max}/\sigma^{\infty} \tag{2.1}$$

where K_t the stress concentration factor, σ_{max} the local maximum elastic stress component due to a notch and σ^{∞} the far-field applied stress. K_t depends on the local geometry of stress raiser and far-field loading conditions; it can be calculated using elasticity theory, e.g. for porosity [74], numerical approaches such as finite element method, e.g. for porosity [75], or can be obtained from reference books such as [76], or can be measured using experimental techniques such as digital image correlation (DIC) [77] as a most recent example.

Predicting fatigue strength in presence of stress raisers by dividing the fatigue strength of a plain (unnotched) sample to the K_t of a stress raiser is an ineffective approach, which can be attributed to the difference in areas under stress: in a plain fatigue test coupon, the entire cross-section is under stress, whereas in a notched sample only a small area is under high stress, which is characterised by K_t. Thus, dividing the experimentally determined fatigue strength value by K_t suggests that the entire cross-section under high stress, which is incorrect. Therefore, the actual knock-down factor, i.e. fatigue notch factor (K_f) often deviates from K_t in reality and expressed using Equation (2.2):

$$K_f = \sigma_{w0}/\sigma_w \tag{2.2}$$

where K_f the fatigue notch factor, σ_w the fatigue strength of a notched sample at a certain number of cycles and σ_{w0} the fatigue strength of a plain (unnotched) sample at the same number of cycles. K_f depends on notch size and its root radius, and also depends on material type as well. K_f needs to be determined either experimentally or by using empirical relationships such those by Peterson [76], Neuber [78] and more. In general, following general characteristics can be said about K_f:

- Notch size effect: Knock-down factor K_f increases as the notch size increases for geometrically similar notches, i.e. equal K_t value, under same applied external loading. In literature, this is often associated with higher stress gradient of larger notches [79].
- Notch root radius: K_f almost converges to K_t value as notch root radius increases, which is demonstrated by classic notch sensitivity diagrams by Peterson [76].
- Material: Another conclusion that can be drawn from notch sensitivity diagrams is the knock-down factor K_f increases along with the increase in material static strength.

In fatigue assessment of defects, stress or strain based notch approaches are not common because of the experimental observations that fatigue cracking occurs early in life, i.e. after a few cycles, hence crack tip stresses dominate the fatigue life rather than the local stresses due to a notch geometry. This finding is important for understanding the research in the field of "fatigue of defects" and is discussed further in the following.

2.6.3 Non-propagating cracks

In the 1950s, Frost and Dugdale [80] showed that for a notch of constant size, as the K_t value increases, i.e. sharper stress-raisers or smaller notch radii, experimentally determined fatigue strength becomes independent of K_t as demonstrated by a constant dashed line in Figure 2.10.

Fig. 2.10 Fatigue strength at 10^7 cycles experimentally determined for a variety of K_t values. Mild steel, axial fatigue tests conducted at R=-1 in air and room temperature. Plain sample fatigue strengths (σ_{w0}) were 200 and 260 MPa respectively. V-notch radius was 0.1mm, 0.254mm, 0.508mm and 1.27mm. Re-created from Frost [81]

As seen in Figure 2.10, after a transition K_t value of around four, the reduction in fatigue strength saturates and the fatigue strength becomes independent of the stress raiser geometry

that is captured by the K_t parameter. The lost correlation between the stress raiser geometry and the fatigue strength was attributed to fatigue cracks initiating almost immediately from "sharp" stress raisers as observed during the experiments; hence, the problem was dominated by crack-tip stresses instead of the local elastic stresses due to the geometry of a stress raiser.

Besides the observation of early fatigue crack initiation, Frost and Dugdale [80] detected fatigue cracks even in run-out samples. It was stated that, if the applied load was below the propagation threshold, i.e. dashed lines in Figure 2.10, fatigue cracks were still initiated after a few load cycles but then these cracks stopped propagating when a certain number of cycles was reached; hence the name non-propagating cracks. Therefore, the problem of estimating fatigue strength in presence of a stress-raiser turns into finding a threshold stress value for fatigue crack propagation, i.e. determining a crack is whether non-propagating type or a critical crack that leads to failure.

Similar observations were made later for small defects such as drilled holes in carbon steels by [82] and inclusions in aluminium alloys as per AGARD experimental programme [83], i.e. the researchers observed cracks initiated very early in fatigue life from these defects. Therefore, in the literature and the remainder of this chapter, the terminology of "defect" and "crack" is sometimes used interchangeably.

It should be noted, however, relating the crack initiation phenomenon to a single K_t parameter could be overly simplistic, especially for the case of small defects in contrast to macroscopic notches as in Figure 2.10. In reality, fatigue crack initiation depends on a number of factors such as the morphology and slip characteristics of material microstructure, ductility or brittleness of the material, residual stress fields near defects and more. Thus, K_t could only be an empirical value when determining the transition regime; for instance K_t value of non-metallic inclusions is much smaller compared to the transition K_t value determined for macroscopic V-notches in Figure 2.10, yet the experimenters observed early crack initiation in both instances.

2.6.4 Anomalous behaviour of small cracks and the threshold problem

As discussed so far, given that fatigue cracks in presence of defects are observed to initiate early in fatigue life but could stop growing after a while, the fatigue assessment of defects could be reduced to predicting a threshold value below which cracks stay dormant. For macroscopic "long" cracks, this is a material constant and is defined by the threshold value of stress intensity range, ΔK_{th}, which can be determined by mechanical testing procedures given in industrial standards such as in ASTM E647 [84]. On the other hand, the non-propagating cracks discussed in Section 2.6.3 were relatively small, e.g. reported to be 200 microns or

less [82]. Such small cracks could grow below ΔK_{th} as reported by review papers on the topic of "small" cracks, e.g. [85], and sketched in Figure 2.11.

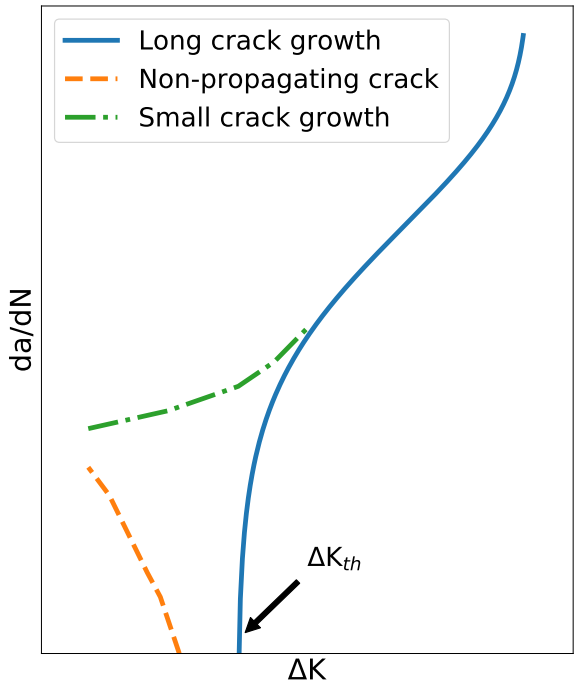

Fig. 2.11 A sketch demonstrating the anomalous behaviour of small cracks

Figure 2.11 shows a threshold value of ΔK_{th} can be experimentally determined for long cracks, which is defined as the asymptotic value of ΔK at which crack propagation rate (da/dN) approaches nearly zero. In contrast, small cracks can grow below the ΔK_{th} value and this anomalous behaviour of small cracks is often attributed to the breakdown of similitude condition at the crack tip: ΔK_{th} parameter is determined using large, through thickness cracks in the mm-scale and the shielding mechanisms, e.g. plasticity induced crack closure, present at this mm-scale can be absent in small, sub-mm scale cracks. As shown in Figure 2.11, some of the small cracks can still arrest after reaching to a certain size, i.e. non-propagating cracks, therefore different engineering assessment approaches were developed to determine the threshold value for propagation of small cracks.

Continuing from the Frost and Dugdale study [80], a further observation that can be made from Figure 2.10 is that the threshold stress for fatigue crack propagation is size dependent, e.g. 45 MPa for a V-notch with 5.08 mm depth and 90 MPa for a V-notch with 1.27 mm depth. For prediction of the threshold stress, Frost [81] suggested an empirical formula by fitting a line to the experimental data in a stress versus effective crack length plot:

$$\sigma_w^3 a_{eff} = \text{constant} \tag{2.3}$$

where σ_w the fatigue strength at 10^7 cycles in presence of stress-raisers, a_{eff} the length of a stress-raiser plus non-propagating crack, and the constant equal to 5.2x10^5 for stress in MPa (or 140 for stress in ton/in^2 as provided in the original paper). Later fatigue research justified this empirical approach by using a stress intensity factor and a more rigorous fracture mechanics framework, i.e. the threshold value of stress intensity factor range (ΔK_{th}) is a material constant.

An important observation was made by Kitagawa and Takahashi [86] during their study of small crack growth initiated from a sub-mm size, artificially introduced defect on the surface fatigue dog-bone samples. After determining ΔK_{th} value at a cut-off value of 2x10^{-9}m/cycle for various crack dimensions, they have demonstrated that fatigue strength, σ_w, follows the linear elastic fracture mechanics (LEFM) formulation using long crack ΔK_{th} value as an input, however, for small cracks below a transition size of a_0, fatigue strength, σ_w, deviates from LEFM formulation and approaches to the plain specimen fatigue strength, σ_{w0}, as shown in Figure 2.12.

Fig. 2.12 Kitagawa-Takahashi diagram [86] along with El-Haddad et al. modification [87]

In contrast to empirical approach in Equation 2.3, here in Figure 2.12 a phenomenological approach was taken by defining a material constant that can be determined via typical fatigue experiments such as load-shedding to determine ΔK_{th} and endurance testing to determine $\Delta\sigma_{w0}$. The correct shape for the prediction curve is an on-going research area, see for instance [88, 87, 89, 90, 91]. In the context of metal AM, El-Haddad, Smith, Topper approach [87] is the most popular so far, which is shown in Figure 2.12 and can be generated using Equations 2.4-2.5.

$$a_0 = \frac{1}{\pi}\left(\frac{\Delta K_{th}}{\Delta \sigma_{w0}}\right)^2 \tag{2.4}$$

$$\Delta \sigma_w = \frac{\Delta K_{th}}{\sqrt{\pi\,(a+a_0)}} \tag{2.5}$$

where $\Delta\sigma_w$ the fatigue strength range at 10^7 cycles in presence of stress-raisers, $\Delta\sigma_{w0}$ the range of fatigue strength of a plain sample, ΔK_{th} the threshold value for stress intensity factor range, a the length of a stress-raiser, and a_0 the material constant.

2.6.5 Stress intensity factor for cracks with arbitrary shapes and $\sqrt{area}$ parameter

It is subjective to select an effective crack length either for 2D cracks that are common in fatigue such as elliptical cracks or in presence of stress raisers with different geometries, for instance selecting the diameter of a blind hole over its depth. By using elliptical cracks, Murakami and Endo [92] showed that maximum stress intensity factor is proportional to the fourth root of a cracked area up to an aspect ratio of five. Then, for arbitrarily shaped cracks, Murakami and Nemat-Nasser [93] divided their area into triangles, i.e. similar to a finite-element mesh, and calculated maximum stress intensity factor using the body force method. These numerical values were then plotted against fourth root of cracked area and the relationship in Equation 2.6 was obtained:

$$K_{\max} = 0.629\sigma\sqrt{\pi\sqrt{\text{area}}} \approx 0.65\sigma\sqrt{\pi\sqrt{\text{area}}} \tag{2.6}$$

where K_{max} is the maximum stress intensity factor of an arbitrarily shaped crack under mode-I loading, σ the far-field applied stress, and the $\sqrt{area}$ corresponds to square root of the cracked area. Equation 2.6 was determined by fitting a linear regression curve to the numerical solution data for a square crack, a rectangular crack, a partial circular crack, and a combined crack consists of a rectangle and triangle. Equation 2.6 enables to compare different shapes of stress raisers and assess their influence on fatigue strength using a single parameter, $\sqrt{area}$; hence extremely useful.

Then, a practical problem related to non-propagating cracks initiated from stress raisers is that they do not exhibit a constant length and seem to follow an inherent uncertainty. Frost [81] reported the length of non-propagating cracks were different even though fatigue crack propagation threshold was constant. Similarly, Murakami [82] reported varying non-propagating crack lengths between 10 μm to 100 μm for the same fatigue crack propagation

threshold. Given that the stress intensity factor requires crack size as an input, then a material can have multiple ΔK_{th} values due to the variable nature of non-propagating cracks. A pragmatic solution to overcome this problem was suggested by Smith and Miller [88] for V-notches and later by Murakami and Endo [94] for defects: considering that non-propagating cracks are very small compared to the size of a typical stress raiser, they can be neglected and ΔK_{th} value can be correlated with the actual stress raiser size. This assumption is visualised in Figure 2.13 and it is customary to use pore size only in this instance by neglecting the planar, non-propagating cracks.

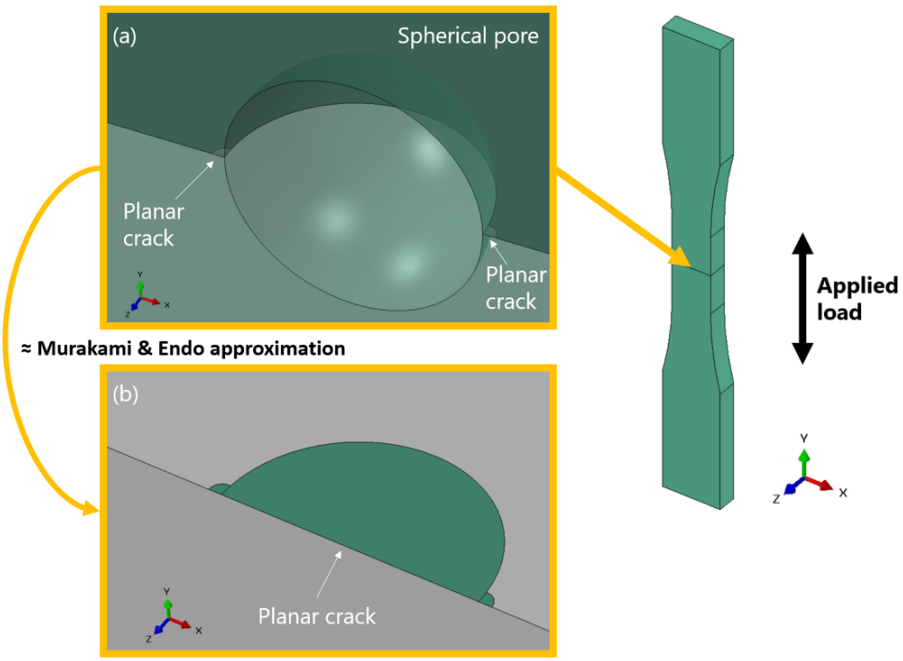

Fig. 2.13 Schematic of converting volumetric defects into planar cracks by projecting the defect area to the plane perpendicular to the applied load direction.

2.7 Fatigue strength prediction of powder-bed fusion Ti-6Al-4V in presence of defects

The state-of-the-art in fatigue of material defects introduced thus far was mainly developed using conventionally manufactured mild steels. In the following, applications of these methods are reviewed for an additive manufactured Ti-6Al-4V. While evaluating the presented results in this Section, the reader should be aware of below listed caveats and limitations.

- Due to lack of available data, both powder-bed manufacturing techniques, i.e. electron beam melting (EBM) and L-PBF, were considered. As mentioned previously, due to differences in process, the resulting microstructures are reasonably different, which can influence fatigue strength in addition to defects.

- A common feature in all the referenced work in this Section is that they accept cracks initiate early in fatigue life without making any observations. In other words, defects were assumed as effective cracks without any evidence.

- Although results were presented in a traditional Kitagawa-Takahashi (K-T) diagram that plots fatigue strength versus defect size, due to inclusion of different studies, fatigue strength is also inevitably influenced by the difference in feedstock (powder quality), AM machine manufacturer and model, process parameters, test specimen size, surface quality, and more.

- Except non-metallic inclusion studies, most of the previous work presented in the state-of-the-art was based on artificial defects, e.g. V-notch or drilled hole with a certain depth and radius. Artificial defects with controlled dimensions make it possible to determine fatigue strength in a statistically significant way, e.g. staircase approach, and the K-T diagram is drawn using these data points. In contrast, AM studies typically work with process-induced defects, which have uncontrolled dimensions, hence presented K-T diagrams in the literature were populated with data obtained from S-N type testing, i.e. not strictly suitable for fatigue strength determination. In fact, most of the data points presented in the following were failed way below common fatigue endurance of 10^7 cycles.

One of early works in fatigue strength prediction of L-PBF Ti-6Al-4V in presence of defects was a conference paper by Wycisk and coworkers [51]. In this study, first a fatigue strength of $\Delta\sigma_{w0}$=450 MPa at 10^7 cycles was estimated from an S-N diagram. Afterwards, a threshold value of the stress range intensity factor $\Delta K_{th} = 3.48 MPa\sqrt{m}$ was determined by extrapolation of the fatigue crack growth experimental data. Then, these experimental values were taken as input to generate a K-T diagram by using Equations 2.4-2.5. The generated K-T diagram was evaluated by nine data points obtained from the S-N diagram; four of the data points were tested at $\Delta\sigma$=450 MPa from which two were run-outs and the remaining five data points were tested below $\Delta\sigma$=450 MPa from which three of them were run-outs. In this early work, the results were presented using an equivalent crack length parameter that considers different shape factors for the variety of defects, e.g. lack-of-fusion, porosity, that were observed on the fracture face. This terminology was not followed in this review, and the

experimental data obtained from this work was converted to more familiar $\sqrt{area}$ parameter in the following.

Afterwards, Beretta and Romano [55] published a review paper on sensitivity of fatigue strength to defects in AM metals. Unfortunately, the majority of the data points in this work were from casting, except for the Wycisk et al. [51] study as described above. Still, this work is an important milestone in fatigue of defects in AM since it presented to use $\sqrt{area}$ parameter in the horizontal axis of the K-T diagram. Furthermore in this work, a slightly higher fatigue strength of $\Delta\sigma_{w0}$=495 MPa at $5x10^6$ cycles was estimated.

In general, there is lack of relevant data in L-PBF Ti-6Al-4V, i.e. most of the time crack initiating defect dimensions are not disclosed in literature. Also, most of the time, applied stress values are much higher than the estimated $\Delta\sigma_{w0}$ values, hence the generated data points naturally fall outside of the K-T diagram, making it hard to evaluate the prediction curve. Therefore, the described studies so far were enriched by two further studies from literature [95, 96], however, nothing that the experimental data in them were generated by a different AM process, namely electron beam melting.

Fig. 2.14 Double logarithmic plot of change in fatigue strength with respect to crack initiating defect size for powder-bed fusion Ti-6Al-4V at R=0.1. Experimental data from [51, 95, 96]

Figure 2.14 shows two prediction curves for fatigue strength in the presence of defects. This solid line curve was suggested by Beretta and Romano [55] using the El-Haddad, Smith, Topper approach (Equations 2.4-2.5) with a reference defect size $\sqrt{area}_0$=200μm; it should

be noted that a_0 parameter in Equation 2.4 is replaced by square root of the defect area. On the other hand, $\sqrt{area}_0$=40μm can be estimated by dashed line curve from Wycisk et al. [51]. By looking at the available experimental data, i.e. scatter points, the Beretta and Romano curve seems promising in terms of prediction quality. Having said that, there is a lack of experimental data beyond $\sqrt{area}$=100 μm crack initiating defect size, thus it would be challenging to state fatigue strength reduces monotonically above 100 microns defect size as the prediction curve suggests. Furthermore, the constant ΔK_{th} curve corresponds to 8.0 MPa$\sqrt{m}$; this is much higher than the actual values as shown in Figure 2.16 and thus signifies the empiricism of the El-Haddad, Smith, Topper approach. Finally, the experimental data shown in Figure 2.10 of state-of-the-art were estimations of fatigue strength at 10 million cycles, whereas the experimental data in Figure 2.14 corresponds to S-N type testing with fatigue lives range from 50,000 cycles to 5 million cycles. Therefore, the prediction curves shown in Figure 2.14 should be validated using more realistic fatigue strength estimates at 10^7 cycles, for example by using staircase type testing with known crack initiating defect dimensions.

Next, a similar exercise was carried out for a stress ratio of R=-1 using the experimental data from literature, which can be seen in Figure 2.15. This time, another popular prediction approach from Murakami-Endo [94] was also considered, which is shown in Equation (2.7).

$$\Delta\sigma_w = \frac{1.43(Hv+120)}{\sqrt{area}^{1/6}} \tag{2.7}$$

where σ_w the fatigue strength in presence of a defect and Hv the Vickers hardness of the material. It is worth noting that this equation follows a similar linear trend as originally proposed by Frost in Equation (2.3), albeit at a different slope. In the referenced publication, it is stated the prediction accuracy of Equation (2.7) is $\pm$10% and valid for defects below $\sqrt{area}$=1000 μm, Hv in the range of 70 to 720.

The argument for empiricism can be further justified by looking at Figure 2.15. The El-Haddad approach suggested by Beretta and Romano [55], which seemed to be working for R=0.1 data in Figure 2.14, is now over-conservative for majority of the experimental data and unconservative for some. On the other hand, Murakami-Endo approach [94] seem to be better suited for the mean values, except it requires a safety factor to cover extreme values around 500 MPa to 700 MPa stress range.

Literature data collected for R=-1 load ratio reveals another problem that is not discussed so far: fatigue under far-field stress is a variable with a certain statistical distribution. For instance, fatigue strength varies more than 50% for defect size approximately 50 μm as seen in Figure 2.15. The variability of fatigue strength data can be attributed to two categories:

Fig. 2.15 Double logarithmic plot of change in fatigue strength with respect to crack initiating defect size for powder-bed fusion Ti-6Al-4V at R=-1. Experimental data from [97, 98, 1]

(1) due to difference in AM machine models, process parameters and more, (2) due to inaccuracy of methods determining fatigue strength. For instance, experimental data in [97] was collected using step-testing method, which is comprehensively validated for Ti-6Al-4V [99], whereas other data points correspond to run-outs in S-N type testing. Therefore, the variability of fatigue strength data makes it difficult to assess validity of various approaches for fatigue strength prediction in presence of defects.

2.8 Fatigue crack growth resistance of laser powder-bed fusion Ti-6Al-4V

2.8.1 Introduction

Fatigue in presence of defects is discussed so far from a “threshold problem” point of view, e.g. for a known defect size the problem of predicting fatigue strength at a certain number of cycles, or alternatively making a binary pass/fail decision for a given design stress. Examples of this approach are shown in Figures 2.14-2.15, in which the prediction curves are either determined using empirical equations, e.g. Eq 2.3, or by combining endurance limit of a

plain specimen and threshold value of stress intensity factor, e.g. Eq 2.5. Given that fatigue cracks either observed or accepted to initiate early from defects, an alternative approach to the threshold problem would be considering the fatigue life as a crack propagation problem for a given constant cyclic load or variable load spectrum. Therefore, this Section starts with introducing long crack growth rates measured from standardised tests such as ASTM E647 [84]. Then application of these growth rates for fatigue of defects is discussed.

2.8.2 Long crack growth rates

Figure 2.16 shows fatigue crack growth rate of the additive manufactured titanium alloy Ti-6Al-4V and compares with conventional manufactured counterparts. Consistent with the previous sections, literature data was limited to L-PBF process, however, different manufacturers, powders, process parameters etc. were included.

Fig. 2.16 Fatigue crack growth rates of laser powder-bed fusion Ti-6Al-4V is compared to conventional manufactured counterparts. Experimental data from [28, 34, 44, 100, 101, 102]

The data in Figure 2.16 was generated using compact tension specimens and through thickness cracks. Such "long" cracks are mainly insensitive to local variations in microstructure, and follow the growth characteristic of a bulk material that is often quantified using the empirical Paris law constants, e.g. C and m. Therefore, it is reasonable that the observed scatter is low in Figure 2.16; for instance in Paris regime between 10^{-9} to 10^{-6} m/cycles most of the test data was within two standard deviations, a value comparable to offshore steels reported by [103]. In contrast, a significant scatter is seen on Figure 2.6 for high cycle fatigue of plain and polished samples, where fatigue life is dominated by the small crack growth regime that is sensitive to local variations in microstructure, i.e. such as unfavourably oriented surface grains. Having said that, the relatively low scatter observed in Figure 2.16 can be increased as seen in the reference [104], if additional data is included from different AM processes like electron beam melting, which replaces the laser heat source with an electron beam. The increase in scatter could be attributed to considerably coarser microstructure in electron beam melting compared to L-PBF. Consequently, it seems that mixing different AM processes should be avoided when collecting data from literature.

As discussed in Section 2.4, fine microstructures are desirable for high-cycle fatigue performance. In contrast, resistance to fatigue crack propagation follows an opposite trend, i.e. coarser microstructures provide higher damage tolerance compared to finer microstructures [28]. This statement is based on the understanding that sub-micron grains cannot be an obstacle for long cracks in millimetre scale, whereas in a coarse microstructure it is possible that two large α-colonies with different orientations branching in front of a crack path could provide resistance to fatigue crack growth (Fig 5.24, [28]). L-PBF Ti-6Al-4V has a fine microstructure, thus it exhibits faster fatigue crack growth rates compared to conventional manufactured counterparts as seen in Figure 2.16 and expected from the arguments presented so far. In contrast, a cast Ti-6Al-4V with colony α grains of 600 μm width exhibits much slower growth rates in the Paris region between 10^{-9} to 10^{-6} m/cycles, and this difference slightly diminishes compared to a wrought material with colony α grains around 20 μm in width. Having said that, some works in the literature [34] account this difference within the usual scatter seen in fatigue crack growth rates and claim the damage tolerance of L-PBF Ti-6Al-4V is comparable to their conventional counterparts.

2.8.3 Crack propagation approach for fatigue of material defects

Assuming that majority of the fatigue life will be spend in the crack propagation regime, Figure 2.17 sketches various crack propagation scenarios depending on the crack initiation source and ignoring the possibility of non-propagating cracks, i.e. the applied stress level is high enough to propagate cracks until failure. Fatigue cracks initiated from defects spend

majority of their life as small cracks, i.e. in the sub-mm zone, as seen in Figure 2.17. This suggests that growth rates of fatigue cracks measured during standardised tests such ASTM E647 [84] might be inapplicable due to the anomalous behaviour associated with small cracks. This loss of similitude between long cracks and small cracks is discussed further in the following.

Fig. 2.17 Crack growth stages depending on the crack initiation source. Reproduced from page 22, Figure 2.7 in [105]

Small cracks can grow faster than long cracks at the same nominal ΔK value and can grow below the ΔK_{th} value as well [85]. Furthermore, even using ΔK parameter could be suspect, since the small scale yielding condition cannot be always fulfilled, i.e. crack-tip plastic zone size could be large compared to the crack and associated local elastic field. Then, even if the small scale yielding condition is fulfilled, the crack-tip conditions might still differ: long cracks are known to subject crack-tip shielding mechanisms such as plasticity induced crack closure in aluminium alloys [106] or roughness induced crack closure in titanium alloys [107]. Given that such shielding mechanisms are absent for small cracks, this could also lead to difference in crack growth rates. In summary, using measured growth rates of long fatigue cracks might lead to unconservative growth rates for small cracks.

Small cracks can be further divided into three categories [85]: (1) microscopically small cracks that are in the range of grain dimensions. (2) Mechanically small cracks where heterogeneous response of individual grains can be averaged, but the small-scale yielding condition cannot be fulfilled, i.e. crack-tip plastic zone size is in the same range of crack size. (3) Physically small cracks, where the small scale yielding condition can be fulfilled, but the crack growth does not exhibit any shielding effect. For the first category, physics based crystal plasticity models are available [108], whereas the other categories are limited to phenomenological models such as the cyclic resistance curve [90]. In practice, specifically for the case of AM Ti-6Al-4V, the concept of equivalent initial flaw size (EIFS) is often used which will be discussed in the following.

AM Ti-6Al-4V

EIFS approach has been extensively used to predict fatigue life of AM Ti-6Al-4V and other alloys [109, 110, 111, 112, 113]. This approach assumes crack propagation from the first cycle, usually using a semi-elliptical crack geometry. Then, an initial crack size is back-extrapolated using a crack growth law, crack shape assumption, and fatigue life obtained from testing. A summary of some of the literature work is given in Table 2.2.

EIFS ranges specified in Table 2.2 were used to predict fatigue life as seen in experiments by plugging them in to the corresponding crack growth laws and crack driving forces. Table 2.2 highlights the flexibility of the EIFS approach: it can be used to predict different crack initiating sources and load spectrums. However, selected crack growth law and crack shape leads to significantly different EIFS values, e.g. a three orders of magnitude difference is observed in Table 2.2. Therefore, this approach should arguably be used in ad-hoc basis rather than selecting an EIFS value from the literature.

Generally speaking, a correlation between the EIFS value and the crack initiating defect size is non-existent; this can be seen in the first line of Table 2.2. However, if the small crack growth rates are used during back-extrapolation, the EIFS value and the crack initiating defect size can comparable as seen in Figure 2 of [110]. This might not always be the case though, if the crack initiation from a defect is delayed or small crack propagation rate show a significant variability compared to the rates used during back-extrapolation. In line two of Table 2.2, small crack growth rates were used and EIFS values are comparable to crack initiating pore dimensions. However, this might be a coincidence as well, since Equation 2.4 used to calculate crack driving forces is validated only for estimating maximum K-value at a given instance, not for growing a crack. Also small crack growth rates used in [111] corresponds to a direct energy AM process, whereas fatigue life prediction was performed for electron beam powder-bed AM process.

Table 2.2 Summary of equivalent initial flaw size values calculated for additive manufactured Ti-6Al-4V

	Growth law (m/cycle)	Driving force	N_f, Life (cycles)	Initiation source	EIFS range (μm)
Constant amplitude axial fatigue $\Delta\sigma$=540 MPa at R=0.1					
[109]	$2.1\times10^{-10}\Delta K^{2.451}$	Surface crack in in a cylinder [114]	15,491 to 2,480,645	Defects (20-160μm)	4-40
[111]	$1.8\times10^{-13}\Delta K^{4.7}$	Arbitrary shaped crack Eq. 2.6	17,734 to 101,868	Defects (92-192μm)	50-200
[115]	$1.4\times10^{-12}(\Delta K_{\text{eff}})^4\times\left(1-\frac{(\Delta K_{\text{eff}})_{\text{th}}}{\Delta K_{\text{eff}}}\right)^2$	Semi-elliptical crack using FEA	80,000 to 100,000	Surface roughness	70-170
Variable amplitude, representative flight load spectra					
[110]	$2.79\times10^{-10}(\Delta K_{\text{eff}})^{2.12}$ $\Delta K_{\text{eff}}=\frac{(\Delta\text{K}-\Delta\text{K}_{\text{thr}})}{(1-\text{K}_{\max}/\text{A})}^{0.5}$	not given	2700h design life	Surface crack	1270

Finally, it is also worth noting that the initial ΔK values calculated in EIFS approach are usually lower than the ΔK_{th} value. Given that small cracks can grow below the ΔK_{th} value, the crack growth laws in Table 2.2 were either extrapolated in the case of linear laws, or were extended by setting ΔK_{thr} value to zero in the case of crack growth laws that model all three regions in the da/dN vs ΔK diagram. These approaches might not necessarily correlate with the actual growth rates of small cracks, hence the back-extrapolated EIFS value will have no physical relevance.

2.9 Summary and knowledge gaps

Most of the prior literature have focused on the influence of AM process on fatigue performance by changing many parameters, hence these works can be categorised as exploratory. The explored areas include but not limited to difference in laser scanning pattern, layer thickness, build direction, powder quality, heat treatment and more. These work uncovered the main aspects in AM that influence the fatigue; for instance the as-built surface roughness is the most detrimental condition and the wrought material fatigue performance can be achieved by a combination of surface roughness removal and hot isostatic pressing. Furthermore, based on the analysis of exploratory literature that represents the current AM technological

maturity, it is evident that process-induced defects such as porosity are a primary source of failure under cyclic loading and fatigue life in the polished surface condition exhibits a significant scatter on the S-N diagram. Yet, it is difficult draw more conclusive results from the literature apart from these general remarks. This is because even if all samples in a particular study were failed from defects, it is challenging to uncouple effect of defects when other parameters such as the build direction were also different. Therefore, a targeted experimental programme is needed to understand the influence of defects on fatigue. In addition, fatigue test results in literature often neglect reporting the morphology, size and location of crack initiating defects, thus there is a lack of relevant data at the moment, which is also mentioned by other researchers [55]. Finally, following questions can be asked related to fatigue of defects in AM:

- How does porosity affect the scatter of fatigue life seen in AM metals? In the literature, the defect size has been suggested as the main driver, i.e. larger pores cause shorter fatigue lives and smaller pores lead to longer fatigue lives, thus ultimately causing a scatter of fatigue life on the S-N diagram. Does experimental data supports this statement?

- State-of-the-art suggests assuming volumetric defects as planar cracks for engineering assessment. Yet, depending on the specific alloy and considering the relatively blunt morphology of spherical gas pores, the crack initiation life might be significant, i.e. crack initiation might take considerable amount of cycles compared to total fatigue life. In this case, should pores be assumed as planar cracks or stress-raisers, i.e. notches for engineering assessment?

- In case of an early crack initiation from porosity as suggested by current state-of-the-art, do cracks spend majority of their lifetime in the small crack regime or a similitude to long crack growth rates obtained from standardised tests can be established?

Chapter 3

Experimental programme

3.1 Introduction

Building upon the exploratory research showing process-induced defects as one of the primary source of failure under cyclic loading, an experimental programme was designed to explore the fatigue behaviour in presence of defects. One of the main considerations in experimental design was to circumvent features other than defects that might influence the fatigue performance without losing relevance to industry practice. The remainder of this section expands the experimental programme and provide concise information for reproducibility. A summary of the programme is given in Table 3.1 for convenience.

Mechanical properties of metal additive manufacturing (AM) materials are improving rapidly, for instance the elongation at break improved from 5% to 15% for stress relieved laser powder-bed fusion processed Ti-6Al-4V samples in couple of years [34, 49]. Therefore, experimental programme designed in a way that it is not particularly focused on individual values of mechanical properties, which seems to be improving continuously, but rather to explore general trends of fatigue behaviour in presence of defects. For example, instead of S-N type testing, repeating the fatigue tests at an arbitrarily selected stress level was preferred to explore fatigue life scatter. Furthermore, even though defects are clearly demonstrated as a primary source failure under cyclic loading, only a handful of data is available in literature concerning crack initiating pore diameters. The handful of available data is also challenging to compare, because many process parameters were different, which is a curse of flexibility for AM. Therefore, a dedicated experimental programme enables to analyse crack initiating pore diameters within a single manufacturing batch.

Majority of the experimental work on “fatigue of material defects” rely on artificial defects in order to conduct a systematic study [116, 117]. By this way, size, location, and number of defects can be controlled, which enables a systematic investigation. On the other

Table 3.1 Summary of the experimental programme

Manufacturing	
Process	Laser powder-bed fusion
Manufacturer, model	EOS GmbH, M290
Powder	Pre-alloyed, grade 5 Ti64 powder
Process parameters	Proprietary information
Layer thickness	60 μm
Build direction	Vertical
Parts	60x rectangular blanks and 12x hourglass fatigue samples
Post-processing	
Heat treatment	Yes, at 800°C for two hours while build plate still attached
Surface roughness	Mechanical grinding and polishing Ra$\leq$0.2 as per ASTM E466
Characterisation	
Chemical composition	Inert gas fusion
Microstructure	Light (optical) microscopy
Porosity	X-ray Computed Tomography
Fatigue	Load controlled, constant amplitude axial testing at R=0.1
Fatigue crack growth	Small cracks using the Replica technique
Environment	in air, at ambient temperature

hand, morphology of an artificial defect can be suspect and whilst machining of defects residual stress fields can be introduced unintentionally. Furthermore in AM, it is theoretically possible to "print" a defect rather than machining as shown in the references [118, 119]. However, such printed defects were rather large so far, e.g. 500 μm in diameter, and filled with un-melted powder particles with rough interior surface, i.e. morphologically unrepresentative of process-induced defects. In this work, naturally induced defects that are inherent to the process were preferred over artificial defects due to the advantage of working with realistic defect morphologies and avoiding possible complications with artificial defects discussed so far. When working with uncontrolled, naturally induced defects, each fatigue test would lead to a single crack initiating defect dimensions and location, thus a large number of tests would be required to achieve statistically significant data. In order to overcome this limitation and extract more information per test, some of the samples were scanned using X-ray Computed Tomography prior to testing.

3.2 Manufacturing process

Samples for this work were manufactured using the laser powder-bed fusion technique by the industrial collaborator "EOS Electro Optical Systems Finland Oy" on their commercially available M290 model. A grade 5, pre-alloyed titanium Ti-6Al-4V powder was used as the feedstock material. A 60 μm layer thickness was selected by the manufacturer, which seems to be preferred by the major aerospace companies as seen in [35, 49, 120]. Process parameters were considered as proprietary information and undisclosed by EOS.

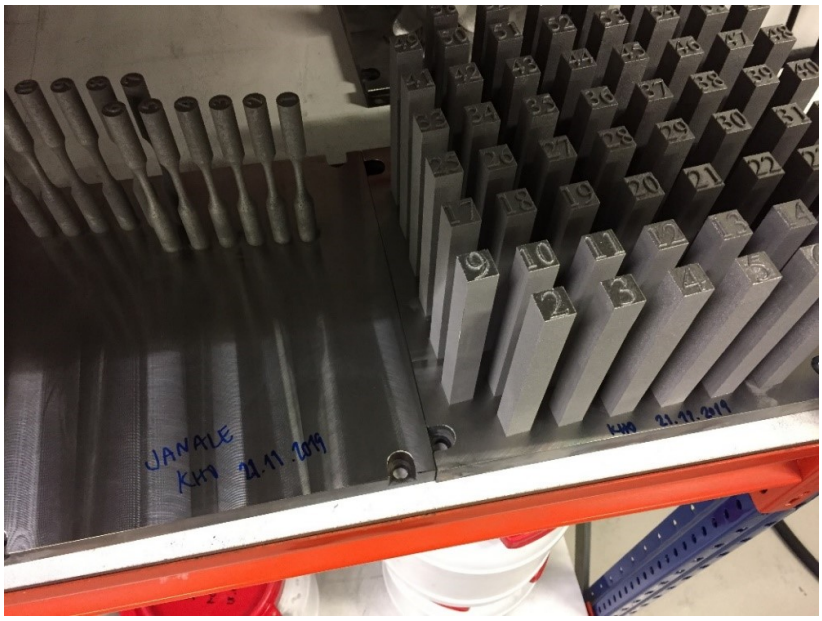

Fig. 3.1 Photograph of samples after manufacturing whilst still attached to the build plate.

Two different geometries were manufactured as shown in Figure 3.1, and the majority of them, e.g. 60 in total, were built as rectangular blocks. These blocks were considered as blanks from which a standardised test specimen geometry can be extracted for the subsequent mechanical testing stage. A rectangular geometry was preferred since it provides the flexibility of extracting both flat dog-bone test specimens and cylindrical hourglass test specimens. All the subsequent machining work to extract test specimens was conducted using the electro-discharge machining (EDM) technique.

In addition, a smaller batch of samples, e.g. 12 in total, were manufactured in the near-net shape of fatigue cylindrical hourglass test specimen geometry; the relevant dimensions can be found in Figure 3.10b. These near-net shape samples were mainly intended for porosity characterisation using X-ray Computed Tomography, which require thinner samples compared to the rectangular blanks, hence a better resolution can be achieved during scanning. Using X-ray Computed Tomography in conjunction with test specimens extracted from rectangular

blanks was avoided, since this would have provided a censored data. In other words, measured pore population would have been limited to the extracted test specimen location only, whereas near-net shape samples enable quantifying the entire porosity population within the manufactured volume. More discussion on the influence of X-ray Computed tomography on sample design can be found in Section 3.7.

As an example, the manufacturing set-up used for rectangular blocks is shown in Figure 3.2. The build plate seen in Figure 3.2 was 200 by 200 millimetres and the distance between the blanks was larger than 1 mm. Manufacturing was conducted in a protective argon environment to prevent oxygen pickup at high temperatures when the feedstock was melted. All samples were built in the vertical direction, in order to avoid the possible influence of build direction on mechanical properties as discussed in Section 2.5.5 of Literature Review. Vertical build direction was preferred over the horizontal direction to maximise the number of samples that can be manufactured in a single batch, hence avoiding a possible influence of batch-to-batch variation on mechanical properties.

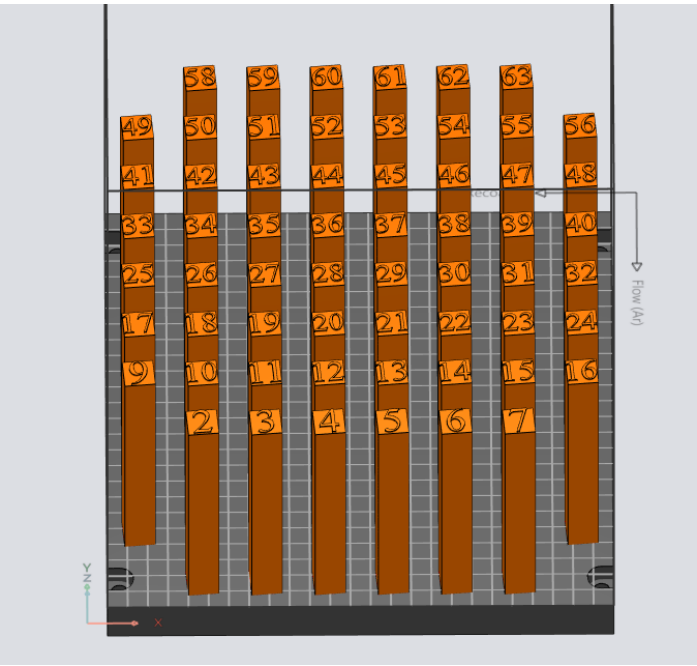

Fig. 3.2 Sketch of the manufacturing set-up. The rectangular blanks had 15 mm x 15 mm cross-section and were 120 mm tall.

3.3 Heat treatment

A stress-relief heat treatment was conducted to relieve residual stresses induced by the process, which could be up to 50% of the yield strength as discussed in Section 2.5.4 of the Literature Review. A stress-relief heat treatment is also recommended by current industry practices such as ASTM F2924 and it helps the aim of concentrating the influence of defects by removing the potential influence of residual stresses on fatigue.

After manufacturing, while the samples were still attached to the build plate, a heat treatment was conducted at 800°C in a vacuum furnace for two hours, followed by a room temperature cooling. These parameters are within the textbook values for stress-relief heat treatment for $\alpha + \beta$ titanium alloys [28, 29], and has been shown to relieve the residual stresses in L-PBF Ti-6Al-4V [34].

The heat treatment was below the recrystallization temperature of the Ti-6Al-4V, hence the morphology of the as-built is microstructure expected to remain roughly unchanged. A side benefit of this stress-relief heat treatment is the conversion of the undesired martensitic phase into a very fine $\alpha + \beta$ phase as discussed in [28].

3.4 Surface preparation

As discussed in literature review, the as-built surface roughness of the powder-bed additive manufactured titanium alloys could be higher than R_a=30 microns and fail exclusively from the rough surface under cyclic loading. Therefore, the as-built surface roughness was removed to study the influence of defects on fatigue performance.

For the purpose of removing surface roughness, successive mechanical grinding and polishing steps were conducted using abrasive silicon-carbide (SiC) papers and diamond paste respectively. Using papers with adhesively bonded SiC particles, successive grinding steps were conducted on the surface of fatigue samples with following particle sizes 60, 120, 300, 600, 1200 and 2500 as per the The Federation of the European Producers of Abrasives (FEPA) standard. After the final step of grinding, sample surfaces were polished using diamond paste with 15 and 6-micron grain size. In addition, for the samples in replica study, colloidal silica was applied to achieve a scratch-free surface to obtain better visualisation. The complete duration of the surface preparation process was around 3-4 hours per sample; during the process a longitudinal grinding and polishing motion parallel to loading axis was aimed, and the total amount of material removal was between 0.16 mm to 0.4 mm, noting that it was inconsistent due to the manual nature of the process.

Surface roughness of the samples was checked qualitatively using a light microscope at 25x magnification. A representative image of the samples surface prior to fatigue testing is provided in Figure 3.3, which conforms the ASTM E466 standard, i.e. no deep machining marks are evident as per Appendix X1 of ASTM E466.

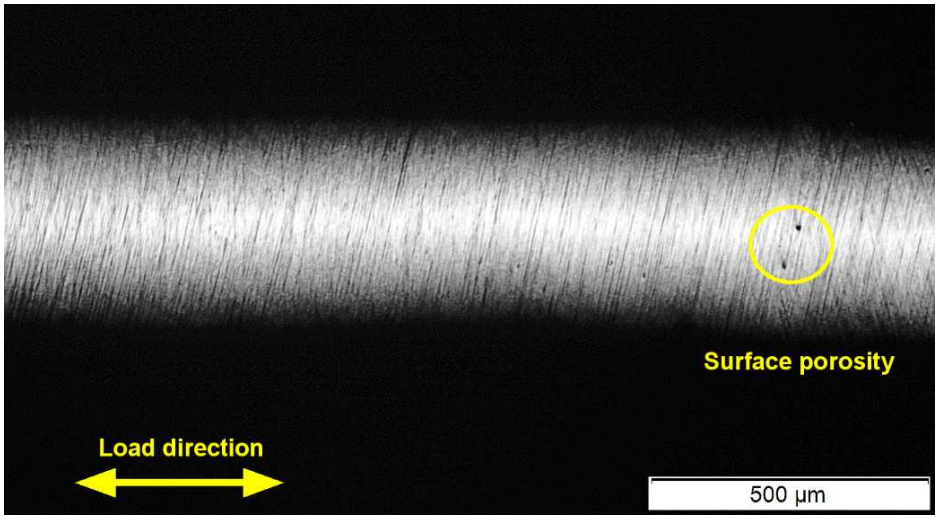

Fig. 3.3 Representative surface quality of a near-net shape manufactured hourglass sample prior to fatigue testing. The image obtained using light microscopy after grinding and polishing steps.

3.5 Microstructure examination

A microstructure examination was conducted to assess whether the samples used in this study were representative of the laser powder-bed fusion process. For this purpose, small pieces from rectangular blanks were sectioned in the build direction and transverse to the build direction. By following standard metallographic procedures, first sections were embedded in a resin using hot compression mounting for easier handling. Then, starting from 120-micron grit paper, sequential grinding steps were applied until 2500-micron grit size. Finally, the metallographic samples were polished using a colloidal silica (OP-S) to obtain a scratch-free surface. In order to reveal the microstructure, the samples were etched using the Kroll's reagent. Metallographic samples, which were obtained following the outlined procedure, were analysed using a light (optical) microscope.

3.6 Chemical analysis

The chemical composition of feedstock material (powder) was provided by the manufacturer as part of their internal quality control; this composition is expected to be preserved given that manufacturing chamber was sealed using an inert gas. However, due to the high reactivity of titanium with oxygen, an additional chemical composition analysis was conducted on the *manufactured* samples for verification. Oxygen atoms are small enough to fit between normal crystalline lattice locations, i.e. the so-called interstitial atoms; hence could lead to solid solution hardening. This in-turn has significant influence on the mechanical properties; for instance increasing the oxygen content improves strength but reduce ductility. From fatigue perspective, literature suggests that oxygen could change the deformation mode to planar slip which leads faster small crack propagation rates [28]. Due to the influence of oxygen on mechanical properties, ASTM F2924 standard limits the oxygen content of additive manufactured Ti-6Al-4V by 0.20% in weight, which is also a common specification for conventionally manufactured Ti-6Al-4V.

For measurement of the oxygen content, small cubes of $\sim$10 mm edge length were cut from the grip section of fatigue samples using a precision cutter. The measurement was conducted by an external, UKAS accredited company Element Materials Technology Ltd in Sheffield, UK according to their LECO analysis procedure. As part of the LECO analysis, the oxygen content of the manufactured samples was determined using the inert gas fusion technique.

3.7 Porosity characterisation

As discussed in the introduction, this work is concerned with naturally initiated defects, hence features of the crack initiating defect is unknown prior to fatigue testing compared to an experiment with artificially introduced defects. Therefore, in the scope of this work, morphology, size and location of pores inside the gauge volume of some fatigue samples were determined using non-destructive testing in order to compare crack initiating defect with the population of process-induced defects. The aim of this work item is to complement fatigue testing results.

Process-induced defects in AM are embedded within the material in the as-built condition and their dimensions are in the sub-mm scale, thus making it particularly challenging to quantify them using non-destructive testing. An overview of the available non-destructive testing techniques for porosity can be found in the Yearbook by The British Institute of Non-Destructive Testing [121] or more specifically for AM materials in ASTM E3166 [122]. In

this work, X-ray Computed Tomography technique was used since it is capable of detecting pores in the sub-mm scale, quantify their dimensions, visualise their morphology and spatial distribution. Furthermore, successful application of this technique in AM Ti-6Al-4V has been extensively demonstrated [12, 95, 15].

X-ray Computed Tomography

In X-ray Computed Tomography technique, an image is created based on the difference in X-ray absorption i.e. attenuation within a test volume. Although both terminologies are used in the literature interchangeably, attenuation is preferred in this work considering some of the incident X-rays are absorbed by the material and some are scattered away. Porosity defects, which are either argon filled or in vacuum, have a different density than the parent material, Ti-6Al-4V, hence can be detected using X-rays.

Fig. 3.4 Sketch of a typical laboratory scale X-ray Computed Tomography setup. The sketch originally published in [123] and reprinted by permission from Springer Nature

As illustrated in Figure 3.4, a typical industrial tomography setup consists of an X-ray source, a sample stage that is used to manipulate the position of a sample, and a detector, which measures the attenuation of travelling X-rays. Unlike the medical imaging, in an industrial tomography sample is rotated around its own axis, while the source and the detector stand still.

Amount of X-ray attenuation depends (1) on the equipment, i.e. the energy of generated X-rays, (2) on the sample geometry, e.g. thickness and (3) on the material, e.g. bulk density. Achieving sufficient X-ray attenuation was considered during fatigue sample design, hence discussed in more detail: The attenuation can be described by using the Beer-Lambert law for monochromatic X-rays. This law cannot be used quantitatively, because the type of X-ray source used in this project produces a polychromatic X-ray energy spectrum, in other words intensity of X-rays vary over the energy range. However, Equation 3.1 provides insight for sample design considerations and constraints.

$$\frac{I}{I_0} = e^{-\mu t} \tag{3.1}$$

where I_0 is the X-ray intensity generated by the source, I is the X-ray intensity after passing through the sample, μ is the linear attenuation coefficient that depends on equipment voltage (kV) and sample density, and t is the thickness of sample. In practice, somewhere between 10-30% attenuation is desired, i.e. ratio of I to I_0. Due to the exponential nature of the Beer-Lambert law, as the sample thickness increases, attenuation decreases rapidly. Having said that, the thinnest sample will not necessarily provide the best imaging either, since the high-energy X-rays produced by a high-voltage source, the so-called hard beams, would not be attenuated by the sample, therefore no image would be created. Therefore, an optimum sample thickness needs to be determined based on the X-ray source and material density. In this work, 5 mm diameter samples were used, which is large enough to be accepted by ASTM E466 as representative amount of grain size within a testing volume, and 20% attenuation was achieved during measurements as discussed later on.

In relation to X-ray attenuation and sample thickness, another consideration during experimental design was the sample geometry. A cylindrical dog-bone sample was used in this work because flat dog-bone samples owing to their high aspect ratio are ill-suitable for tomography measurements. This is illustrated in Figure 3.5.

In Figure 3.5 shows that as the sample rotates, incident X-rays has to traverse different thickness values marked by t and w. Considering the significant influence of material thickness on attenuation, there will be varying attenuation rates as the sample rotates. Despite some modern software algorithms could fix this problem up to a certain extent, a cylindrical sample geometry was used to avoid this problem completely.

μXCT setup and settings

In this work, process-induced defects were measured using the Nikon XTEK High Flux Bay micro-tomography, referred as μXCT from here afterwards, which is located in the

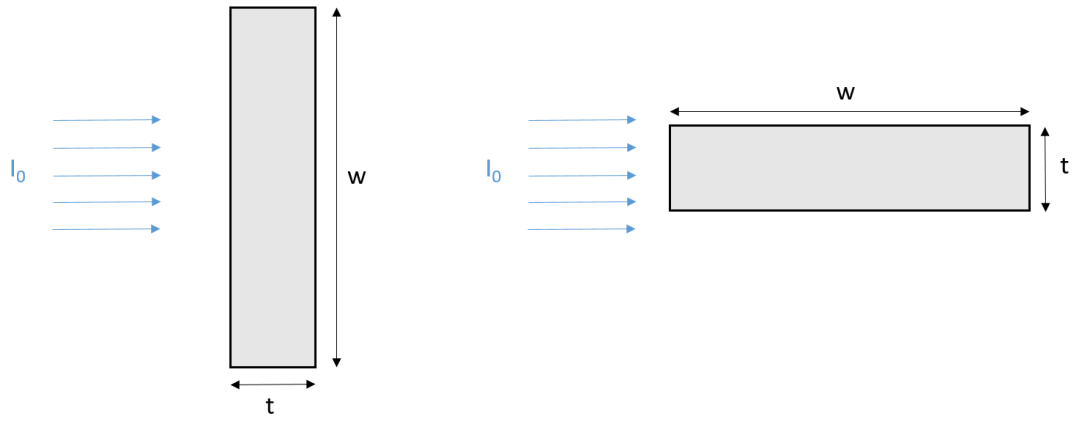

Fig. 3.5 Sketch demonstrating incident X-rays on a high-aspect ratio sample

Henry Moseley X-ray Imaging Facility (HMXIF) at the University of Manchester. It is equipped with a 225kV, 450W tube type X-ray source that has a 2-micron optimal spot size transmission rotating target. Detector is an indirect type, which first converts received X-rays into light by using a scintillator material and then converts this light into an electric current by using photoconductors. Finally produced electric current is used the display the image by the common thin film transistor technology which is the basis of many LCD screens.

First two measurements of the gauge volumes on near-net shape manufactured (hourglass) samples were conducted by the author using the settings provided in Table 3.2.

Table 3.2 μXCT settings for the first two samples

Parameter	**Value**	**Unit**
Voltage	190	kV
Current	32	mA
Power	6	W
Exposure	2	s
Distance from source to sample	31.1	mm
Distance from sample to detector	877.5	mm
Voxel	7.1	μm

Voxel size can be calculated by dividing the magnification factor, which is the ratio of distance between source and detector to source and sample, to the detector pixel pitch that was equal to 0.2 *mm* for the corresponding equipment used by Nikon. At the time of scanning, the detector was scheduled to be replaced; this is why roughly a 1.5 mm^3 volume were faulty as marked in Figure 3.6. Considering that all samples were failed due to surface porosity, this volume was not relevant from a structural integrity perspective. Furthermore, a 5% deviation

between μXCT measurements and design diameter was detected as shown in Figure 3.6. Thus, during analysis of the μXCT data, the voxel size was taken as 7.44 μm.

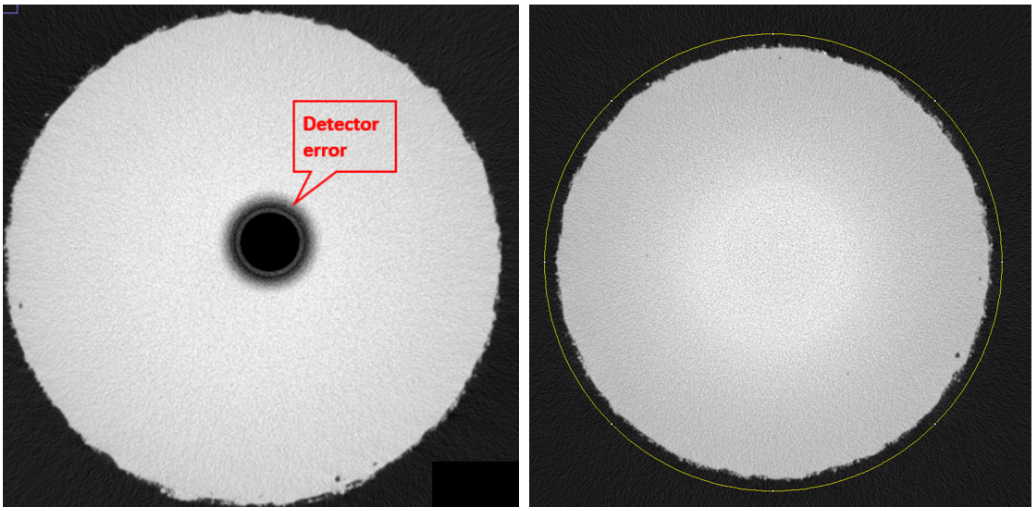

Fig. 3.6 Representative images from X-ray Computed Tomography of first two samples. (a) Detector error (b) Slight deviation in sample diameter

Afterwards the detector was replaced; however, due to the coronavirus pandemic that restricted travel, the remaining samples were scanned by the Senior Experimental Officer at HMXIF using the same parameters as in Table 3.2 except the following revisions in Table 3.3.

Table 3.3 μXCT settings for the remaining samples

Parameter	**Value**	**Unit**
Distance from source to sample	70.1	mm
Distance from sample to detector	1404.0	mm
Voxel	9.99	μm

Data processing and minimum detected pore size

This subsection describes the procedure followed to quantify the dimensions of porosity detected using μXCT. A Python script was written to implement the described procedure, which is provided in Appendix C, along with a comparison of results with a commercial software for verification.

The technique used for this purpose is referred as “image segmentation” in the literature. More specifically, a global threshold value was assigned to create a binary image between

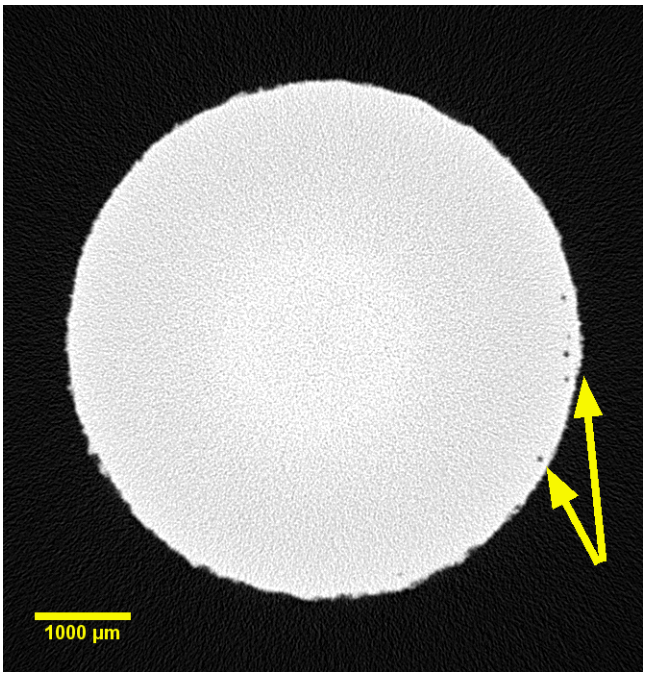

Fig. 3.7 Representative image of X-ray Computed Tomography after detector replacement and according to settings given in Table 3.3. Arrows are pointing to the detected pores.

black (grey level = 0) and white (grey level = 255) from the original scan data. This step, as expressed in Equation (3.2), was carried out by using the open source software ImageJ [124].

$$B(i,j) = \begin{cases} 0 & \text{if} \quad I(i,j) \leq t \\ 255 & \text{if} \quad I(i,j) > t \end{cases} \tag{3.2}$$

In Equation (3.2), i and j refers to the location of a pixel in the 2048x2048 grid. Intensity function, I, has the initial grey level values between 0 and 255 obtained from the μXCT. These pixels were assigned either black or white colour based on the specified threshold value, t. New binary image, represented by the function B, consists of black and white pixels only. An example image is given in Figure 3.8.

Threshold value was determined by using the Otsu algorithm [125] provided in the ImageJ software. By this way, grey level intensity variation between the individual images were taken into consideration as selected algorithm was applied to each image independently, rather than applying the same threshold value to every image. Furthermore, operator bias was reduced to picking the algorithm only; hence, the procedure can be reproduced. As an example, Figure 3.9 is provided to visualise the procedure.

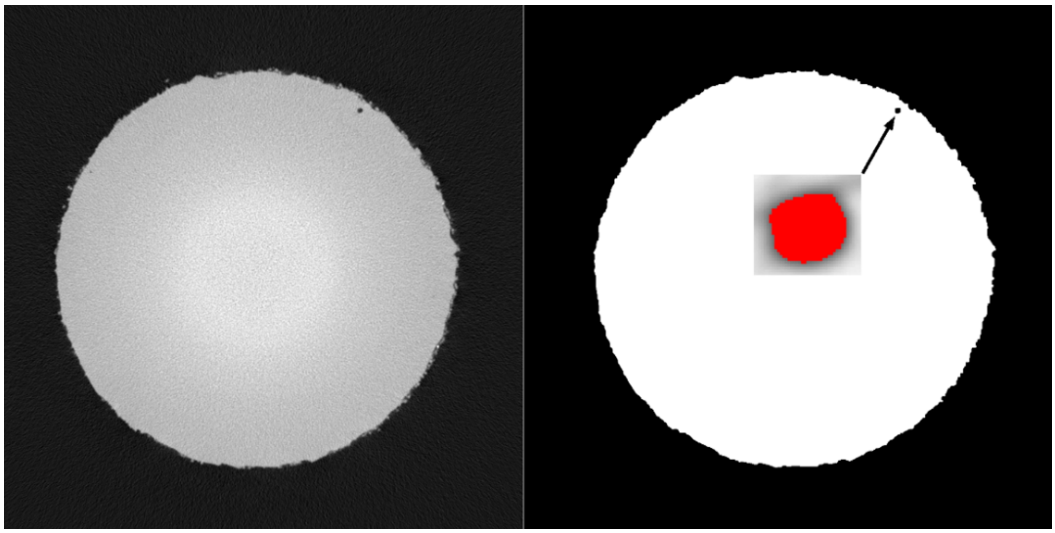

Fig. 3.8 Example output of the image segmentation step

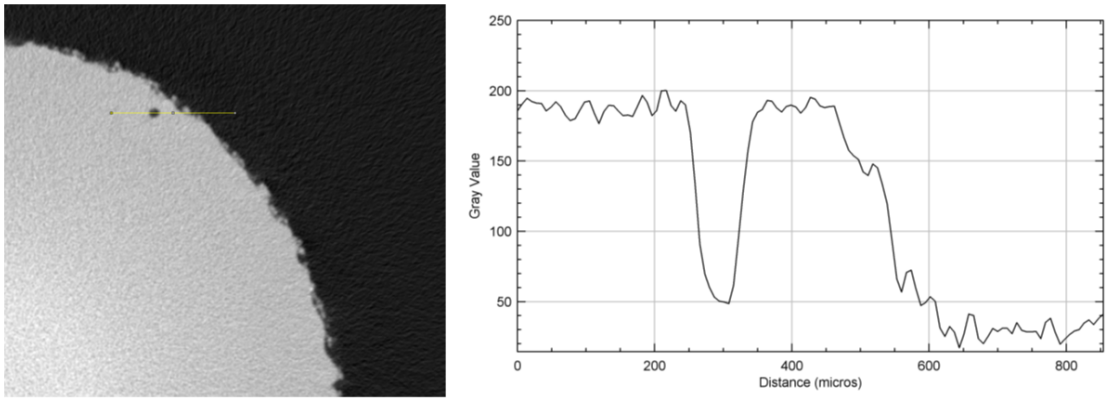

Fig. 3.9 Detailed look at the image segmentation step

Figure 3.9 is a representative slide consists of bulk material, porosity and the surrounding air. A line was drawn to show change of grey level intensity along it. Figure 3.9 shows that there are two different grey levels. First one, around 200, corresponds to the material, whereas air and the porosity is around 50. Otsu algorithm finds this difference by minimizing the interclass variance for the whole histogram.

As shown in Figure 3.9, the classification of a voxel as pore depends on the difference in grey level values of the surrounding voxels, in other words a single voxel is insufficient to detect a pore. Minimum two voxels are required to compare grey level values and given the 3D nature of X-ray Computed Tomography scans, a cut-off value of 2x2x2 cubic voxels was selected as detection limit, i.e. pores larger than 8 cubic voxels were counted. Consequently,

the smallest measured pore in this work was 26 μm in diameter by assuming a spherical pore morphology and by using the largest voxel size of 10 μm as reported in Table 3.3.

It should be noted that the selected detection limit was a subjective decision but shared among other researchers in the field as well [56, 126, 127, 128, 129], thus enabling the possibility of direct comparison with other reported X-ray Computed Tomography scans. However, more quantitative analyses [130, 131] suggest using at least 5 voxels, i.e. 125 cubic voxels, within the feature of interest for an accurate detection.

3.8 Static properties

Tensile testing was conducted by the equipment manufacturer (EOS GmbH) to determine static properties of L-PBF Ti-6Al-4V. The testing was according to the ISO 6892-1 standard [132] using cylindrical test specimens with 4 mm gauge diameter and 16 mm gauge length. The test results are given in Table 3.4, which correspond to test specimens that were built using the same machine model, e.g. EOS M290, same heat treatment, and same built direction as in this work.

Table 3.4 Static properties of L-PBF Ti-6Al-4V

Ultimate tensile strength (MPa)	Yield strength at 0.2% strain (MPa)	Elongation at break %	Reduction in area %
1075	965	14	25

3.9 High cycle fatigue testing

Fatigue in presence of manufacturing defects was studied for the case of axial loading, without the influence of environmental conditions, e.g. in air, at ambient temperature. Instead of aiming for an S-N curve, the fatigue testing strategy was repeating tests at selected load levels to determine fatigue life variability owing to the change in defect population.

Load-controlled, constant amplitude fatigue tests were conducted at a stress-ratio of R=0.1 following the recommendations given by the industry standard ASTM E466 [41]. Cyclic loading was applied using a servo-hydraulic actuator at a 10 Hz frequency. The actuator was a commercially available product from the company Instron with 100 kN maximum capacity. The calibration of the actuator load cell was inspected at regular intervals by an independent organisation, e.g. United Kingdom Accreditation Service (UKAS). The alignment of the loading axis was maintained by the industrial collaborator TWI Ltd. using a strain-gauged

alignment transducer as per ASTM E1012, hence a significant out-of-plane bending of the test specimens was unlikely. In addition, test specimens with a flat rectangular geometry are susceptible to in-plane bending due to eccentric mounting; a reasonably straight test specimen mounting was ensured by using a combination of a T-corner joint and a Vernier calliper. Given the best practice measures were taken and small dimensions of the fatigue test samples, a further investigation of the additional bending stresses using strain gauges were not carried out.

Two types of sample geometries were used in this work for fatigue testing, namely flat dog-bone samples and cylindrical hourglass samples as shown in Figure 3.10. The motivation behind using different geometries was related to supplementary measurements, e.g. a cylindrical geometry allow incident X-rays to pass through a constant thickness during μXCT measurements, whereas a flat test sample surface allow examination of a larger area during replica measurements. The influence of supplementary measurements on fatigue test sample design is more thoroughly discussed in their corresponding sections, e.g. Sections 3.7 and 3.10.

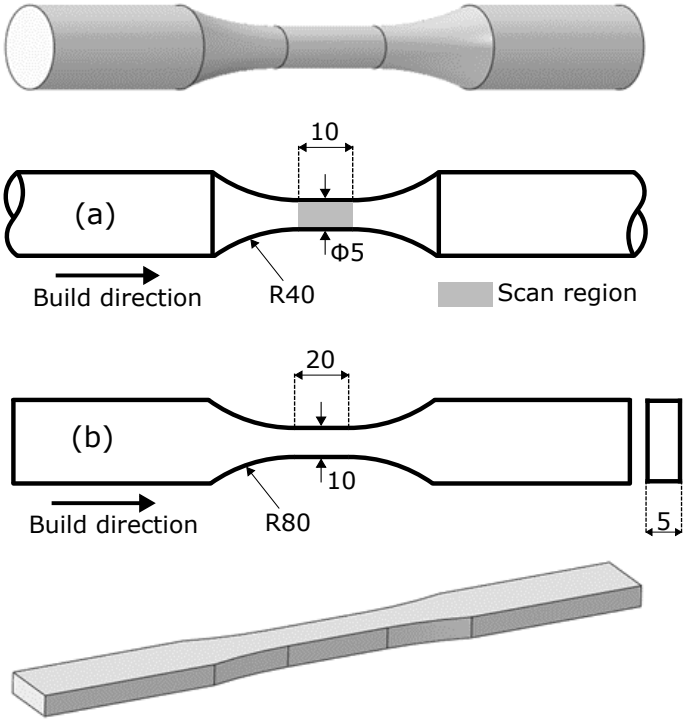

Fig. 3.10 Sample geometries used in this work for fatigue testing of L-PBF Ti-6Al-4V. All dimensions are given in millimetres.

The sample dimensions given in Figure 3.10 were according to the ASTM E466 standard, e.g. the test volume was large enough to contain a representative amount of grains for a bulk material response, and the transition radius was eight times the test diameter or width to ensure samples fail from the gauge section. As previously mentioned, electro-discharge machining (EDM) was used to extract desired sample geometries from the rectangular blanks shown in Figure 3.2. Furthermore for the case of cylindrical sample geometry, a limited 12off set of near-net shape manufacturing was also conducted as shown in Figure 3.1.

Due to the geometry change that was necessary for supplementary measurements, the gauge volume of fatigue samples was different. This raises a question about the so-called size effect in fatigue and fracture, e.g. for nominally similar materials, larger samples have lower (fatigue) strength due to the increased probability of weakest positions such as unfavourably oriented grain or a defect. A potential size effect was not investigated further based on the following arguments: (1) Minor effect in tensional loading in comparison to bending or torsion. (2) ASTM E466 standard allows sample size between 5-25 mm, meaning that a strong size effect is not expected within this range. (3) A recent work [133] reports an insignificant size effect from L-PBF built samples with 8 mm diameter (2000 mm^3) and 5mm diameter (200 mm^3) gauge sections, if the crack initiation source is the same, e.g. pore or lack of fusion defect.

3.10 Fatigue crack growth measurements

It is widely observed that cracks initiate early in fatigue life in presence of defects [134]. In this case, fatigue life will be controlled by crack-tip stresses instead of the defect geometry, hence the motivation behind this item in the Experimental Programme. Instead of performing fatigue crack growth measurements as per international standards such as ASTM E647 [84] using an artificial through-thickness crack, growth of naturally initiated cracks were measured during high cycle fatigue testing. This is mainly because the similitude condition in presence of small fatigue cracks initiated from defects might be unfulfilled, as discussed in Section 2.8 of Literature Review. For small crack growth measurements, an industry standard is unavailable at the moment but the recommendations given in Appendix X3 of ASTM E647 and experiences gathered in Proceedings of European Structural Integrity Society [135, 136] were considered for the experimental plan described in the following.

The replica technique was used to measure the growth of fatigue cracks naturally initiated from process-induced porosity during some of the high cycle fatigue testing as described in Section 3.9. This technique is limited to surface observations, thus only crack length can be measured under normal circumstances, and crack depth has to be either inferred or

measured using an alternative technique. Compared to microscopy approaches, where the crack initiation location must be known beforehand and the microscope lens must be focused on that particular point, the replica technique allows capturing a large area. This feature was particularly useful when dealing with process-induced defects because the crack-initiating pore was unknown beforehand.

In the replica technique, materials with low surface tension are employed to capture surface topography of a fatigue sample. A typical workflow can be described as follows: first the fatigue testing is briefly interrupted to apply the replicating material on the sample surface. After drying of the replicating material, it is peeled away and stored for subsequent analysis under an optical or electron microscope. At this stage, the surface of the fatigue sample needs to be cleaned in order to remove any remaining debris and the fatigue testing is re-started until the next scheduled interruption. Until failure of the sample, such replica exemplars of the sample surface are taken at pre-scheduled intervals. Finally, by tracing back from the final replica until the first one, crack length measurements can be obtained under a microscope. A representative surface from this work is given in Figure 3.11.

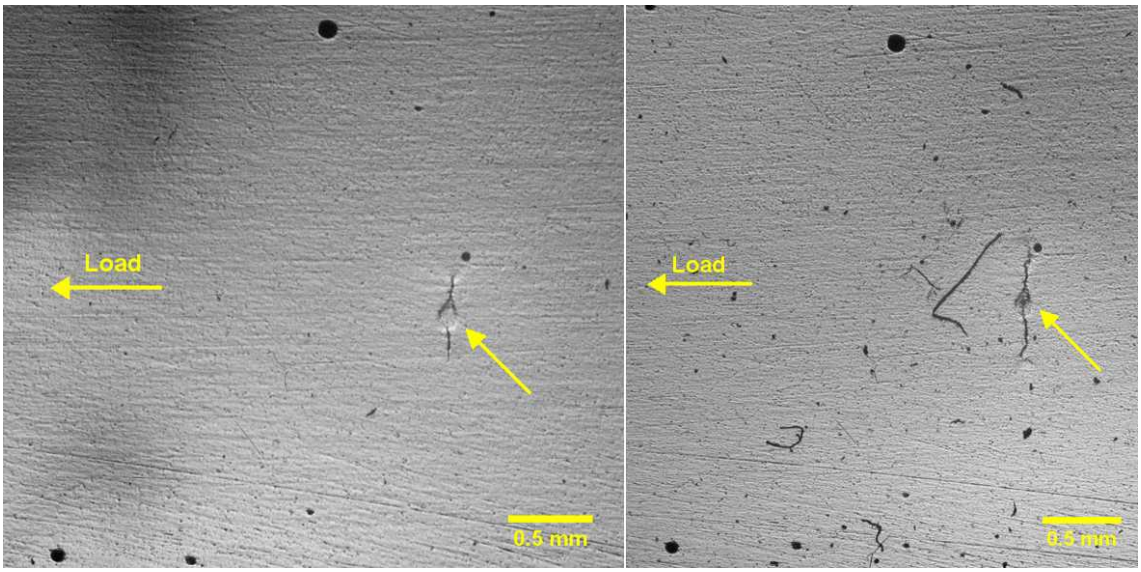

Fig. 3.11 Representative image from the replica measurements. Image on the left shows first crack detection from porosity, whereas image on the right shows subsequent crack propagation captured.

Arguably, the most common replicating material is acetate sheets. Prior to application, acetate sheets are softened with a solvent such as acetone, then lightly pressed on the surface on interest. During trials, acetate sheets with two different thicknesses were employed. The thick acetate sheets were unable to capture small cracks below 0.5 mm. On the other hand, the thin acetate sheets were able to capture the small cracks; however, they require a certain

level of operator skill: easy to tear apart if too much solvent was applied and air bubbles were observed to form if not pressed on the surface properly. Furthermore, since acetate sheets are transparent, they require an additional contrasting material for observation under light microscopy.

In this work, silicon-rubber type compounds were used as the replicating material mainly due to their ease of use compared to acetate sheets. Commercial products are available with dispensing gun, in which the replicating material can be applied to the surface of interest relatively easily by pointing and dispensing without much danger of any air bubbles. Compared to acetate sheets, their curing time was also much quicker, e.g. less than five minutes, and they do not require any additional contrasting step for the light microscopy afterwards. For electron microscopy, a gold coating or similar is required for improving the conductivity of the silicon-rubber.

Most of the silicon-rubber replicating materials are fluid when dispensed, hence making them unsuitable for tensile fatigue testing conditions where gauge surfaces are perpendicular to the ground as opposed to bending tests where gauge surfaces are parallel to the ground. In tensile testing environments, since gravity pulls the replicating material away from the surface, a suitable measurement cannot be obtained. Some manufacturers offer thixotropic compounds as well that have a toothpaste like consistency, making them ideal for conditions where gravity plays a role. Commercially available thixotropic replicating materials from the company Struers Ltd. were used in this work. The company offers two compounds, namely T1 and T3. During trials, it was observed that T3 type compound was unable to capture surface breaking cracks; hence, T1 compound was used throughout the experimental programme. It should be noted that this is a trial and error process, and different compounds seem to be working as well [137].

Although usage of replicating materials with curved surfaces were demonstrated in the literature [138], these works were mainly notches where crack initiation is limited to a small region at the tip of a notch. For cylindrical hourglass samples, cracks could initiate from anywhere on the gauge surface, making it an infeasibly large area to analyse under microscope. Furthermore, curved surfaces are mainly incompatible with optical microscopes, and stretching replicating material to make it flat could lead to erroneous results. Therefore, flat dog-bone samples were used for the replica measurements. The dimensions of these samples can be found in Figure 3.10.

Procedure

Replica measurements were taken at two different stress ranges, e.g. $\Delta\sigma$ = 540 MPa and $\Delta\sigma$ = 360 MPa. During high cycle fatigue testing as described in the previous section,

tests were briefly interrupted every 10,000 cycles to apply the replicating material. During replication process, a mean tensile load was applied to aid crack opening and in less than five minutes, fatigue testing was re-started after curing of the replica. Once the crack reached to a size where it is possible to detect via naked eye, i.e. somewhere between 0.5 mm to 1 mm, replicating interval was reduced to 5,000 cycles for accuracy during data reduction stage. After fatigue testing, replica exemplars were traced back from the last cycle to the first replication interval using a light microscopy. Projected crack length perpendicular to the applied load direction was measured using the proprietary software of the Zeiss light microscope. For every crack length measurement, at least three observations were taken.

The fatigue life of some titanium alloys is reduced drastically, if the applied cyclic loading has a trapezoidal shape, i.e. held constant at maximum stress for longer than two minutes, which is known as the dwell fatigue (Section 6.4.1 in [28]). This phenomenon is not expected arise due to the replication intervals because of the following: (1) Ti-6Al-4V typically exhibit negligible susceptibility to dwell fatigue. (2) A mean tensile load was applied during replication, not the maximum applied stress. (3) Replication intervals were infrequent i.e. every 5,000 to 10,000 cycles, whereas in dwell fatigue the maximum stress is held constant in every cycle.

3.11 Wire+arc additive manufacturing

In addition to the experimental programme described so far on L-PBF process, a previous PhD study [15] from the same research group was expanded by fatigue testing of the remaining twelve test samples. As can be inferred from the Section title, these samples were manufactured using a different AM process, namely wire+arc additive manufacturing (WAAM). They were useful in understanding of the influence of pores on fatigue performance, because some samples were manufactured using contaminated wires, as a result it was possible to examine a large variety of crack initiating pore diameters, ranging from roughly 20 microns to 400 microns. A detailed information about the WAAM experimental programme can be found in [15]. In order to make this thesis self-contained, following information is extracted from [15], except the fatigue test results which are reviewed and interpreted in Chapters 4-5.

3.11.1 Sample manufacturing

A set of two wall shaped, 27 mm thick manufacturing blanks with 300 mm width and 160 mm height were deposited on a 12 mm substrate material by using the plasma arc equipped

HiVe machine located at the Cranfield University. An oscillation build strategy was followed using 1.2 mm diameter, AWS 5.16 specified Ti-6Al-4V wires as the feedstock material. A sketch of this process is provided in Figure 3.12. During manufacturing, some of the wires were intentionally contaminated by spraying a WD-40 solution on the wire surface. The decomposition of the organic contaminant when subjected to plasma heating generates gases to promote porosity formation, which was found to be a non-intrusive approach [139, 140].

Fig. 3.12 (a) Sketch of the WAAM process as published in [141] (b) Extraction of samples from manufactured blanks in [142]

From the wall shaped manufacturing blanks, cylindrical hourglass shape fatigue samples were extracted using electro-discharge machining and lathe turning. Residual stresses developed during processing were expected to be relaxed, when the deposited material was cut from the substrate material. Furthermore, tensile residual stresses were found to be located close to the substrate [64], which corresponds to the grip section of fatigue samples, i.e. far away from the gauge (test) section as seen in Figure 3.12(b).

Fatigue testing conditions were nominally similar compared to the conditions described so far in this work. The build direction in manufacturing was parallel to the loading direction of fatigue testing as seen in Figure 3.12(b). Gauge section dimensions of the samples were 5 mm diameter and 13.5 mm length, which are similar to the L-PBF samples from the experimental programme developed in this thesis, as shown in Figure 3.10. Prior to fatigue testing, surface roughness was removed similar to the procedure described in Section 3.4. Fatigue testing as per ASTM E466 was followed in air at ambient temperature.

3.11.2 Chemical composition

A chemical analysis was conducted using small samples extracted from manufactured walls, which were subject to the same procedure explained in Section 3.6. The results are summarised in Table 3.5.

Table 3.5 Chemical composition of WAAM Ti-6Al-4V samples in wt.%

Source	Al	V	O	N	H
Clean wire	5.61	3.80	0.18	0.008	0.006
Contaminated wire	5.89	3.80	0.17	0.017	0.007

As discussed in Section 3.6, the main purpose of chemical analysis in this work was to check the oxygen content, which could influence the mechanical properties. The measurement results in Table 3.5 were deemed satisfactory as the oxygen content was below the 0.20% weight specified in ASTM F2924 standard.

3.11.3 Microstructure

Three metallographic sections were extracted from the manufactured wall in XY, XZ, and YZ planes as per Figure 3.12. The exact spatial and build height locations of these sections were not disclosed in the original work. The extracted sections were subjected to successive grinding and polishing steps similar to the procedure given in Section 3.5. Then, polished and etched metallographic sections were analysed under optical microscopy to quantify α lath

thickness using the intercept method according to ASTM E112. The revealed microstructure is shown in Figure 3.13.

Fig. 3.13 Microstructure of WAAM Ti-6Al-4V as captured by optical microscopy. (a)-(c) macro views, (d)-(e) zoomed-in views. Originally published in [15].

In macro views of Figure 3.13, columnar prior-β grains can be observed, which are a characteristic feature of metal additive manufacturing so far and related to the directional solidification as discussed in Section 2.4. The width of prior-β grains were reported to be between 1 mm to 3 mm, which is an order of magnitude larger than the L-PBF process values reported in [36, 69, 59]. From the zoomed in views, it can be seen that α plates are generally more orderly compared to the L-PBF microstructures shown later in Figures 4.8-4.9, which suggests different cooling rates as expected from different energy sources, e.g. laser versus arc, used in manufacturing. The width of the α colony structure was reported to be between 20 μm to 30 μm, whereas the individual α laths were on average 3 ± 0.7 μm, which is considerably coarser than the reported values in Table 4.2 for L-PBF process used in this work. Finally, the author also reported an α lath thickness 1 ± 0.2 μm on localised regions, and an example of this difference in α lath thickness within the same microstructure can be observed by comparing Figure 3.13(d) and (e).

3.11.4 Porosity

Destructive and non-destructive analyses were carried out for porosity measurements. For the former, metallographic sections were extracted and polished, which were subsequently investigated to determine porosity statics; unfortunately the total number of sections, the location of sections, and the total area of sections were not disclosed. For the latter, an X-ray

CT was conducted to measure bulk density within gauge volumes of fatigue test samples extracted from both cases, i.e. clean and contaminated wires. A 20 μm voxel size was reported, which is twice as large the value obtained in this study. Unfortunately, the total number of samples used in X-ray CT study was not provided.

Bulk density was measured as 99.99% for the clean wire case and 99.96% for the contaminated wire case using X-ray CT; no further statistics were reported from this measurement. Using metallographic sections, $\sim$17 pores were detected for the clean wire case with a mean pore diameter of 62$\pm$23 μm and $\sim$48 pores were detected for the contaminated wire case with a mean pore diameter of 206$\pm$80 μm. Although the number of pore observations were limited in metallographic sections, in both instances the mean pore diameter is larger than the L-PBF samples used in this work as discussed later in Section 4.3.3.

3.11.5 Static mechanical properties

For each condition, e.g. clean versus contaminated wire, 4off tensile testing in air, at ambient temperature was carried-out using flat test specimens as per the ASTM E8 standard. The test specimen was 5 mm thick with a gauge section of 25mm long and 6 mm wide. The test results are presented in Table 3.6, which correspond to a strain rate of 0.06 min^{-1}.

Table 3.6 Static properties of WAAM Ti-6Al-4V

Source	Ultimate tensile strength (MPa)	Yield strength at 0.2% strain (MPa)	Elongation at break %
Clean wire	859$\pm$4	802$\pm$7	10$\pm$2
Contaminated wire	842$\pm$8	825$\pm$5	4$\pm$1

From Table 3.6, it can be seen that static mechanical properties between two cases were similar, except the significant difference in elongation. As expected, the elongation of samples fabricated from contaminated wires was lower due to the increased defect density, which influences the ductility as reported widely in literature [26, 59, 143, 144, 127, 145]. In this specific instance, the static mechanical properties of WAAM Ti-6Al-4V were lower compared to L-PBF Ti-6Al-4V, which are given in Table 3.4.

3.12 Summary of the fatigue testing programme

The fatigue testing programme described so far is summarised in Table 3.1 for convenience.

Table 3.7 Summary of the fatigue testing programme[1].

Process	Source	Specimen geometry	Surface quality	Number of tests	Maximum stress (MPa)	Environment	ID[2]
L-PBF[3]	Near-net shape Fig 3.1	Cylindrical Fig 3.10a	Mechanically ground and polished	12	600, 500, 400, 335	in air, at RT	NNS
L-PBF	Rectangular blanks Fig 3.2	Cylindrical[4] Fig 3.10a	Mechanically ground and polished	3	655, 600, 535	in air, at RT	DF
L-PBF[5]	Rectangular blanks Fig 3.2	Flat[4] Fig 3.10b	Mechanically ground and polished	11	600, 400, 270	in air, at RT	-
WAAM	Clean wire	Cylindrical Fig 3.12a	Mechanically ground and polished	6	800, 500	in air, at RT	-
WAAM	Contaminated wire	Cylindrical Fig 3.12a	Mechanically ground and polished	6	500	in air, at RT	-

(1) All fatigue tests were carried out under load control at a stress ratio of R=0.1 using a loading frequency f=10 Hz.

(2) Refers to sample identification system given in Appendix A.

(3) Test (gauge) volumes of some specimens were scanned using X-ray CT as marked in Appendix A.

(4) Desired sample geometry was extracted from rectangular blanks using electro discharge machining (EDM).

(5) As marked in Appendix A, flat test specimens were used in replica method to measure fatigue crack growth rates.

Chapter 4

Results and discussion

4.1 Introduction

Figure 4.1 shows the structure that was followed for presenting the experimental results, including the interpretation of experimental data provided in Chapter 5. The focus of this work is fatigue, hence the sections were divided accordingly. In Figure 4.1, the information given in parentheses identifies the AM procedure from which the experimental data was derived, i.e. individual sections do not mix and match different AM processes. For example Section 4.4.3 presents the fatigue crack growth measurements, which the experimental data was obtained from samples fabricated using the L-PBF process.

4.2 Local stress distribution in the vicinity of a pore

4.2.1 Introduction

The aim of Section 4.2 is to review local stresses in the vicinity of a pore by means of analytical solutions available in the literature and by constructing a simplified finite element model to visualise the problem. Using the finite element model, mechanics relevant to fatigue are summarised in this section, which serves as an introduction to the problem. Furthermore, some of the mechanics presented here provides context for the discussion of experimental results later on, e.g. the influence of pore size on stress concentration factor and on fatigue endurance test results, the expected crack initiation location and its influence on replica measurements.

Local stresses in the vicinity of a pore are higher due to the pore geometry, which could explain process-induced pores in additive manufacturing being preferential locations for crack initiation under cyclic loading as discussed in the Literature Review. The morphology of

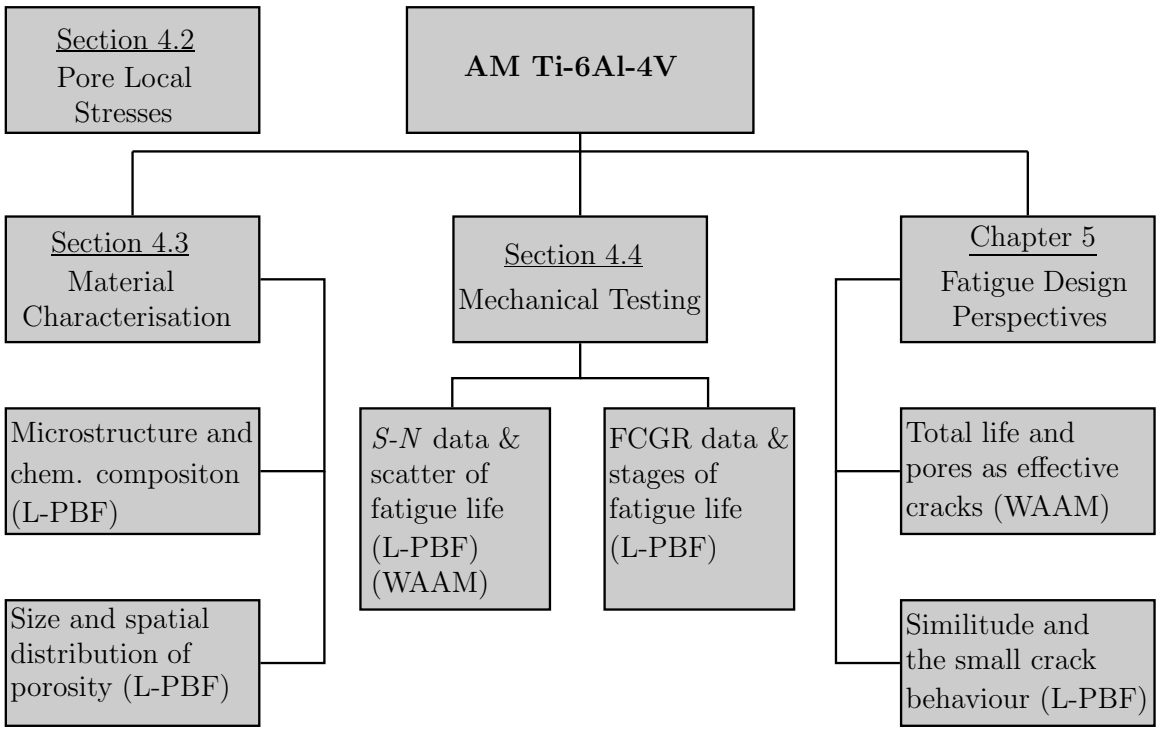

Fig. 4.1 The structure of results

process-induced pores can be approximated as spheres based on the experimental observations available in the literature [146, 126, 12] and Section 4.3.3 of this study as well. These spheres are expected to be filled with vacuum for the case of keyhole pores or filled with an inert gas, which is used extensively across the processing chain. In either case, pores cannot carry any load, hence can be assumed as cavities (voids). Finally, given that the diameter of process-induced pores are in the sub-mm scale, they will be extremely small compared to the gauge volumes of the test samples used in this work, which were in the range of 196-800 mm^3, and as well as for most of the industrial applications. Thus, the problem of process-induced porosity in additive manufacturing can be generalised as spherical cavities embedded in infinite bodies.

4.2.2 Stress concentration factor of a pore

For the case of axial loading used in this work, analytical solutions are available for the local elastic stresses near a spherical cavity embedded in an infinite body; e.g. Southwell and Gough [74], Goodier [147] using the theory of elasticity and Eshelby using the inclusion method [148]. Inside a linear-elastic material regime, the stress concentration factor of a pore in an infinite body can be calculated using Equation (4.1), where stress concentration

factor is defined as the ratio of local elastic stress divided to a far-field nominal stress. This equation was derived from the available analytical solutions discussed so far and can also be found in popular reference books such as the Peterson's Stress Concentration Factors [76].

$$K_t = \frac{27 - 15\vartheta}{14 - 10\vartheta} \tag{4.1}$$

where ϑ the Poisson's ratio and was assumed as 0.34. Thus, the stress concentration factor (K_t) of a spherical pore equals to 2.067 for a titanium alloy Ti-6Al-4V. It should be noted that, this value of K_t, e.g. 2.067, is valid for all materials with the same Poisson's ratio based on Equation (4.1).

Furthermore, K_t is independent of the pore diameter as can be observed from Equation (4.1). This might challenge the basic intuition that larger pores are more detrimental. However, K_t depends on loading and geometry only. Given that pores are embedded in an infinite body, the stress concentration factor is unaffected by the change in pore size, i.e. radius of curvature (geometry).

4.2.3 Finite element model

A commercially available software, namely ABAQUS Version 2021 [149], was used to perform finite element analysis in this work. A 3-dimensional model with a single spherical pore was used throughout. Using a 3D model instead of a 2D or axisymmetric model made it possible to consider Poisson's contraction of a pore under axial loading and as well as the influence of pore location on local stress distribution. The 3D geometry was selected as a cube with 1 mm edge length, which is often referred as a representative volume element (RVE) in multiscale problems. The finite element model, alongside with material parameters are shown in Figure 4.2.

As seen Figure 4.2, only 1/8th of the cube was modelled to be computationally efficient; in this model a 1 MPa unit axial load was applied in the Y-direction and symmetry planes were defined in X-Y, X-Z and Y-Z directions as boundary conditions. Despite the finite boundary conditions, the size of modelled pore was sufficiently small compared to the body in order to simulate the infinite body condition. Given that stress concentration factor is related to stresses in the elastic regime, a linear-elastic material constitutive behaviour was considered adequate. The elastic modulus was set to 114 GPa and Poisson's ratio was set to 0.34.

It should be noted that for some stress ranges used in this work, a degree of localised plastic deformation is expected as the local elastic stress exceeds the yield strength of the material. For instance, majority of the fatigue testing was replicated at 600 MPa maximum

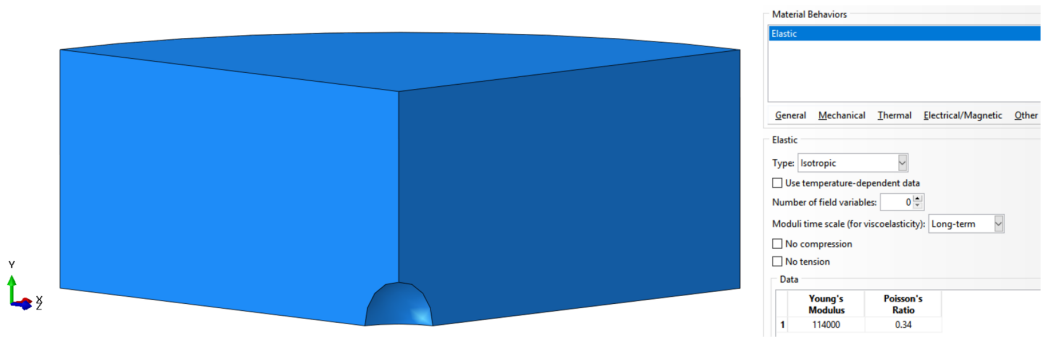

Fig. 4.2 Finite element model alongside with material properties. A unit axial load was applied in Y-direction and symmetry boundary conditions were defined in X-Y, X-Z and Y-Z directions.

stress, which exceeds the yield strength of 965 MPa given in Table 3.4 when stress concentration factor of 2.067 is taken into account. However, throughout this work, fatigue design approaches based on far-field (nominal) stress measures were considered. Given that the test specimen was strictly limited to elastic regime, the local plasticity in the vicinity of a pore was not considered in this work.

Mesh convergence analysis

Second-order hexahedral brick elements were used, which are shortly referred as C3D20 in ABAQUS. Mesh size was set to 100 microns globally, but a local mesh refinement was performed near the pore. In comparison, global mesh size of 100 microns is significantly larger than the individual α lath thickness of 0.5-1.5 microns seen in L-PBF process presented in Section 2.4, which is line with the homogeneous material behaviour assumption as discussed in Section 1.3. A representative meshing of the geometry is shown in Figure 4.3.

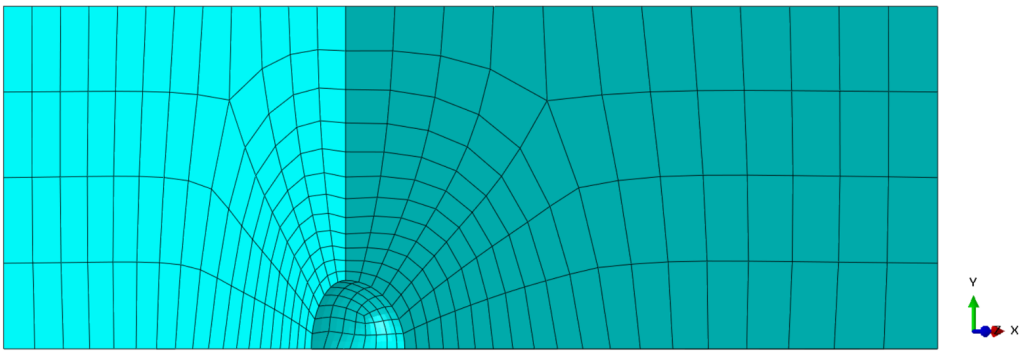

Fig. 4.3 Finite element mesh

The numerical model described so far was verified using the analytical solution given in Equation 4.1. For this purpose, a mesh convergence analysis was conducted by gradually refining mesh size and the analysis results are given in Figure 4.4.

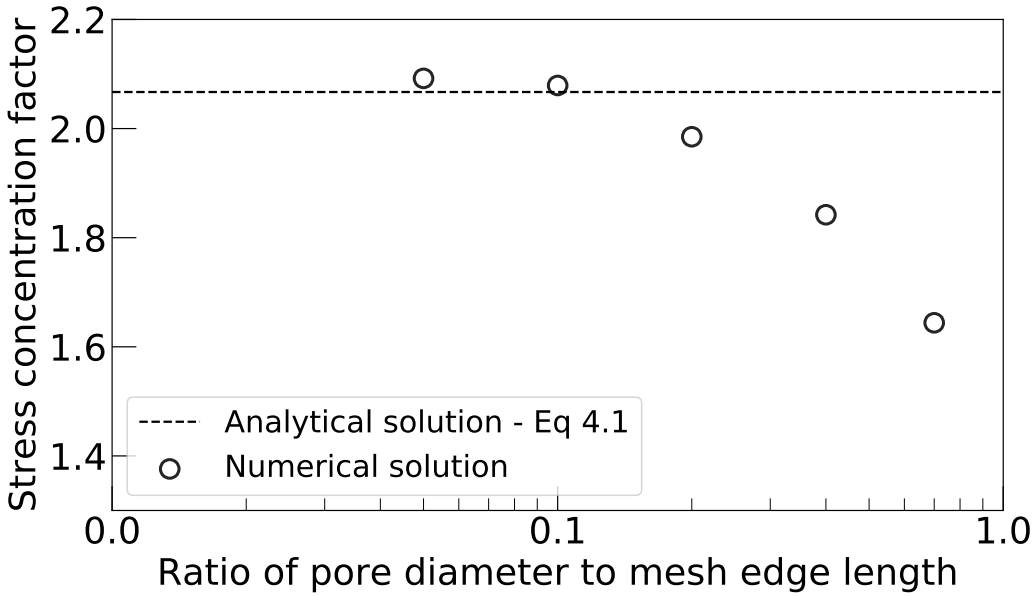

Fig. 4.4 Mesh convergence study

Figure 4.4 shows the stress concentration factor calculated using the gross section area for different mesh edge lengths, which were normalised using the pore diameter. When the ratio of the edge length of a brick mesh to the pore diameter was less than 0.1, the numerical solution of the stress concentration factor was converged to the analytical value of approximately two as seen in Figure 4.4. The numerical results presented in the remainder of this Section were calculated with respect to the converged mesh and the verified numerical solution.

4.2.4 Local elastic stress distribution

For the stress component parallel to the applied load direction (σ_{22} or σ_Y), the distribution of local stresses near a pore is given in Figure 4.5, which displays Y-Z and X-Z symmetry planes as well for an easier visualisation of the local stresses with respect to the pore geometry. In this visualisation mode, ABAQUS calculate stresses in the actual 1/8th model, then mirrors them to the symmetry planes.

Figure 4.5 shows the applied unit load, i.e. green contour, increases roughly by a factor of two, i.e. red contour, due to the pore geometry. Given that the stress concentration factor is defined as the ratio of maximum local stress divided to far-field nominal stress, the legend

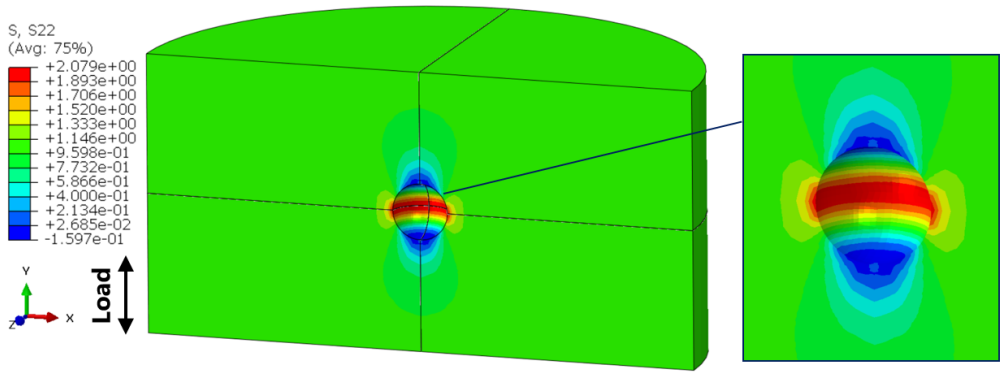

Fig. 4.5 Distribution of local elastic stress component in Y-direction under unit loading

provided in Figure 4.5 can be interpreted as the stress concentration factor as well since a unit load of 1 MPa was applied. Therefore, the stress concentration factor is constant along the circumference of a pore as displayed by the red stress contour in Figure 4.5. This suggests that fatigue cracks can initiate anywhere along the circumference, considering that the location with the highest stress concentration factor is usually associated with crack initiation location. From a practical point of view, surface observations during a routine inspection might be inadequate to eliminate the possibility of cracks initiated from pores, since cracking could start from the embedded portion of a pore as well.

4.2.5 Stress gradient and the influence of pore size

In the finite element model described so far, the pore diameter was systematically increased to demonstrate the influence of pore size on local elastic stress distribution. For this purpose, Figure 4.6 plots the change in maximum elastic stress component (σ_y) along the path that is perpendicular to the applied unit axial loading (1 MPa).

In Figure 4.6, x is the horizontal distance from the pore edge and D is the pore diameter. As expected from the analytical expression, i.e. Equation (4.1), the peak elastic stress is constant and insensitive to pore diameter, which can be seen at x/D=0 in Figure 4.6. However, larger pores cause higher stresses in the surrounding area, for instance at x/D=0.5 peak elastic stress is reduced to around 1.2 MPa for the smallest pore (D) but only to around 1.6 MPa for the largest pore (4D). This feature is characteristic for geometrically similar stress-raisers as pores in this work, and it is commonly used to predict the size effect seen in experimental results of notched test samples; see for instance the Theory of Critical Distances [79]. The interpretation of difference in stress gradients is further discussed in Section 5.2 of Fatigue Design Perspectives. Finally, it can be seen that the increased local elastic stress due to the

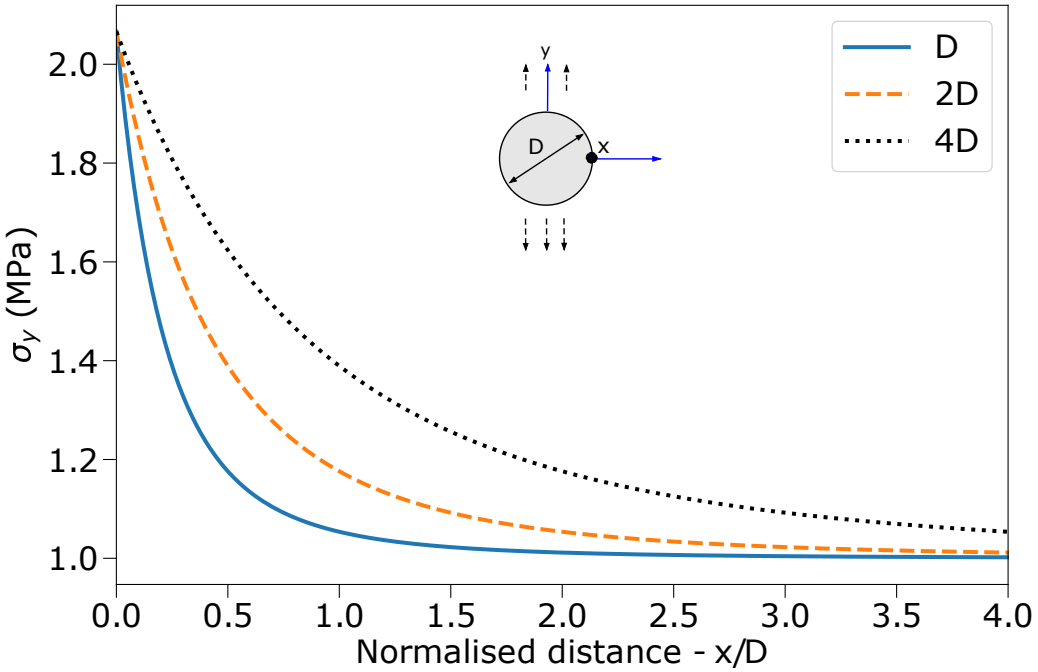

Fig. 4.6 Change in maximum elastic stress component (Y-direction) evaluated at various distances away from the pore edge

pore geometry approximately converges to the far-field applied stress after a diameter away from the pore, i.e. at evaluation points x/D=1, 2, and 4 in Figure 4.6.

4.2.6 The influence of pore location

Surface pores are more detrimental than embedded pores as discussed Section 2.5.3 of the Literature Review. This stems from observations made during high-cycle fatigue testing that the smaller surface pores acted as preferential location for crack initiation despite the presence of much larger embedded pores. In order to investigate this dominance of surface pores, the stress concentration factor of a pore with constant diameter was calculated for various spatial locations as shown in Figure 4.7.

In Figure 4.7, pore spatial location is given as the distance from pore edge to the free surface, which is normalised by the pore diameter, and the stress concentration factor is evaluated at two points, e.g. A and B. Owing to two different evaluation points, the figure has two x-axes corresponding to relevant distances. Furthermore, two additional insets are provided outside the figure on the right hand side to further visualise the problem. Two remarks can be made as follows:

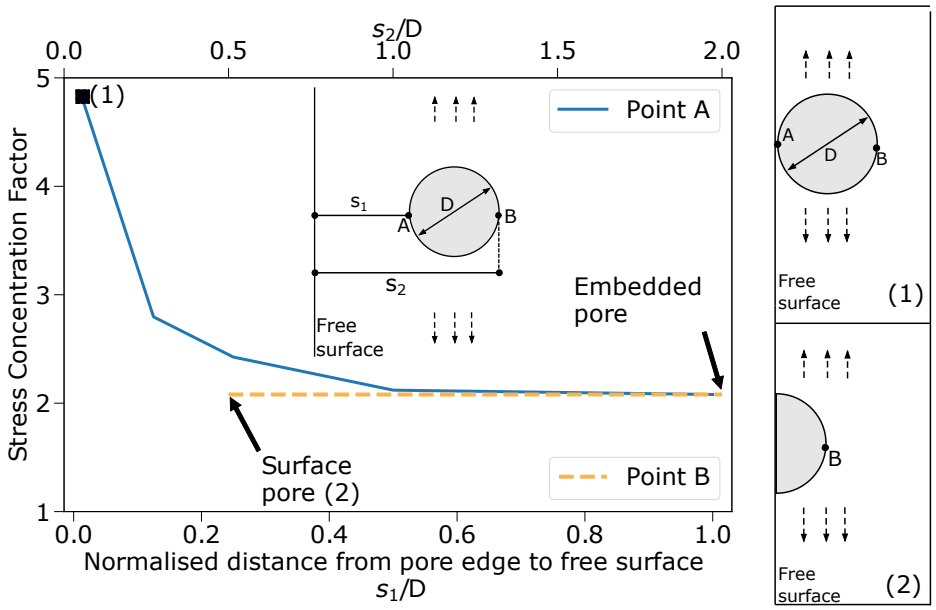

Fig. 4.7 Change in stress concentration factor with respect to pore spatial location for a constant pore diameter. Inset (1) shows the extreme location for point A when there is negligible material remains between the pore and the free surface. Inset (2) visualises the case of a surface pore as seen on fracture faces, e.g. Figure 4.18a, which typically occurs due to post-process machining to achieve desired surface finish.

First, dashed line in Figure 4.7 illustrates the stress concentration factor of a surface pore and an embedded pore is equal. Given that the stress concentration factor is a geometrical parameter, for pores of the same size, the radius of curvature that produces stress concentration is the same for a surface and an embedded pore. Thus, the higher severity of surface pores over embedded pores is unrelated to the stress concentration factor. Instead, this phenomenon might be qualitatively explained by the lower restraint to cyclic slip at the free surface, whereas an embedded pore is surrounded by material that comparatively imposes a larger constraint against the slip motion.

Another highlight from Figure 4.7 is that the stress concentration factor starts to increase on one side of the pore (point A), when the distance between the free surface and the pore is less than a diameter. This is because the increased local stresses due to the pore geometry act on an area roughly a diameter as shown in Figure 4.6, hence the stress concentration factor will increase from its nominal value of 2.08, if less than a diameter material is available to resist. In addition to linear-elastic material model used in this work, more advanced kinematic-hardening material models also suggest a similar behaviour as shown in [150]. As discussed later on in Section 4.4.1, when a pore was less than a diameter away from the free surface, it was assumed as a surface pore in this work despite its spherical morphology. This

is based on the assumption that a fatigue crack will quickly develop due to the high stress concentration factor and break into the free surface, hence forming a surface breaking defect in the process. Furthermore supporting this assumption, in fracture mechanics it is suggested to use almost equal shape factors for surface and subsurface defects [82].

4.3 Material characterisation of L-PBF Ti-6Al-4V

4.3.1 Chemical composition

The results of chemical composition analysis described in Section 3.6 are provided in Table 4.1. The values of the individual elements in this table comply with the specifications given in the industry standard ASTM F2924 [151] for Ti-6Al-4V manufactured using powder-bed fusion techniques.

Table 4.1 Chemical composition of the L-PBF Ti-6Al-4V samples in wt.%

Ti	Al	V	Fe	O	N	H
Bal.	6.11	3.87	0.17	0.15	0.019	<0.001

4.3.2 Microstructure

This section presents the microstructure of a sample that was manufactured using the L-PBF process as part of this work; the procedure for obtaining the microstructure was described in Section 3.5. The aim is to examine whether the manufactured parts were representative of the L-PBF process; the examination was mainly qualitative except the measured α-lath thickness values. Furthermore, fatigue performance of a Ti-6Al-4V alloy depends on the microstructure type, e.g. lamellar versus bi-modal. The micrographs provided in this section can be used to correctly categorise fatigue test data when comparing to literature data.

The microstructure was revealed using two metallographic cuts from the central grip section of flat fatigue dog-bone test sample labelled as 38-3, which was extracted from a rectangular blank shown in Figure 3.2. Microstructure images parallel and transverse to the build direction are shown in Figures 4.8-4.9. For both directions, two sets of images were provided: a macro view for prior β-grain morphology and a magnified view for the α-phase structure. In the magnified views, dark contrast corresponds to β-phase with body centred cubic unit cell structure, while white contrast is the α-phase with hexagonal closed pack structure.

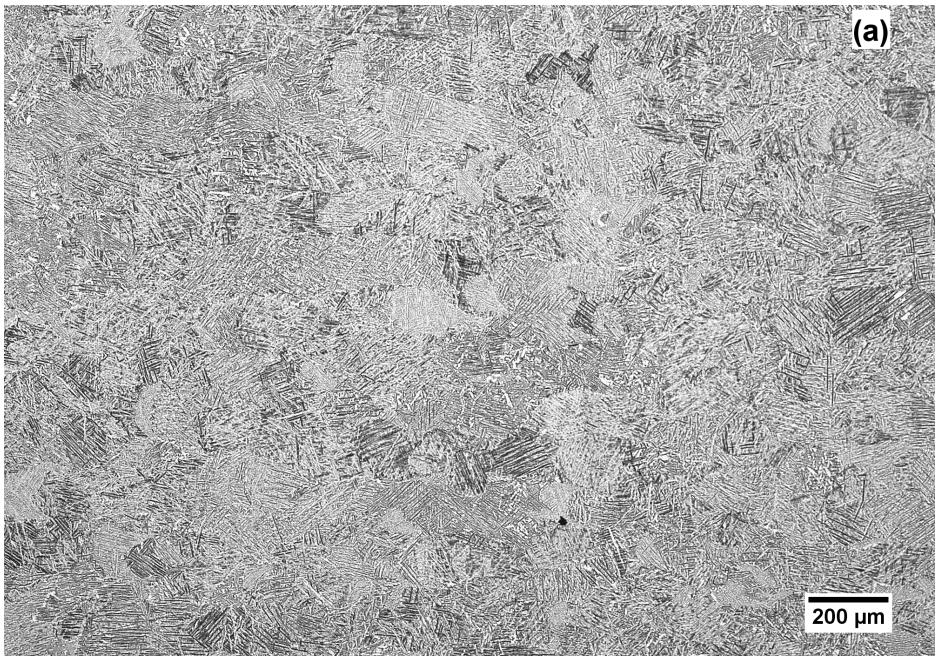

(a) Macro view

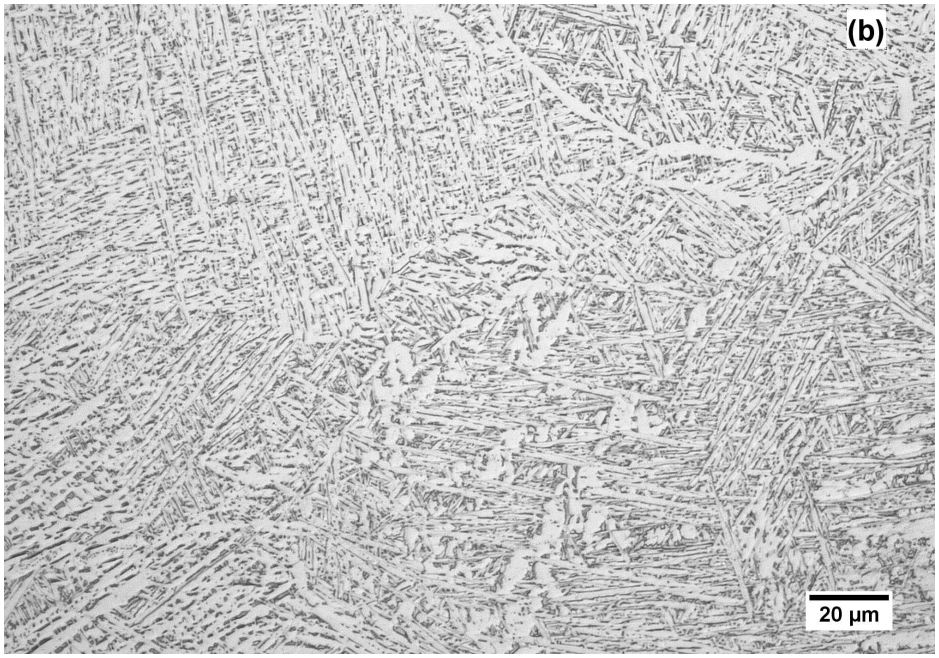

(b) Magnified view

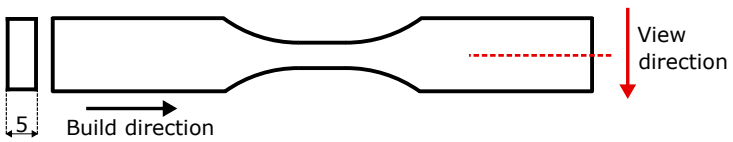

(c) Cut of the metallographic section

Fig. 4.8 Representative images of the microstructure along the build direction for L-PBF Ti-6Al-4V. Images were taken using a light microscope. (a) Macro view (b) Magnified view (c) Position of the metallographic section cut

(a) Macro view

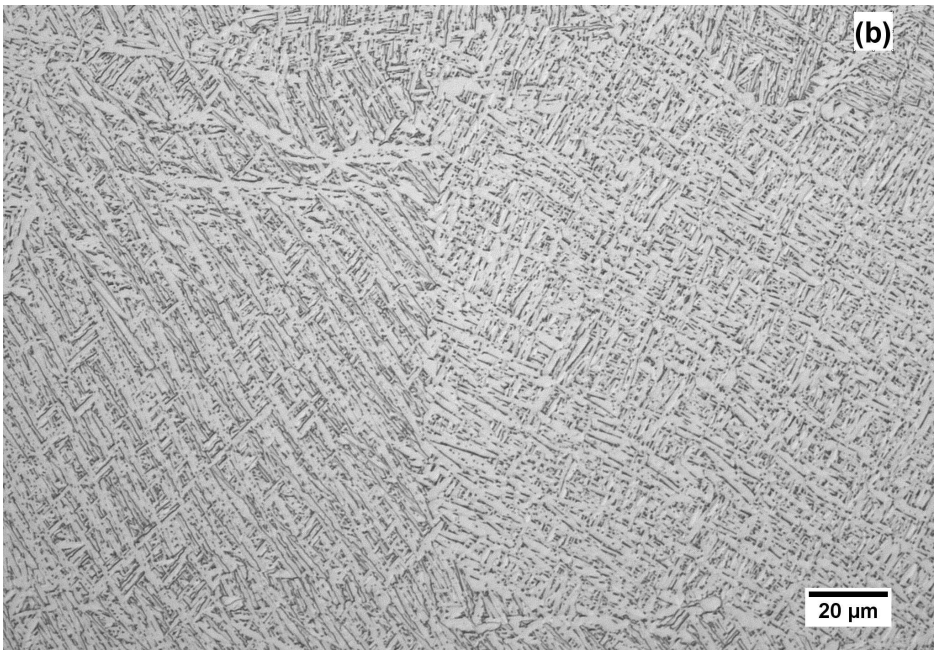

(b) Magnified view

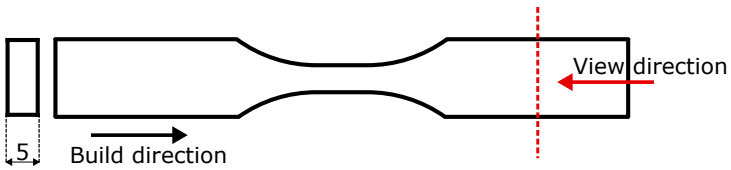

(c) Cut of the metallographic section

Fig. 4.9 Representative images of the microstructure transverse to the build direction L-PBF Ti-6Al-4V. Images were taken using a light microscope. (a) Macro view (b) Magnified view (c) Position of the metallographic section cut

As seen from the macro view along the build direction in Figure 4.8a, columnar prior β-grains were not immediately obvious compared to earlier literature, for instance in [37]. Yet, the prior β-grains along the build direction were still not as equiaxed as in the transverse direction shown in Figure 4.9a. In both close-up images Fig 4.8b and 4.9b, α-laths were intertwined and a colony structure was absent. These sample images of the microstructure are typical for the L-PBF process using standard process parameters, which exhibits a very fine lamellar microstructure, i.e. acicular needles, after the subsequent stress-relief heat treatment as discussed in Section 2.4 of Literature Review. A further distinction can be made depending on the α-phase orientations, which would classify the microstructure as Widmänstatten for single α-phase orientation or Basketweave for multiple orientations, however, this step would require an Electron Backscatter Diffraction (EBSD) analysis that was out-of-scope in this study.

In addition to the type of microstructure, the characteristic length of a specific microstructure type, e.g. α-lath thickness, also plays a role in fatigue performance. For instance as discussed in Section 2.4, finer α-lath thickness in lamellar microstructures leads to superior high cycle fatigue strength [28]. The characteristic microstructural length of an L-PBF sample, i.e. α-lath thickness, was measured using the procedure described in [58] by National Institute of Standards and Technology (NIST). For each direction, i.e. metallographic section, a total of 20 thickness measurements were taken randomly using the magnified optical micrography images given in Figures 4.8b-4.9b. This measurement was conducted three times to assess repeatability and the measured mean values and standard deviations are given in Table 4.2.

Table 4.2 α-lath thickness measurements of L-PBF Ti-6Al-4V

Build direction	Measurement no.1 (μm)	Measurement no.2 (μm)	Measurement no.3 (μm)
Parallel	1.64 $\pm$0.50	1.50 $\pm$0.57	1.45 $\pm$0.56
Transverse	1.42 $\pm$0.46	1.64 $\pm$0.55	1.41 $\pm$0.50

The α-lath thickness measurements shown in Table 4.2 correspond well with the literature data, which were obtained using the more detailed intercept method as discussed in Section 2.4. It is important to note that α-lath thickness measurements were taken from one section in a sample, hence they are extremely limited. In additive manufacturing, microstructural heterogeneity can be a concern [152], i.e. there might be a local variation in α-lath thickness due to uneven thermal history; for instance Sharma et al. [153] shows the influence of build height on α-lath thickness. This possible local variation of microstructure was not further investigated in this work, since the experimental programme was designed to concentrate

on the influence of porosity on fatigue, hence a single batch manufacturing and post-heat treatment were carried out to avoid any significant microstructural variation among the test samples. Furthermore, the minimum crack initiating pore size was 40 μm, which is considerably larger than the α-lath thickness, hence the fatigue life would be expected to be dominated by pore size rather than any variation in α-lath thickness.

4.3.3 Porosity characterisation

Pore size distribution

Using the scanning parameters given in Section 3.7, pores within the gauge volume of near-net shape manufactured dog-bone samples were characterised prior to fatigue testing. A representative measurement from a sample is given in Figure 4.10, which shows a histogram of pore size distribution along with crack initiating pore diameter as measured on the fracture surface. The pore diameter in Figure 4.10 was calculated using Equation 4.2.

$$d = 2\sqrt{\frac{\text{Area}}{\pi}} \tag{4.2}$$

where *Area* either calculated by summing number of pixels detected during image segmentation stage of X-ray Computed Tomography measurements as per Section 3.7 or by fitting a spline along the crack-initiating pore as seen on the fracture surface to establish boundaries, and then area inside this boundary was calculated by using the open-source image analysis software ImageJ [124], which counts the number of pixels to quantify this value.

The histogram in Figure 4.10 reveals a positive skewed distribution of pore diameters, i.e. majority of the detected pores were below the mean pore diameter. This shape was expected based on the available literature studies not only from additive manufacturing [155] but also from inclusions in conventional manufacturing [134]. Positive skewed size distribution was consistent among the scanned samples in this work; therefore, the remaining samples were given in Appendix D for clarity.

For the sample shown in Figure 4.10, despite a total of 189 detected pores, bulk density of the gauge volume was calculated as 99.98%. Yet, fatigue being a local phenomenon, one large pore above the critical pore size is enough to initiate cracking and lead to a premature failure. In this particular case, a large pore but not the largest was detected as the crack initiating pore during fracture surface study and marked in Figure 4.10 as well. In practice, by fitting a curve to the extreme tail of a known defect size distribution as in Figure 4.10, the maximum defect size can be estimated for a component where defect measurements are

Fig. 4.10 Representative histogram of a pore size distribution detected in the gauge volume of a fatigue dog-bone sample manufactured using L-PBF (Sample ID = NNS no.8). The size distribution was obtained using X-ray Computed Tomography along with crack initiating pore diameter as measured on the fracture surface. As appeared in [154]

.

unavailable; example of such work can be found in [8, 134, 156]. Afterwards the estimated defect size can be used to predict fatigue life either using the threshold framework or crack propagation framework as discussed in Section 2.6-State-of-the-art.

Intersample variability

Although test samples were manufactured in a single batch, process conditions could still vary locally due to differences in test sample location on the build plate, which could lead to different defect population in each sample. In this regard, shape of the histogram for pore size distribution was consistent among the scanned test samples as mentioned previously. Furthermore in Table 4.3, pore size statistics of each scanned sample is provided.

Table 4.3 shows that mean pore diameter and its standard deviation among the scanned samples was remarkably consistent. Given that the shape of size distribution was also consistent, it can be qualitatively stated that pore size population was unaffected by the sample location on build plate. This finding, however, cannot be generalised since this would

Table 4.3 Pore size statistics among the scanned test samples

	NNS Sample ID								
Parameter	#2	#3	#4	#5	#6	#7	#8	#10	#12
Maximum dia. (μm)	101.18	86.59	79.81	84.24	88.74	82.51	82.09	81.28	82.14
Mean dia. (μm)	43.01	42.32	42.49	42.87	41.21	42.52	37.08	40.24	37.99
Standard deviation	13.29	12.80	11.86	11.74	11.73	11.91	10.30	11.47	10.91
No. of pores detected	172	203	250	281	228	260	189	203	219

require a quantitative analysis using statistical techniques like ANOVA, and also exploring more extreme locations on the build plate rather than clustering all specimens in one corner as in this work (Figure 3.1).

In general, pore size statistics shown in Table 4.3 is challenging to compare with literature data as defects depend on build part size and shape. For instance, albeit for electron beam melting process, Tammas et al. [95] reported 81.7 μm mean pore diameter, which is roughly double the value of pores detected in this work but it was for a 1600 mm^3 volume, which is roughly 8 times larger than the volume scanned in this study. Similarly, Cunningham et al. [22] reported 6.21 μm mean pore diameter, but for a tiny volume of 1.5 mm^3.

In terms of fatigue, which is the main scope of this work, extreme values are usually the main point of interest, i.e. fatigue failure typically correlates with the extreme tail of a size distribution rather than the mean values. In this regard, maximum detected pore diameter shows a larger variance compared to mean pore diameter as shown in Table 4.3. However, this variance did not turn into a significant fatigue life scatter as discussed later on in Section 4.4.1, and the pore spatial location rather than its size was found to be the main contributor to the fatigue life scatter. Spatial distribution of pores as measured using X-ray Computed Tomography is discussed next.

Spatial distribution of pores

In general, surface defects or cracks are more detrimental than their embedded counterparts, which is captured by the shape factors in stress intensity factor equations. Therefore, a pristine surface, and also sub-surface, is desirable against fatigue. Understanding the spatial distribution of pores could provide insight about their severity and also could help deciding a suitable post-manufacturing treatment; for instance the popular hot isostatic pressing is

ineffective against defects connected to free surface [157]. In this regard, Figure 4.11 shows all pores detected within a gauge volume projected into a

Fig. 4.11 A representative spatial distribution of porosity for L-PBF Ti-6Al-4V. In this image all the detected pores within a gauge volume using μXCT were projected on a cross-sectional plane. As appeared in [154].

Spatial distribution of pores showed a clear tendency towards the free surface as seen in Figure 4.11; around 85–90% of pores were located within 200 μm beneath the surface as marked with a blue circle. In contrast, early literature suggested that pores were distributed randomly [54, 158], based on the understanding that gas pores are formed when they are unable to escape the melt pool. Considering that the melt pool geometry can be influenced by the selected process parameters, the latest evidence suggests that there is a strong correlation between the manufacturing strategy and location of the pores: Tammas-Williams et al. [146] related pore locations with the movement patterns of the energy source, i.e. scanning strategy, in powder-bed fusion AM, albeit for a process that uses a different energy source instead of a laser. Similar spatial distributions can be seen in literature [159], though not emphasized as in here, or produced based on metallography [160], hence not as distinct as in Figure 4.11. Some preliminary work [161] also further corroborates the tendency of pores being located towards the free surface.

The majority of the L-PBF samples were failed from surface porosity, because spatial distribution of pores showed a tendency towards the free surface. When the defect dense

layer beneath the surface was removed, the samples still failed due to surface porosity since during additional material removal some of the embedded pores were exposed to the surface. There is on-going research concentrating on machining strategies, i.e. deep versus shallow machining as a post-processing option [162, 163]. Theoretically, by using a suitable machining strategy, embedded pores acting as the crack initiation source is also possible, but this was not the case for L-PBF Ti-6Al-4V in this work.

Finally, measured pores as described so far were categorised as surface and embedded pores, then size statistics for each category was quantified. A representative sample is shown in Figure 4.12, and the rest of the measurements can be found in Appendix D.

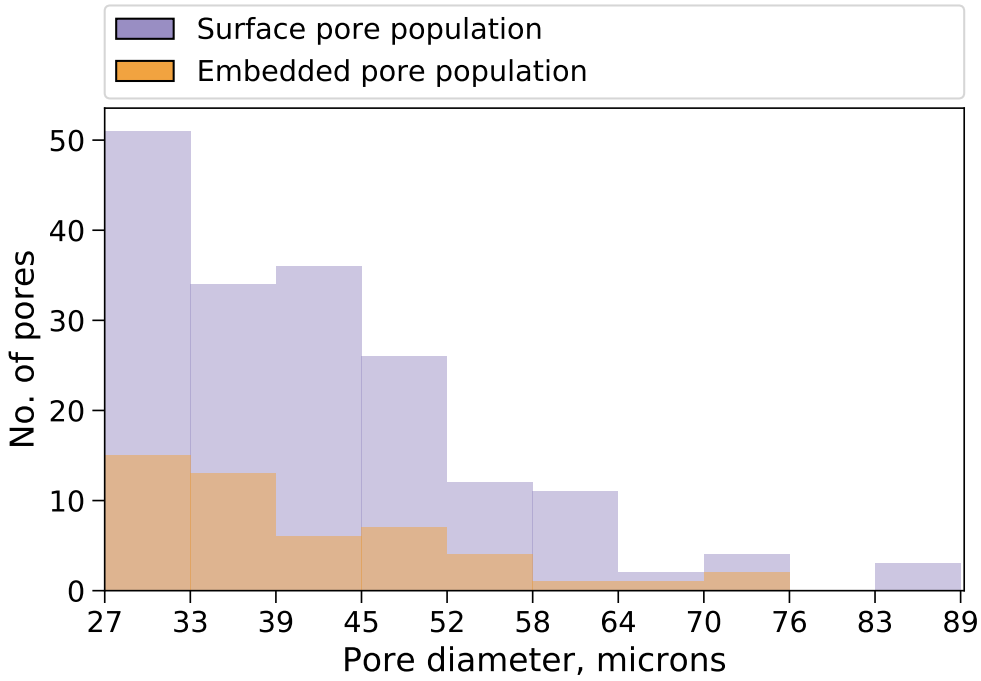

Fig. 4.12 Representative histogram of pore size distribution of embedded and surface porosity. (Sample ID = NNS no. 6)

.

Figure 4.12 shows that the shape of size distribution of embedded and surface pores were similar, and the main difference was the number of detected pores as can expected by looking at Figure 4.11. Thus, the mean pore diameter was found to be comparable for both populations, e.g. 41.77±12.14 μm for surface pores and 40.25±11.64 μm for embedded pores. This trend was observable in the remaining scanned samples shown in Appendix D. Therefore, it can be concluded that there was no significant difference in size between embedded and surface pore populations.

Distribution of pores along the height of gauge section

The gauge length of the scanned samples were 10 mm, and for each sample a histogram was created by binning 1 mm sections along the gauge length. A representative sample is shown in Figure 4.13, and the rest of the measurements can be found in Appendix D.

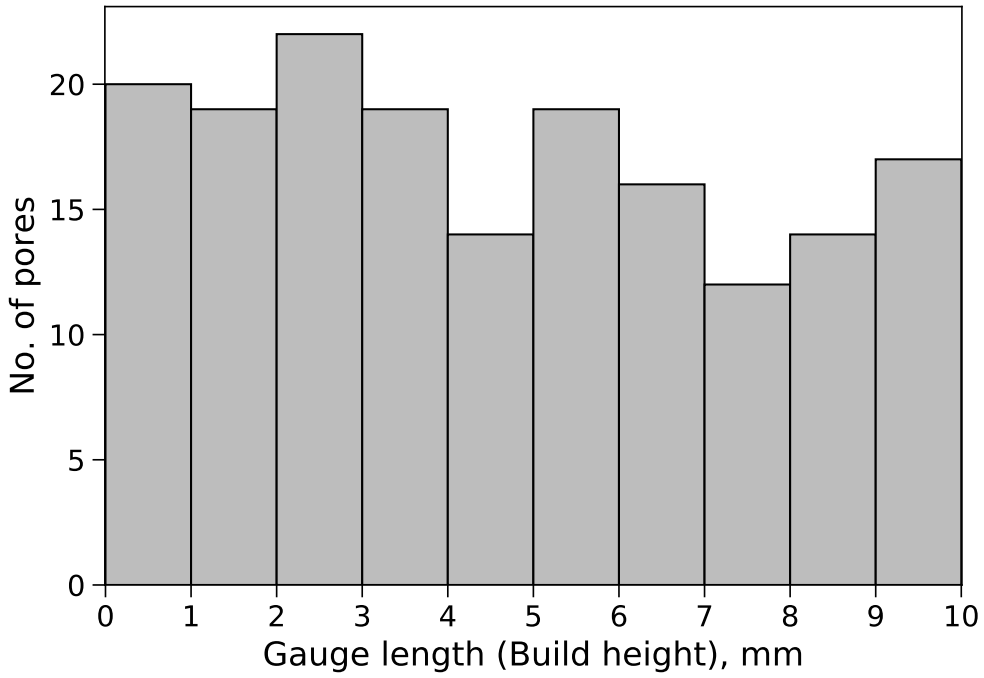

Fig. 4.13 Representative histogram of detected pores along the height of gauge section. (Sample ID = NNS no. 2)

.

Figure 4.13 shows the number of pores detected within each 1 mm section along the gauge length; please note that considering the vertical build orientation, 0-1 histogram bin is closest to the build plate and 9-10 histogram bin is farthest to the build plate. A relatively uniform shape can be observed from Figure 4.13, hence no significant influence of build height on pore distribution can be stated. However, it should be noted that a limited volume was scanned in this work, e.g. grip sections of the test sample were not scanned. In literature, albeit for electron beam melting process, Seifi et al. [152] for 100 mm tall sample and Elambasseril et al. [145] for 300 mm tall sample have shown that defect density is higher closer to the build plate compared to the very top in a vertical build orientation.

Pore coalescence

Given that majority of pores were located right beneath the surface, the likelihood of a pore coalescence is higher due to the increased defect density in a confined volume. In fact, 3-D visualisation of coalesced pores can be found in literature and shown in Figure 4.14.

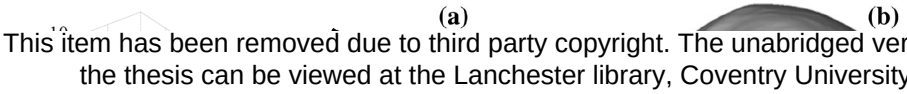

Fig. 4.14 3D visualisation of coalesced pores (marked by black arrows). Image on the left originally from [146] and reprinted by permission from Creative Commons CC-BY license. Image on the right originally from [126] and reprinted by permission from Springer Nature.

On fatigue fracture surfaces of L-PBF Ti-6Al-4V, it is possible to observe an irregular defect morphology as the crack initiation source; examples can be found in Figures 4.15a and 4.18b. An irregular defect morphology is unexpected, because pores are approximately spherical. The other common defect type in AM, the so-called lack of fusion defects are indeed irregular, however, they often manifest with un-melted powder particles and a rough interior surface, which is not the case in Figures 4.15a and 4.18b. Consequently, such observations are mentioned as "facet" [56] or "irregular pore" [100] in the literature. In order to clarify the crack initiation source, successive projections from a single μXCT scan are given in Figure 4.15(b-c).

In Figure 4.15(b-c), it is possible to see two individual pores are combining, leading to an irregular shape that resembles the one seen in the fracture surface in 4.15a. From a structural integrity perspective, coalesced pores will have a higher stress concentration factor (K_t) compared to a spherical pore due to their irregular morphology, thus test specimens with coalesced pores or defects with irregular morphology as crack initiation source could have an inferior fatigue life compared to cases with a spherical pore as crack initiation source. However, such a difference was not observed as part of the fatigue tests that were carried out in this study as shown in Table 4.4, which consists of fatigue data from same applied maximum stress and nominally similar surface quality, but involves additional variability due

Fig. 4.15 (a) Fatigue fracture surface showing an irregular defect as the crack initiation source; the image was obtained using SEM under secondary electron mode. (b, c) Sequential μXCT slices of another specimen showing pore coalescence that is similar to the fracture surface observation in (a). As appeared in [154].

to manufacturing source and test geometry. This unexpected outcome is further discussed in Section 4.4.1 and more data is needed to further support this evidence.

Table 4.4 The influence of crack initiating defect morphology on fatigue life at 600 MPa applied maximum stress

ID	Source	Test geometry	Fatigue life (cycles)	$\sqrt{area}$ (μm)	Defect shape
15-1	Rectangular blank	Flat dog-bone	102,672	42.45	irregular
38-1	Rectangular blank	Flat dog-bone	104,712	55.81	irregular
38-3	Rectangular blank	Flat dog-bone	91,446	42.40	irregular
NNS-6	Near-net manuf.	Cylindrical	48,835	84.50	irregular
		Average	86,916	56.29	irregular
19-T	Rectangular blank	Flat dog-bone	71,033	57.80	circular
38-2	Rectangular blank	Flat dog-bone	101,562	44.87	circular
NNS-8	Near-net manuf.	Cylindrical	53,624	68.78	circular
		Average	75,406	57.15	circular

4.4 Mechanical testing

4.4.1 High cycle fatigue

Figure 4.16 shows the fatigue testing results in an S-N diagram, which were obtained by following the procedure outlined in Section 3.9. In Appendix A, the results are also provided

in a tabulated form; this table includes additional information such as the specimen type, crack initiation source, and more. Data points in Figure 4.16 and Appendix A correspond to the fatigue test results that were carried-out at TWI Ltd as part of this PhD. However, for completeness, previous fatigue test results from the same WAAM process batch were also included in Figure 4.16a, which were carried-out at Coventry University as part of a previous PhD work [15]. Thus, WAAM samples include an additional scatter source due to the change in fatigue testing machine.

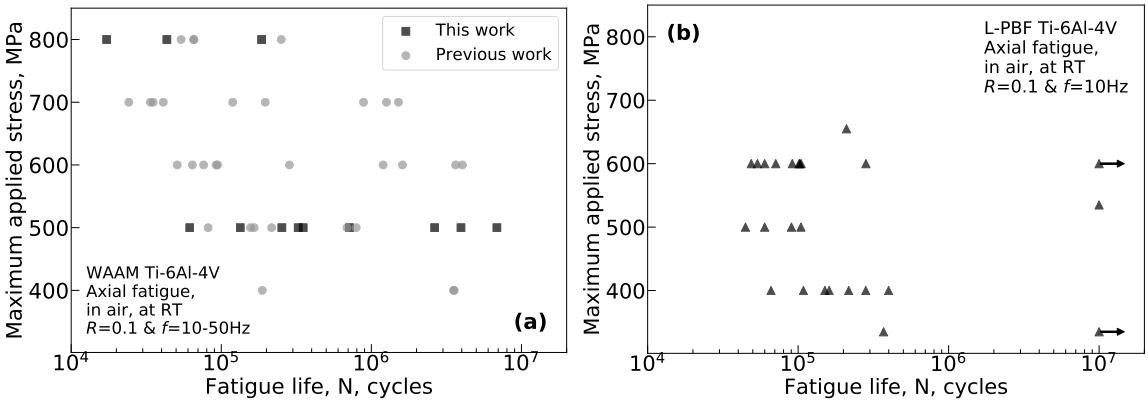

Fig. 4.16 High cycle fatigue test results (a) Wire+arc additive manufacturing (WAAM) including results from a previous work [15] (b) Laser powder-bed fusion (L-PBF)

A significant scatter of fatigue life can be observed in Figure 4.16; for instance there is three orders of magnitude difference in fatigue life at the maximum applied stress level of 500 MPa for the WAAM process. The scatter of fatigue life is common in AM of metals, for instance similar plots can be seen in [40, 164, 165], and the scatter is often associated with manufacturing defects [53, 54, 49]. Therefore, a fracture surface analysis was conducted for each sample in Figure 4.16 to examine crack initiation sources.

Five different crack initiation sources were determined from the fracture surface analysis of samples built by the WAAM process, however, majority of the samples were failed either from surface pores or embedded pores. On the other hand, four different crack initiation sources were observed in the L-PBF batch, yet majority of the samples failed from surface pores. Representative images from the fracture surface analysis are provided in Figures 4.17 and 4.18.

A surface pore can be distinguished from its semi-elliptical morphology on the fracture surface as seen in Figures 4.17a and 4.18a. Surface pores can be classified as “semi-natural” defects considering that all pores are embedded in the as-built condition. The embedded pores are exposed to the surface after an additional material removal during the post-processing

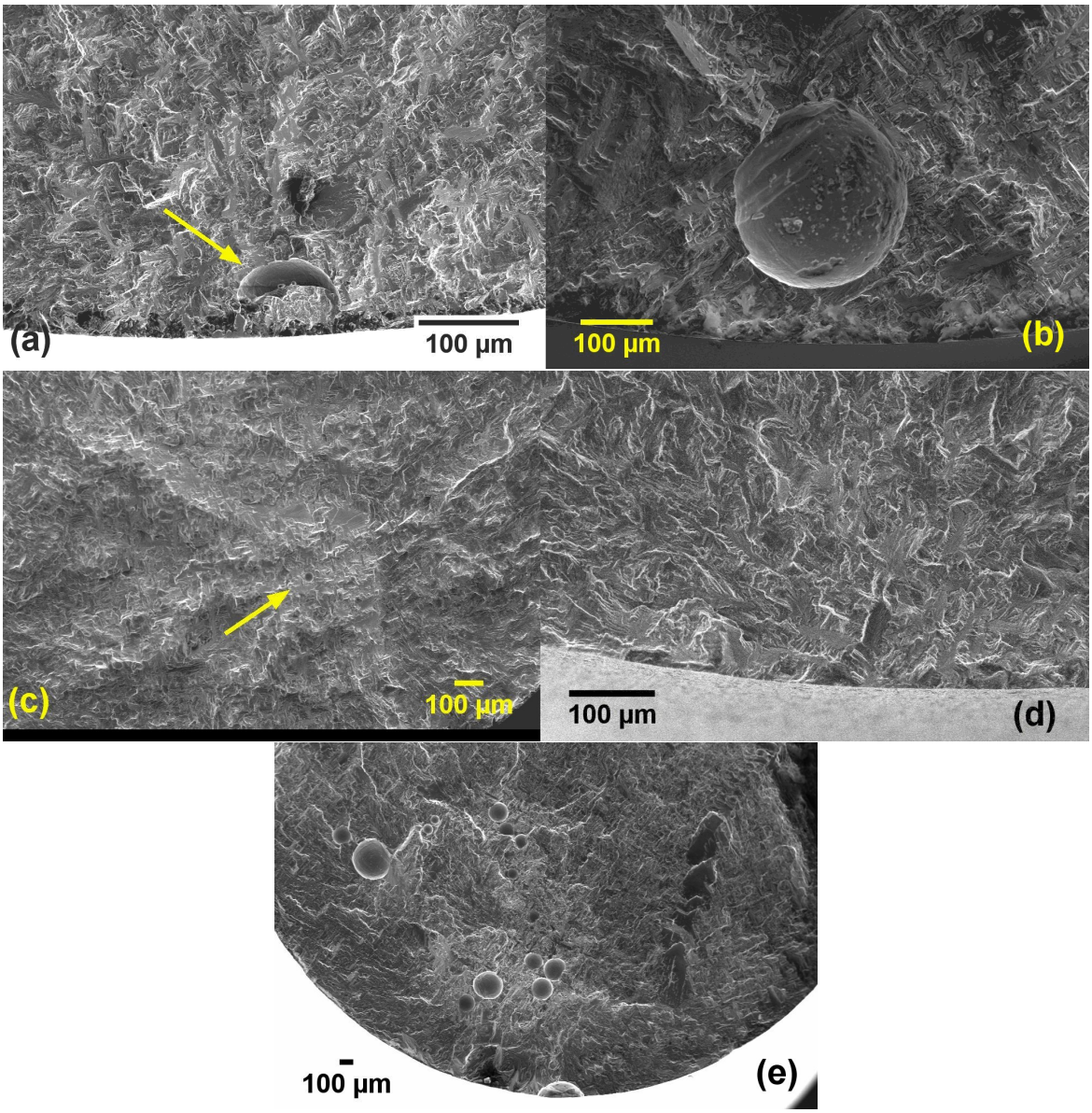

Fig. 4.17 Fatigue crack initiation sources seen in WAAM samples. Images were obtained using scanning electron microscopy. (a) Surface porosity (b) Sub-surface pore (c) Embedded pore (d) Microstructure (e) Clustured pores

stage, which is often necessary to achieve a desirable surface finish for cyclic loading applications. Thus, the surface pores in AM are a relatively common defect type and they can be observed in many other works in the literature as well.

The morphology of surface pores can deviate from the semi-elliptical shape seen on the fracture surface, an example is given in Figure 4.18b. Surface pores with irregular morphology were seen exclusively in L-PBF samples and their origin could be related to

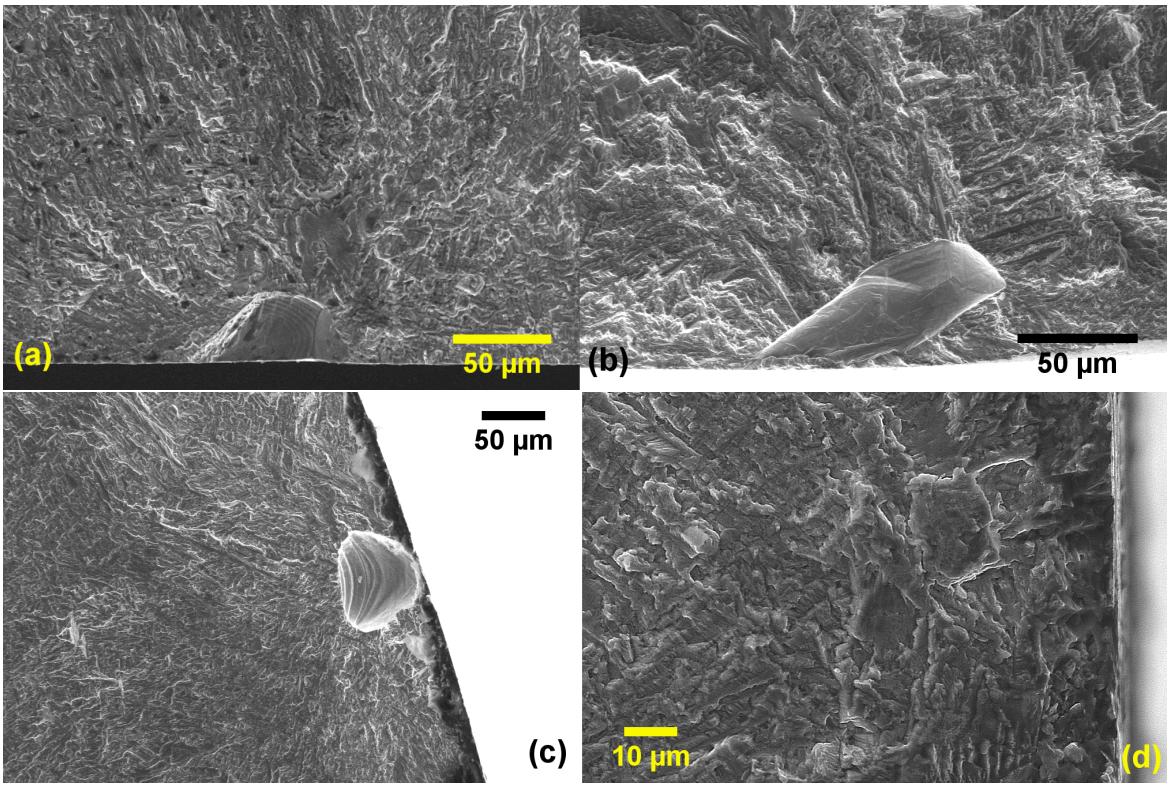

Fig. 4.18 Fatigue crack initiation sources seen in L-PBF samples. Images were obtained using scanning electron microscopy. (a) Surface porosity (b) Irregular pore (c) Sub-surface pore (d) Microstructure

coalescence of pores as discussed in Section 4.3.3 or the keyhole mechanism of lasers, which is absent in plasma sintering of WAAM. Compared to a semi-elliptical surface pore, the stress concentration factor of an irregular surface pore will be higher due to its complex morphology, however, a difference in fatigue life was not observed in this study as shown in Table 4.4. This observation based on limited data suggests that fatigue life might be dominated by the crack propagation regime, but later in the replica study in Section 4.4.3, the crack initiation life was found significant. Similarly, Leopold et al. [166] reported a negligible influence of defect morphology and a significant crack initiation life for the same titanium alloy, albeit made from cast, hence much coarser, colony type microstructure. Thus, although the observed behaviour seem to be present across different microstructures, the available fatigue test data is limited and more research is needed to better understand the influence of defect morphology on fatigue life of titanium alloy Ti-6Al-4V.

The next distinct crack initiation source is the so-called “sub-surface” pore as seen in Figures 4.17b and 4.18c, which can be distinguished by the circular morphology, i.e. the pore is entirely embedded within the material. From the finite element analysis results using

kinematic hardening material model presented in [150], it can be inferred that embedded pores should be classified as "surface pores" when the distance between the free-surface and the pore is less than its diameter. When this criteria was fulfilled, sub-surface pores were treated as surface pores in the remainder of this work, assuming that a crack will quickly develop between the free surface and the sub-surface pore as a result of the increased stress concentration factor (Figure 4.7). This crack will then subsequently break the surface, forming a surface pore. Thus, it was expected that sub-surface pores act as surface pores for the majority of the fatigue life. Similar arguments can be found in the literature [167] and also captured by shape factors of stress intensity factor calculations in [82].

The fourth distinct crack initiation source is "embedded defects" that are more than one diameter away from the free surface and have a circular morphology on the fracture surface, see Figure 4.17c. Embedded pores are expected to be less detrimental to fatigue performance compared to surface pores due to: (1) lower crack driving force for the same crack length, (2) crack tip subject more favourable environmental conditions. The first point can be demonstrated by comparing an embedded penny shaped crack in an infinite medium to an edge crack in a semi-infinite body for simplicity, noting that a more appropriate comparison would be using finite body solutions discussed later in Chapter 5. Crack driving force equations for both cases can be found in handbook of stress intensity factor solutions, e.g. [168], and given in Equation (4.3) for the former and in Equation (4.4) for the latter.

$$\Delta K = (\frac{2}{\pi})\Delta S\sqrt{\pi a} \approx 0.64\Delta S\sqrt{\pi a} \tag{4.3}$$

$$\Delta K = 1.12\Delta S\sqrt{\pi a} \tag{4.4}$$

where ΔK is the crack driving force, ΔS the applied far-field stress range, a the crack depth or radius. It can be seen that for equal crack dimensions, the crack driving force ΔK, will be lower for an embedded defect. Furthermore, crack propagation rate is sensitive to the environmental conditions. For instance, fatigue crack growth rate was found to be slower in vacuum, which would be relevant to embedded cracks, compared to fatigue cracks propagating in air for conventional manufactured Ti-6Al-4V [169, 170, 171]. Therefore, embedded defects are expected to be less detrimental than surface defects due to the combination of lower crack driving force and more favourable environmental conditions.

As shown in Figure 4.17e, pores clustered together were also seen as a crack initiation source in intentionally contaminated WAAM samples. This scenario was considered out-of-scope for this work and was not pursued further. It is worth emphasizing that clustered pores as the crack initiation source was only present in the samples fabricated from a contaminated

wire, which suggests that it could be avoided by following the best-practice measures during manufacturing. Similarly, industrial standards such as ASTM F3187, Clause 8.2.2.4 put measures on quality of the feedstock material, hence this failure source might not have any practical relevance. Finally, it should be noted that, some of the samples were failed either from remaining surface roughness or scratches as labelled in Appendix A. These were considered as user-errors and removed from the analysis in the following plots.

4.4.2 Scatter of fatigue life

Categorising S-N data of WAAM Ti-6Al-4V

Fracture surface analysis did show a variety of crack initiation sources, which could explain the significant scatter observed in the S-N diagram shown in Figure 4.16a. Here, it is argued that the scatter seen in Figure 4.16a is normal, since samples fail from different sources. This statement is further demonstrated by using a normal probability plot in the following.

The procedure given in BS ISO 12107 [172] was followed to produce a normal probability plot: first fatigue test results were sorted in the ascending order, e.g. from lowest life to the highest fatigue life obtained at the applied load level. Then individual probabilities were calculated using Equation (4.5).

$$P_i = \frac{i - 0.3}{n + 0.4} \tag{4.5}$$

where P_i is the probability of failure of i^{th} sample, n the total number of samples at that applied load level. For demonstration, fatigue data of WAAM samples were used at 500 MPa and 600 MPa maximum applied stress levels; in the former samples were mainly failed due to large surface pores, whereas in the latter a mixture of failure sources and crack initiating pore dimensions were present. The calculated normal probability plot is shown in Figure 4.19.

As seen in Figure 4.19, the scatter of fatigue life is around an order of magnitude at 500 MPa applied maximum stress level, whereas it is more than two orders of magnitude for 600 MPa. Furthermore, a linear line can be drawn at 500 MPa maximum applied stress level; a linear line is expected based on the common assumption that logarithm of fatigue lives being normally distributed. However, at 600 MPa applied maximum stress level two distinct groups of fatigue data is visible, suggesting entirely different failure sources, e.g. from a surface pore and an embedded pore.

Based on the evidence from fracture surface analysis and normal probability plot, WAAM Ti-6Al-4V fatigue test data was categorised according to the failure source. After categori-

Fig. 4.19 The influence of porosity on fatigue life of WAAM samples shown in normal probability plot. Plot legend with respect to maximum applied stress values. As appeared in [173].

sation of failure sources, it was possible to fit a linear S-N curve in the log-log plot with a high correlation coefficient, e.g. R^2 around 0.9. Coefficients of the linear regression analysis are provided in Table 4.5, which correspond to the Basquin equation (power law) that was modified by Morrow [174] to accommodate the mean stress influence, Equation (4.6).

Table 4.5 Linear regression results of the S-N curves

	Surface pore failure	Embedded pore failure
σ'_f-σ_m	1305	2597
b	-0.131	-0.145
No. of data points	14	7
Correlation coefficient (R^2)	0.896	0.897

$$\sigma_a = \left(\sigma'_f - \sigma_m\right)\left(2N_f\right)^b \tag{4.6}$$

$$\begin{aligned} \log\sigma_a &= b\log\left(2N_f\right) + \log\left(\sigma'_f - \sigma_m\right) \\ \sigma_a &= 1305\left(2N_f\right)^{-0.131} \end{aligned} \tag{4.7}$$

where σ_a the applied stress amplitude, σ'_f the cyclic fracture strength, σ_m the applied mean stress and b the Basquin coefficient. As an example, Equation (4.6) is expanded to show equation for the S-N curve of samples failed from surface porosity in Table 4.5.

Fig. 4.20 S-N curves according to the crack initiating defect type for WAAM Ti-6Al-4V. As appeared in [173] with additional fatigue data from subsequent testing.

S-N curves calculated using linear regression analysis are plotted in Figure 4.20. This figure suggests that the significant scatter of fatigue life, which was shown in Figure 4.16a, is mainly related to the defect type, more specifically defect location. Defect size in the surface porosity group ranged from approximately a minimum of 100 microns in diameter to a maximum of 400 microns in diameter, and the average crack initiating surface pore size was 175.5 microns. On the other hand, defect size in the embedded porosity group ranged from approximately a minimum of 20 microns in diameter to a maximum of 60 microns in diameter, and the average crack initiating embedded pore size was 32.7 microns. As previously discussed in the Experimental Programme, some of the samples were manufactured using contaminated wires, which enabled to investigate a large range of crack initiating pore diameters as evident from the preceding statistics.

From a fatigue design perspective, individual S-N curves according to defect type can be calculated using linear regression, which can be subsequently used in practice with appropriate confidence intervals and safety factors. A similar situation exists in the welding design recommendations, e.g. Hobbacher [175], where according to the weld type or joint configuration, a specific S-N curve exists, the so-called FAT classes. Such a scenario could be suitable for the AM materials, since early literature in AM fatigue has established that there is

no competition among the failure sources but rather a clear hierarchy exists [40, 176]: Surface roughness in the as-built condition is the most detrimental situation. After eliminating it, process-induced defects, such as porosity, act as main sources of fatigue failure. Finally, if a thermo-mechanical treatment such as hot isostatic pressing (HIP) is applied, fatigue performance can reach to the wrought material level and fatigue cracking initiates from microstructural features. Therefore, for engineering design, a specific S-N curve can be selected depending on the expected failure source (defect type), which can be predicted depending on the post-processing history. The further nuance about the critical defect size is discussed later in Section 5.2.

Fatigue life reduction in L-PBF Ti-6Al-4V and comparison of scatter with conventional manufacturing

After demonstrating the major influence of pore location on fatigue life, this Section is dedicated to the influence of pore size on fatigue life by considering the same defect types only; more specifically, surface pores since majority of the fatigue data corresponds to this defect type. Again, normal probability plots were used to demonstrate fatigue life variability by using the procedure given in BS ISO 12107 [172]. The standard recommends using at least seven data points, hence L-PBF test series were suitable in which fatigue tests were repeated at selected load level and surface pores were the dominant failure source. For comparison, fatigue test results from a forged Ti-6Al-4V were extracted from [177] and shown in Figure 4.21 as well. For L-PBF Ti-6Al-4V fatigue life variability was assumed to be related to the change in crack initiating pore diameter, whereas for the forged Ti-6Al-4V fatigue life variability was associated with distribution of unfavourably oriented surface grains.

From Figure 4.21, it can be seen that defects reduce fatigue life on average, e.g. 50% of probability, by a factor of 27.8 at 600 MPa applied stress level. However, fatigue life variability, which is up to three orders of magnitude in forged Ti-6Al-4V, was reduced significantly for the case of L-PBF Ti-6Al-4V, e.g. between 50,000 cycles and 100,000 cycles. This suggests that defects act as preferential location for crack initiation hence reducing scatter despite the fact that crack initiating pore diameter was changed by a factor of two, e.g. from 40 μm to 80 μm. On average, crack initiating surface pore diameter was 56 μm in L-PBF Ti-6Al-4V, which is comparable to crack initiating pore dimensions given in Appendix A for WAAM Ti-6Al-4V when a clean wire is used, whereas considerably less when a contaminated wire is used in the WAAM technique.

Fig. 4.21 Influence of surface pore size on fatigue life scatter of L-PBF Ti-6Al-4V, including a comparison with conventionally manufactured counterpart. Originally published by the author in [154]

4.4.3 Fatigue crack growth measurements of L-PBF Ti-6Al-4V

The replicating procedure coupled with the fatigue testing was outlined in Section 3.10. Following the procedure, three useful measurements were obtained and these are plotted in Figure 4.22. The crack length measurements in Figure 4.22 also include pore width as seen on the test specimen surface.

At $\Delta\sigma$=540 MPa applied stress range, somewhat fortunately, a crack initiating pore located close to the sample edge was observed as shown in Figure 4.23a. Under normal circumstances, replica measurements are limited to crack length observations; however, owing to this coincidence the crack depth measurements were also obtained. Furthermore, the fatigue cracks initiated from pores formed a semi-elliptical shape as shown in Figure 4.23b, which is a common observation in fatigue. The measurement results from $\Delta\sigma$=540 MPa applied stress range were used in Figure 4.24 to further describe replica test findings.

The particular sample seen in Figures 4.23a-4.24 failed at 71,033 cycles using an applied stress range of $\Delta\sigma$=540 MPa; the crack initiation source was a surface pore with an equivalent diameter of 65 μm as shown in Figure 4.23a. At first replicating cycle, e.g. 20,000 cycles, there was not any observable cracking, noting that this technique is shown to capture cracks as small as 10 μm [178]. First fatigue cracking was detected at 40,000 cycles as shown in 4.24a. At this stage, the crack was still in the "microstructurally small" regime distinguished by the zig-zag path; hence it could be argued that the crack might not yet evolved into a semi-elliptical shape. At 60,000 cycles, the crack was growing perpendicular to the applied

Fig. 4.22 Crack length measurements plotted against replicating intervals obtained from three different fatigue tests. Crack length includes the pore width as seen on the sample surface. Hollow markers indicate crack depth measurements. First published in [154].

Fig. 4.23 (a) Fracture surface of one sample used in the replica study at $\Delta\sigma$=540 MPa, obtained using scanning electron microscopy in secondary electron mode at 20 kV. Surface pore was identified as a crack-initiating source. (b) Macro-photo of the fracture surface shows a clear semi-elliptical crack shape that is evolved from process-induced porosity. First appeared in [154].

load direction as shown in Figure 4.24b, which corresponds to the stage II in fatigue crack growth regime under the mode-I loading. At this stage, the crack was assumed to be advanced enough to develop into a semi-elliptical shape.

Fig. 4.24 Surface replica results of a sample tested at $\Delta\sigma$=540 MPa and failed at 71,033 cycles (a) First crack detection at 40,000 cycles located along the width of the fatigue sample. (b) At 60,000 cycles, the crack reached to the stage II type growth distinguished by the perpendicular growth to the applied load direction. (c) The same crack along the sample thickness direction at 60,000 cycles. First appeared in [154].

In all fatigue tests involving replica extractions, first cracking was detected around 50% of the total fatigue life, which suggests the importance of crack initiation life. In contrast,

material defects like porosity are often analysed from a fracture mechanics perspective based on the common observation that fatigue cracks initiate from defects relatively early as discussed in Section 2.6. Previous observations in literature were mainly based on small, micron-sized drilled holes or weld toes, where stress concentration factor is much larger compared to a blunt, spherical pore; this could explain the experimental observations made in this study. Given that significant crack initiation life was an unexpected outcome, in the following paragraphs limitations of the replica technique and accuracy of the measurements are discussed in order to put this result into context.

A caveat of the replica measurements that they are limited to surface observations only, thus cracks originating internally cannot be detected, which is a possibility considering that stress concentration factor of a spherical pore is uniform along its circumference as shown in Figure 4.5. However, given that the first detected cracks were still in the microstructurally small stage as shown in Figure 4.24a, an earlier crack initiation from the pore root seems unlikely. Furthermore, even greater proportion of crack initiation life, e.g. 70%, was reported for the same alloy using μCT [56]. But in reality, this proportion is likely to be closer to the reported 50% value here, because of the limited resolution of μCT, the smallest detected crack length was 900 μm in [56]. Moreover in [179], up to 70% crack initiation life was reported for cracks starting from foreign-object damage that has similar morphology and low stress concentration factor as porosity, albeit comparatively larger size with an additional residual stress field.

A smaller crack could also be missed due to the limited measurement resolution. In all experiments, the first crack observation was consistently less than 50 μm length and the smallest being equal to 16.41 μm. The Standard Error (SE) based on the three observations taken for these measurements was less than 1 μm. It should be noted that the smallest measured crack length is highly dependent on the replication interval, which was every 10,000 cycles in this work, and the combination of replicating material resolution, which was down to 0.1 μm according to the supplier, and the microscope resolution. Therefore, in theory it might be possible to detect even a sub-micron crack using a higher resolution microscopy and more frequent replicating intervals. However, in practice this seems unlikely as opening of such a small crack won't be easily distinguishable in the vicinity of a much larger pore. Therefore, it was concluded that the crack initiation life in presence of porosity was significant, noting that the initiation life is defined as the number of cycles to detect a surface breaking crack that is between 16 to 50 μm in length.

Chapter 5

Fatigue design perspectives

5.1 Introduction

The porosity problem in additive manufacturing (AM) is analysed using two different approaches in this Chapter, e.g. local stress based depending on the pore geometry and fracture mechanics based depending on the crack tip stresses. The justification for this choice can be explained as follows: from a physical point of view, fracture mechanics based approaches are valid in presence of cracks. However, the point of crack initiation in total fatigue life cannot be determined definitively due to current limitations in imaging, which are discussed at the end of Section 4.4.3 in the context of replica method and surface porosity. Therefore, fatigue design choices in practice can be driven by needs rather than the actual physics. For instance, common application areas of titanium alloys are hip joint replacement in humans, which are not easily accessible, and fan blades in aerospace, which are subject to very high number of cycles due to vibratory loads. Therefore, fatigue design from a durability perspective might be desirable in practice, i.e. S-N curves, local stresses and fatigue notch factors. However, fatigue cracks expected to initiate early in presence of manufacturing defects as discussed in Section 2.6 of the Literature Review, hence fracture mechanics based approaches might be more suitable from a physical point of view. Consequently, the porosity problem in AM is analysed using both durability and damage tolerant approaches in this Chapter, given that each approach could be useful depending on the industrial application.

5.2 Case against assuming pores as effective cracks

5.2.1 Local stress based framework

In presence of stress-raisers, like porosity or macroscopic features like bolt holes, reduction in fatigue strength is often predicted by using an averaged local stress value instead of the peak elastic stress. For instance in fatigue design recommendations for welded joints [175], the peak stress at the weld toe is averaged either using a fictional radius (R = 1 mm) or by linearising the local stress distribution at certain distances. Furthermore, Taylor [180] showed that the averaging approach to predict fatigue strength of notches could be extended to analysing cracks as well, which leads to producing Kitagawa-Takahashi type diagrams shown in Figure 2.12 of the Literature Review.

Following this understanding, first local elastic stress distributions in the vicinity of a pore and a crack were calculated by using analytical formulations. Then fatigue strength reduction with respect to varying pore and crack dimensions was determined by assuming a critical distance from the peak elastic stress as shown in Figure 5.1, i.e. the so-called point method [79]. This method was selected for demonstration only due to its ease of use, and there are other methods available for calculating the average local stress that correlates well with the reduced fatigue strength values determined experimentally; an overview of other methods can be found here [181] and their predictive capability for the case of Ti-6Al-4V can be found in [182, 183].

Fig. 5.1 Sketch of the approach used in averaging the peak elastic stress. As appeared in [173].

Assuming a far-field axial loading as shown in Figure 5.1, the local elastic stress distribution near a spherical cavity in an infinite body has a closed-form solution as shown in Equation (5.1), which was found using the theory of elasticity [74, 147].

$$\sigma_{\text{local}}(x) = \sigma^{\infty}\left[1.0 + \frac{4-5\vartheta}{14-10\vartheta}\left(\frac{r^3}{(x+r)^3}\right) + \frac{9}{14-10\vartheta}\left(\frac{r^5}{(x+r)^5}\right)\right] \tag{5.1}$$

where σ_{local} is the local stress component parallel to the load direction, σ^{∞} the far-field applied stress, ϑ the Poisson's ratio, x the distance from pore edge perpendicular to the loading direction and r the pore radius. When point of interest is the pore edge, i.e. x=0, then the Equation (5.1) reduces to the stress concentration factor formula given in Equation (4.1).

Considering a plain specimen with fatigue strength σ_N at a specific fatigue life N, reduced fatigue strength due to a pore, σ_{Np}, can be assumed as equivalent to an average stress value found at a certain distance, δ, away from the pore:

$$\begin{gathered}\sigma_{\text{local}}(\delta) = \sigma_{av-p} = \sigma_N\left[1.0 + \frac{4-5\vartheta}{14-10\vartheta}\left(\frac{r^3}{(\delta+r)^3}\right) + \frac{9}{14-10\vartheta}\left(\frac{r^5}{(\delta+r)^5}\right)\right] \\ \sigma_{Np} = \frac{\sigma_N}{K_f} \text{ where } K_f = \frac{\sigma_{av-p}}{\sigma_N} \\ \text{when } r \gg \delta \rightarrow \frac{\sigma_{Np}}{\sigma_N} = \left(\frac{27-15\vartheta}{14-10\vartheta}\right)^{-1} = \text{ constant}\end{gathered} \tag{5.2}$$

As seen in Equation (5.2), fatigue strength reduction is independent of the pore diameter for pores that are sufficiently larger than the selected distance. The physical meaning of this distance is not discussed further, since it was merely seen as a fitting parameter.

Local elastic stress in the vicinity of a crack can be calculated according to the Westergaard solution available in most fatigue textbooks such as [105], see Equation (5.3).

$$\sigma_{\text{local}}(x) = \frac{\sigma^{\infty}}{\sqrt{\left[1-\left(\frac{a}{x+a}\right)^2\right]}} \tag{5.3}$$

where σ_{local} is the local elastic stress component parallel to the load direction, σ^{∞} the far-field applied stress, x the distance from crack tip perpendicular to the loading direction and a the crack size. Alternatively, for long cracks, this equation can be expressed as:

$$\sigma_{\text{local}}(x) = \frac{\sigma^{\infty}\sqrt{\pi a}}{\sqrt{2\pi x}} = \sigma^{\infty}\sqrt{a/2x} \tag{5.4}$$

In presence of a crack, reduced fatigue strength, σ_{Nc}, compared to the crack-free condition, σ_N, can be calculated similarly by following the steps in Equation 5.2.

$$\text{when } a \gg \delta \rightarrow \frac{\sigma_{Nc}}{\sigma_N} = \frac{1}{\sqrt{a/2\delta}} \tag{5.5}$$

In contrast to Equation (5.2), it can be seen that in presence of cracks, fatigue strength reduces monotonically as the crack size increases based on the Equation (5.5). This difference in behaviour between pores and cracks are shown in Figure 5.2.

Fig. 5.2 The difference in fatigue strength reduction with respect to a crack and a spherical pore. As appeared in [173].

Figure 5.2 can be divided into three distinct zones. In the first zone, fatigue strength in presence of porosity, σ_{Np}, is equal to the plain specimen fatigue strength σ_N, i.e. pores are too small to cause any fatigue strength reduction. Beyond a critical pore size, fatigue strength starts to reduce monotonically as marked by Zone 2. Here, it can be stated that sufficiently small pores can be treated as cracks since fatigue strength reduction is similar in both instances as seen in Figure 5.2. In this case, the problem of predicting fatigue strength in presence of a pore can be translated into finding suitable fatigue crack growth threshold for a planar crack of similar size as discussed in Section 2.6 of Literature Review. However, the analogy of assuming pores as effective cracks is valid up to a certain transition pore size as seen in Figure 5.2. After the transition size, fatigue strength reduction for pores saturate to the value given by the plain specimen fatigue strength divided by the stress concentration factor (σ_N/K_t), whereas fatigue strength continues to reduce monotonically for cracks. Therefore,

beyond the transition size (Zone 3 in Figure 5.2), assuming pores as cracks could lead to overly conservative results. Given the infinite body assumption of analytical equations, this statement cannot be extended to cases where pore diameter is comparable to load-bearing component size.

5.2.2 Evaluation of WAAM Ti-6Al-4V fatigue test results

The theoretical behaviour discussed so far, i.e. saturation of fatigue strength reduction beyond a certain transition pore size, will be explored in the experimental data. The majority of the fatigue test data in AM Ti-6Al-4V was generated using naturally occurring defects, i.e. uncontrolled dimensions. In this case, achieving constant life diagrams as in Figure 5.2 is challenging, hence the experimental data was analysed from a constant stress perspective. Given that a power-law relationship exists between stress and fatigue life, such as the Basquin law, reduction of fatigue life in presence of stress raisers should follow a trend similar to in Figure 5.2, albeit at a different scale. In this regard, Figure 5.3 was created, which is a constant stress diagram that shows reduction in fatigue life with respect to the crack initiating pore diameter.

Fig. 5.3 Influence of pore size on fatigue life at given maximum applied stress for WAAM Ti-6Al-4V. (a) 700 MPa, (b) 600 MPa, wrought fatigue data is from [184]. Pore diameter was calculated using Equation 4.2, As appeared in [173]

In Figure 5.3, plain specimen fatigue limit, i.e. the reference case, is marked using the fatigue life of wrought Ti-6Al-4V, which is obtained from [184]. As discussed in the literature review chapter, AM Ti-6Al-4V can reach wrought level performance if the as-built surface roughness is removed and the defects are suppressed using the hot isostatic pressing technique. Figure 5.3 shows that wrought level can still be achieved when the crack initiation

source was embedded pores roughly smaller than 85 μm diameter. This observation suggests the existence of a critical pore size below which the fatigue endurance is unaffected, i.e. Zone 1 in Figure 5.2. At this point, it is important to underscore the potential difference in failure sources between the wrought and AM material. Although the failure source of the wrought data was not provided in the referenced handbook [184], it would be fair to assume a microstructure related failure, e.g. surface initiation due to an unfavourably oriented grain, which is typical for high-cycle fatigue regime of smooth-surface fatigue test coupons. This suggests that AM material had reached the wrought fatigue performance despite the embedded pores as the failure source.

After exceeding a critical pore size, fatigue life reduces significantly as can be observed from Figure 5.3. However, there was not sufficient data available to compare crack versus pore behaviour marked in Zone 2 of Figure 5.2, which can be attributed to working with process-induced defects of uncontrolled dimensions. Still, it is worth pointing out the difference in fatigue life reduction due to embedded pores and surface pores. As previously discussed Section 4.4.1, stress intensity factor is higher at the surface for cracks or defects of the same size, and fatigue crack growth rate is slower for embedded cracks due to different environmental conditions. Therefore, surface pores are expected to be more detrimental compared to embedded pores from a theoretical point of view and this can be observed in the experimental data shown in Figure 5.3. Furthermore based on the preceding arguments, the critical diameter for surface pores is expected to be lower than the embedded pores, i.e. in this study, crack initiating embedded pores in the range of 20 to 59 micron diameter were non-detrimental, but these dimensions cannot be transferred to surface pores considering the discussion provided so far. Unfortunately, crack initiating surface pore data was limited to large diameters in this study, hence an estimation concerning the critical surface pore diameter below which fatigue endurance stays unaffected cannot be made at this stage.

In Figure 5.3, it can be observed that crack initiating surface pores larger than 100 microns diameter do not follow the crack trajectory shown in Figure 5.2, i.e. the fatigue life do not monotonically reduce with a slope of two as per the linear elastic fracture mechanics formulations. It could be argued fatigue life reduction is saturated despite the increase in crack initiation pore diameter by roughly a factor of four, which is in line with the approach presented in Figure 5.2 that assumes full notch sensitivity $K_t = K_f$. Alternatively, it could be also stated that fatigue life still continues to reduce with increasing crack initiating surface pore diameter, albeit with a much shallower slope as can expected from a geometric blunt notch. In fact, Schoenbauer and Mayer [117] reports for martensitic stainless steels, which is an another high-strength alloy example as used in this work, when notch sensitivity is taken

into account by stress gradient approaches, the resulting prediction curve with a shallow slope can predict the experimental data within 10% of the mean fatigue strength values.

A limitation of Figure 5.3 is that the fatigue test data was restricted to finite life regime, i.e. fatigue endurance less than 10^5 cycles. At this regime, a large fraction of fatigue life is spent in the crack growth stage based on the experience from smooth, defect-free test specimens. Replica study presented in Section 4.4.3 suggested a similar outcome for test specimens with surface porosity, i.e. at least half of the fatigue life was spent in the crack growth stage. As a future work, it would be interesting to know, whether a similar outcome to Figure 5.3 can be generated at lower applied stress levels, i.e. fatigue endurance in the order of 10^6 cycles or more, where a large fraction of fatigue life is spent in the crack initiation stage based on the experience from smooth, defect-free test specimens.

As a final remark, although Figure 5.3 seem to suggest a competition between embedded and surface pores, the difference in crack initiating source was related to test sample type, i.e. whether it was fabricated using contaminated or clean wires. As reported in Section 3.11, contaminated batch had significantly more porosity compared to the clean wire batch, e.g. three times more based on a metallographic analysis, hence likelihood of forming surface pores during post-process machining was higher. The difference in defect populations made an influence on fatigue test results: contaminated samples were failed mainly from surface pores, whereas clean samples were failed from embedded pores. This observation is in agreement with literature findings discussed previously, where a dominance of surface pores over embedded pores as crack initiation source was found in [56, 57].

To summarise, when evaluating criticality of a pore, considering it as a small crack could lead to overly conservative estimations in some cases. In practice, this is especially important for high strength materials, where the critical distance, δ, is small. Therefore, notch behaviour could be observed even for small micron-sized pores. Another way of thinking is from a qualitative perspective: for small pores, limited radius of curvature could lead to crack-like behaviour, whereas for larger pores blunt morphology could lead to notch-like behaviour.

5.3 Propagation of fatigue cracks initiated from surface porosity of L-PBF Ti-6Al-4V

5.3.1 Assumptions

Sufficiently small fatigue cracks could depict unexpected behaviour when analysed by using linear elastic fracture mechanics; examples of such behaviour include faster crack growth rates at the same nominal ΔK value compared to long crack growth rates and fatigue crack growth below the ΔK_{th} value as documented in review papers [85] and textbooks [7]. In this regard, two key factors can be listed: (1) small scale yielding condition, and (2) crack-tip shielding mechanisms.

The small scale yielding condition is fulfilled when the ratio of crack size to crack-tip plastic zone is negligible. Given that titanium alloy Ti-6Al-4V used in this work is a high-strength material, this condition is most likely to be fulfilled based on the Irwin formulation given in Equation 5.6. Since this Equation assumes a perfectly elastic-plastic material, a monotonic loading, and a circular plastic zone shape, it is only considered as a first approximation.

$$w = \frac{1}{3\pi}\left(\frac{K_{max}}{\sigma_{ys}}\right)^2 \tag{5.6}$$

where w the plastic zone size, K_{max} the maximum stress intensity factor calculated using Murakami-Endo Equation 2.6 and σ_{ys} the yield strength of the material. Estimated plastic zone size using Equation 5.6 is less than 5 μm considering representative values in this work such as 600 MPa applied maximum stress, 50 μm square root of the projected pore area and 930 MPa yield strength. Therefore, the small scale yielding condition was assumed as fulfilled and the linear-elastic fracture mechanics formulations were used in the remainder.

In this work, the possible loss of similitude between the standardised long crack measurements and small cracks initiating from porosity is most likely related to difference in crack-tip conditions and absence crack-tip shielding mechanisms for small cracks. An example for the former is increased local crack driving force due to the pore notch field, and for the latter is the absence of crack closure at the micron scale.

5.3.2 Similitude

As part of the experimental programme, lengths of surface cracks initiated from pores were measured at certain intervals and provided as “a vs N” data in Figure 4.22. Then, the secant technique was used by plugging the data in Figure 4.22 to Equations 5.7-5.8 for calculating

growth rate (da/dN) data of fatigue cracks initiated from pores. Calculation results are shown in Figure 5.4.

$$\frac{\mathrm{d}a}{\mathrm{d}N} = \frac{a_i - a_{i-1}}{N_i - N_{i-1}} \tag{5.7}$$

$$a_{\mathrm{avg}} = \frac{a_i + a_{i-1}}{2} \tag{5.8}$$

where a is the crack depth or crack length value obtained from replica measurements, N the corresponding fatigue cycle of the measurement and i the measurement number. ASTM E647 standard recommends using a constant Δa (Δ2c) in Equation 5.7 to prevent introducing artificial errors during data reduction stage. This recommendation can be fulfilled by using automatic data logging techniques that rely on electric potential difference or by taking pictures at frequent regular intervals with a light microscope. However, inadequate data was collected due to the labour and material intensive nature of the replica technique, hence constant Δa condition was unfilled. As a result, artificial scatter might be introduced to the data presented in Figure 5.4.

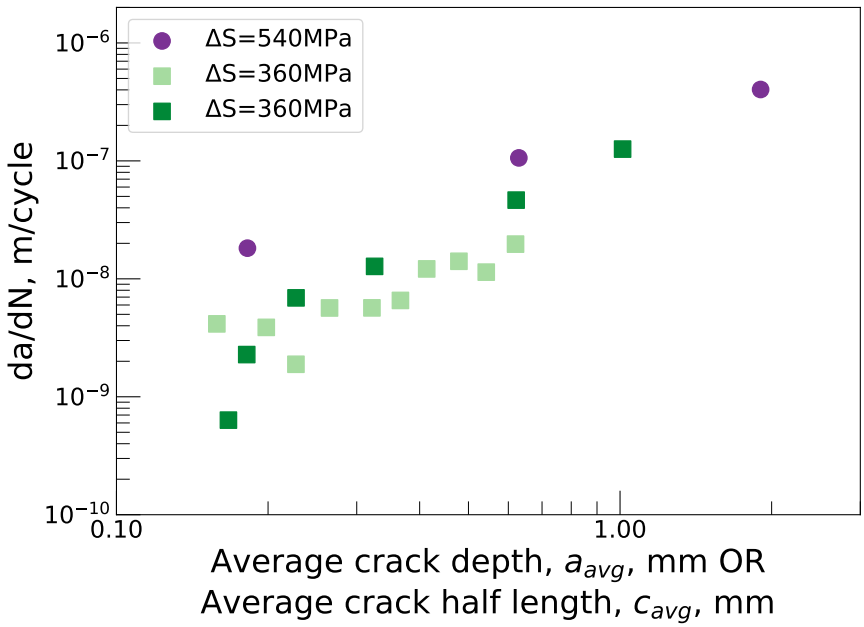

Fig. 5.4 Growth rates of fatigue cracks initiated from surface porosity. Calculated using the secant technique from "a vs N" measurements.

The growth rates presented in Figure 5.4 were compared to “predicted” growth rates using the measured long crack growth data available in the literature. For this purpose, first the crack driving force was calculated using the Newman-Raju formulation [185], see Equation 5.9. Then the calculated ΔK values were plugged-in to the the long crack growth

rate measurements in Figure 2.16 for prediction. Finally, predicted crack growth rate values were compared with the measured values in Figure 5.5.

$$\Delta K = \Delta S \sqrt{\pi \frac{a}{Q}} F\left(\frac{a}{c}, \frac{a}{t}, \varphi\right) \tag{5.9}$$

where ΔS is the applied far-field stress range, a the crack depth, Q the shape factor for a semi-elliptical crack, and F the function for boundary correction taking account of the crack depth (a), crack length (c), plate thickness (t) and specific location (φ) of the ΔK along the ellipse. All Newman-Raju calculations were based on the semi-elliptical surface crack formulation, except the special case described in Section 4.4.3 where a quarter-elliptical corner crack formulation was used to simulate the scenario shown in Figure 4.23b. The surface crack cases consider total length (2c), i.e. pore plus crack length, and the ΔK evaluation was done at the surface, i.e. $\varphi = 0°$. On the other hand, corner crack case uses depth value (a), and the driving force was calculated at the deepest location, i.e. $\varphi = 90°$. Admittedly, these decisions are highly subjective; however, using two different cases was necessary to align better with the available measurement data and reduce systematic errors that could lead to a fortunate result.

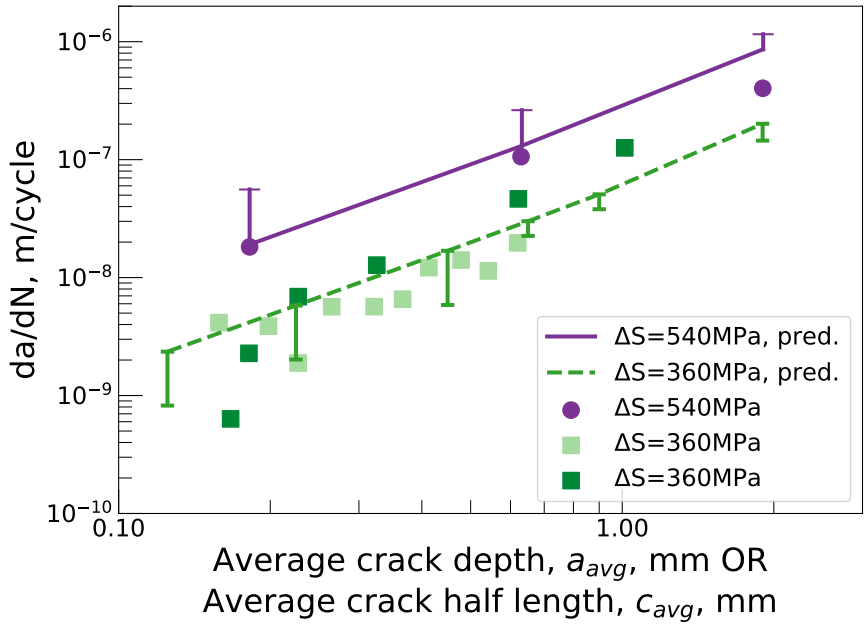

Fig. 5.5 Prediction of the growth rates of fatigue cracks initiated from porosity

In Figure 5.5, dashed prediction lines were calculated using a constant crack aspect ratio of 0.9; this was based on the replica measurements in which the ratio was varied between 0.7 to 0.9 and marker load assisted fracture surface images in which the ratio was 0.9. However,

the experimental data for crack aspect ratio was limited to relatively large cracks, e.g. crack depths of 364 μm (replica) and 400 μm (marker load bands). To compensate this ambiguity, ΔK calculation was re-performed for three additional aspect ratios 0.25, 0.5, 0.75, and added to Figure 5.5 as an error bar. As seen in Figure 5.5, a reasonable agreement between the prediction and measurement data was obtained. This suggests that long crack growth data could be used to predict fatigue life in presence of porosity, when the pore length as seen on the sample surface was added to the actual crack length measurements.

Given that the dimensions of process-induced pores are variable, it is reasonable to expect that adding pore size to the crack length might be insufficient to fulfil similitude condition for certain pore dimensions. Therefore, controlled experiments via artificial defects or cracks could be useful to determine the transition size where similitude to long crack growth rates cannot be achieved.

5.3.3 Small crack behaviour

This Section concentrates on the problem's phenomenology, which is the growth behaviour of fatigue cracks initiated from porosity. The aim was to examine whether the fatigue cracks initiated from pores exhibit an anomalous small crack behaviour, i.e. faster growth rates at the same nominal ΔK value. For this purpose da/dN versus ΔK plot was used and a comparison was made between the long crack growth rates and the growth rates of fatigue cracks initiated from porosity. In contrast to previous Section, measured crack lengths were also used without adding the pore length seen on the surface.

Long crack growth resistance of a material is influenced by the bulk microstructure type, for example bimodal versus lamellar microstructures in titanium alloys. In contrast, growth rate of small cracks does not seem to be influenced by the change in bulk microstructure type as discussed previously in [110, 186]. Therefore, it is expected that the growth rate of small cracks in this work should fall into the same scatter band of growth rates of small cracks available in the literature for Ti-6Al-4V. Given that majority of the available literature data consists of naturally initiated surface cracks, the crack driving force was calculated by using the Newman-Raju formulation (Equation 5.9) for the replica measurements obtained in this work. This calculation assumes a semi-elliptical crack growth and ignores the stress concentration factor of a pore, but allows a direct comparison with the available literature data. To be consistent with the previous Section, an aspect ratio of 0.9 was assumed in Equation 5.9 and the results can be found in Figure 5.6.

Figure 5.6 shows the growth rate of small cracks in the near-threshold zone and below ΔK_{th} of L-PBF Ti-6Al-4V that is between 3-5 MPa$\sqrt{m}$. The literature small crack data consists of conventional manufactured Ti-6Al-4V with either lamellar or bimodal microstruc-

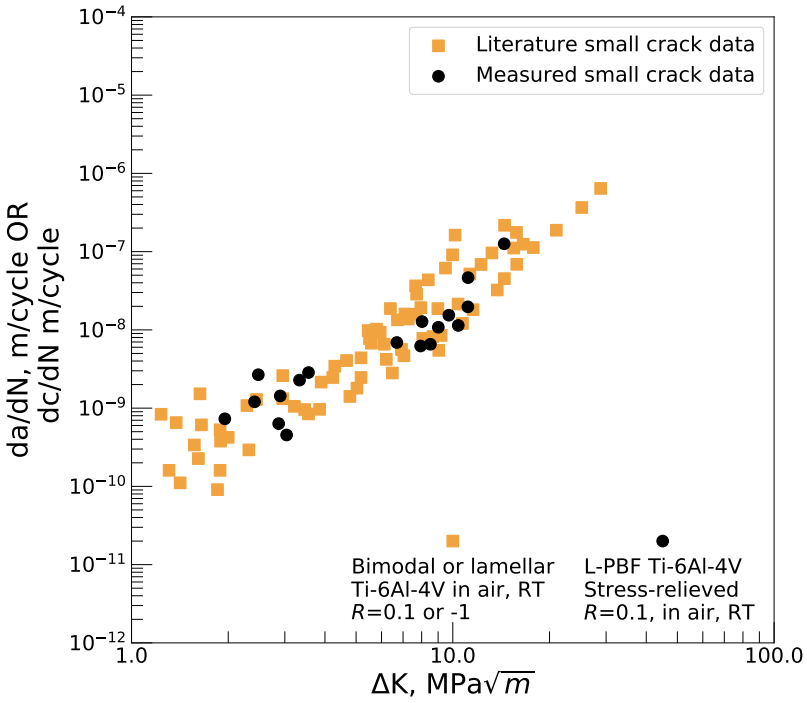

Fig. 5.6 Comparison of the growth rates of small cracks obtained in this work with the literature data from [187, 188, 102]

ture; the small cracks were either naturally initiated surface cracks or were initiated from a foreign object damage that was simulated by firing a sphere on the specimen surface, hence a very similar morphology to surface pores in this work. Figure 5.6 further corroborates the measurements obtained in this work as they fall within the same scatter band of small crack growth data available in the literature.

For investigation of the small crack behaviour, three different formulations were used to calculate the driving force of cracks initiated from pores: (1) semi-elliptical crack growth according to Newman-Raju formulation given in Equation 5.9. (2) Crack-tip embedded in an elastic notch field according to Lukas [189], hence the stress concentration of a pore was taken into account. (3) Equation 2.6 by Murakami and Endo, which implies that the maximum stress intensity factor is dominated by the defect area and the actual crack length can be ignored; hence crack initiating pore size was used as in input. Following these formulations, the generated da/dN vs ΔK plot is shown in Figure 5.7. In this figure, the crack driving force calculated using the Newman-Raju formulation was plotted as a scatter point, while the other formulations included as error bars to visualise the range. When the crack-tip was sufficiently far away from the pore notch zone, e.g. more than a diameter, it was assumed that the fatigue crack initiated from a pore evolved into a semi-elliptical shape and the Newman-Raju formulation (Equation 5.9) was used exclusively. This assumption

corresponded to Paris regime in Figure 5.7 and the error bars were removed since only a single crack driving force was calculated. Furthermore, the crack length was added to pore length at this stage, hence the sudden jump of measurement results in Figure 5.7.

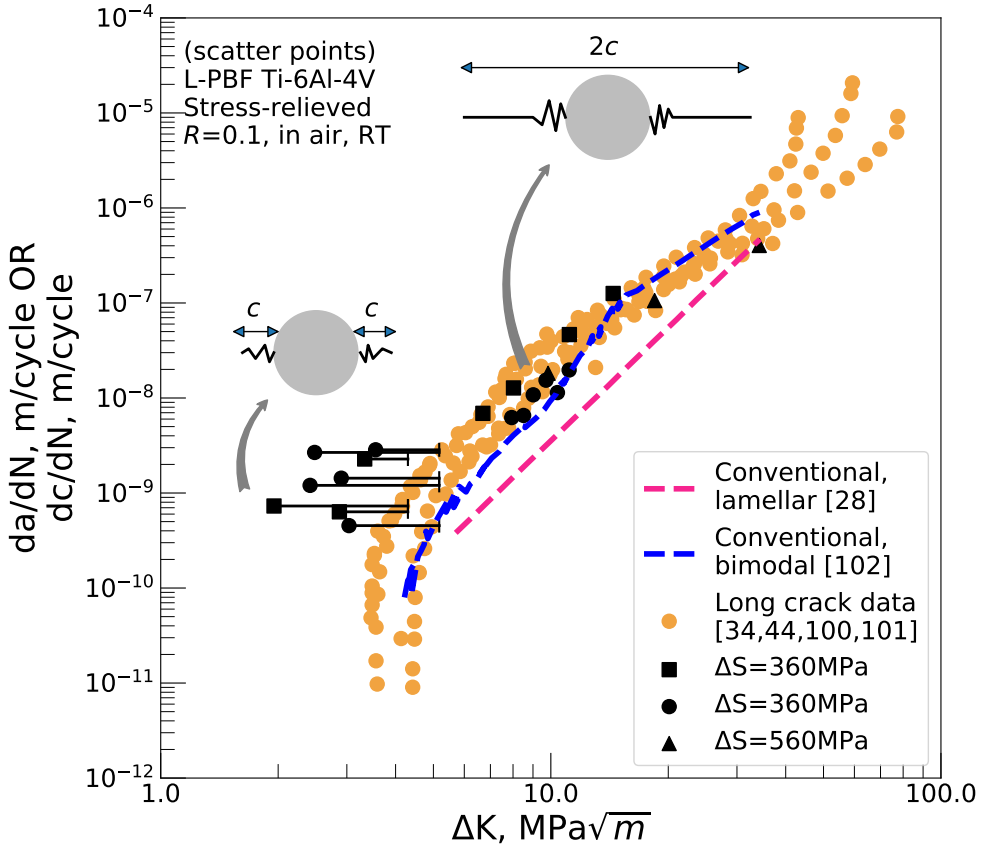

Fig. 5.7 Growth rates of fatigue cracks initiated from porosity compared to the long crack data

As seen in Figure 5.7, fatigue cracks initiated from porosity deviate from the long crack growth rates in the near-threshold regime, which is a common observation for small cracks [85]. After reaching a sufficient length, growth rate of small cracks merge with the long crack growth rates. In Figure 5.7, it can be also observed that the difference in growth rates between small cracks and long cracks are smaller for L-PBF Ti-6Al-4V compared to their conventional manufactured counterparts. This difference in the near-threshold region was further quantified by fitting a mean regression line to the small crack growth rates in Figure 5.7 and comparing with long crack growth curves at the nominal ΔK values of 4, 5 and 6 MPa$\sqrt{m}$. It was found that the small cracks were growing on average 1.74 to 2.20 times faster than the long cracks in L-PBF Ti-6Al-4V, whereas 15.67 to 17.34 times, i.e. an order of magnitude faster than the long cracks in conventional manufactured Ti-6Al-4V.

Fig. 5.8 Comparison of crack front roughness in the near-threshold zone (a) Forged Ti-6Al-4V subjected to a heat treatment for obtaining a coarse lamellar microstructure with α colony size of 500 μm. Originally from [187] and reprinted by permission from Springer Nature. (b) L-PBF Ti-6Al-4V with extremely fine microstructure without any α colony. Originally from [190] and reprinted by permission from Elsevier.

The negligible difference in growth rates of small and large cracks in L-PBF Ti-6Al-4V could be related to weak crack-tip shielding of long cracks. Such a mechanism for instance is the roughness-induced crack closure that under normal circumstances reduce the crack driving force significantly for this alloy; an example crack front profile in the near-threshold zone along with comparison to a conventional manufactured counterpart can be seen in Figure 5.8. The relatively flat crack front profile of L-PBF Ti-6Al-4V is striking in Figure 5.8 and an another example can be found in [101]. This suggests a marginal influence of roughness-induced crack closure in L-PBF Ti-6Al-4V, which could explain negligible difference in growth rates of small and large cracks. Similarly in [191], by using a crack starter notch and a synchrotron X-ray computed tomography, growth rates of small cracks were found to be even slower than long cracks in L-PBF Ti-6Al-4V. This also highlights the variability of small crack growth rates, which is further discussed in [192].

Chapter 6

Conclusions and future work

6.1 Summary

In this work, the influence of process-induced porosity on fatigue of additive manufactured (AM) titanium alloy Ti-6Al-4V was investigated. The aim of this work was contributing to our understanding of the material defect problem in fatigue, which could be helpful in the future when developing assessment methodologies for accepting AM components in service. The scope included two different AM processes: laser powder-bed fusion and wire+arc additive manufacturing; and the scope was limited to high cycle fatigue testing of constant amplitude, axial loading condition in air, at room temperature. In contrast to previous literature, a dedicated experimental programme was developed by circumventing parameters that might influence the fatigue life other than porosity defects. High cycle fatigue testing was supplemented by X-ray Computed Tomography of the gauge volumes to quantify defect population, and by replica extractions to measure growth rates of fatigue cracks initiated from surface pores.

6.2 Main conclusions

Concerning the influence of porosity on fatigue endurance:

1. As opposed to common belief, the influence of pore size on dispersion of fatigue life was found marginal for a Ti-6Al-4V alloy fabricated by laser powder-bed fusion (L-PBF). Despite the size of a crack initiating surface pore was varied by a factor of two, the resulting fatigue life dispersion was significantly smaller when compared to a conventional manufactured counterpart.

2. The main source of fatigue life dispersion due to porosity was found to be the pore type, more specifically pore location e.g. surface versus embedded pores. Despite the presence of a highly dispersed fatigue endurance data for a Ti-6Al-4V alloy fabricated by wire+arc additive manufacturing (WAAM), S-N curves with reasonable accuracy were generated when fatigue endurance data was categorised according to the crack initiating source, e.g. surface or embedded pore.

3. The impact of surface porosity on fatigue endurance was established by carrying-out fatigue test replications at 600 MPa maximum stress using a stress ratio of R=0.1: fatigue life on average (50% probability of failure) was reduced by a factor of 27.8 due to surface pores in L-PBF Ti-6Al-4V when compared to a reference wrought Ti-6Al-4V with bimodal microstructure.

4. X-ray Computed Tomography of fatigue test samples showed that larger pores but not necessarily the largest pore were acting as a crack initiation source under cyclic loading.

   Concerning the influence of porosity on fatigue crack propagation:

5. Fatigue crack growth rates were measured directly from naturally induced porosity for the first time in L-PBF Ti-6Al-4V.

6. Despite measured fatigue cracks were an order of magnitude smaller than the long cracks used in standardised measurements, a similitude to long crack growth rates was observed, when the measured crack lengths were added to the pore length as seen on the surface. This suggests that long crack growth rates could be useful for fatigue design in presence of defects, however, more data is required to further corroborate this finding.

7. When fatigue cracks initiated from surface porosity were considered in isolation, i.e. without adding the pore length, a small crack behaviour was observed: fatigue cracks were growing below the long crack ΔK_{th} value and the measured crack growth rates were higher than the long crack growth rates at the same ΔK value.

   Concerning the fatigue assessment of porosity:

8. Two different evidences were provided against the common assumption of assuming an early crack initiation hence accepting volumetric defects as planar cracks. Firstly, surface breaking cracks of lengths between 10-50 μm were consistently detected around 50% of total fatigue life during replica measurements, i.e. fatigue cracking did

not occur early in life for L-PBF Ti-6Al-4V. Secondly, experimental data of WAAM Ti-6Al-4V did not follow Kitagawa-Takahashi type diagram, i.e. the trend of fatigue life reduction deviated from the slope of two as indicated by linear elastic fracture mechanics formulations. In the light of these evidences, a stress based notch assessment procedure was presented as an alternative for fatigue assessment of porosity.

6.3 Recommendations for future work

1. The scope of this thesis was limited to material defects. In practice, load-bearing components subject to cyclic loading often fail from geometric macro-notches that arise from design features like bolt holes, transition radius and more. The combined effect of a macroscopic notch and process-induced porosity has practical relevance and this work could be used as a building block to tackle this more complex problem due to the introduction of an additional geometric notch.

2. Fatigue of material defects research often rely on artificial defects such as micron-sized drilled holes, lathe turned grooves and more to carry a systematic investigation of effect of defects on certain materials. This work instead concentrated on natural defects, which requires many fatigue tests to achieve statistically significant data. However, it seems plausible that AM technology can print natural defects on demand by locally manipulating process parameters. This feature can be exploited to carry-out a systematic study to further corroborate findings in this work.

3. The morphology of crack initiating pores can deviate from a spherical shape in presence of coalesced pores or keyholes as seen in Figure 4.18b. Yet, the change in defect morphology did not influence the fatigue life of laser powder-bed fusion samples in this thesis. The same conclusion was reached in [166], albeit for a cast Ti-6Al-4V with significantly coarser microstructure. Since the defect morphology was found insignificant, it could be stated that fatigue life was dominated by the crack propagation regime. Yet, the replica study in this work suggested a significant crack initiation life. Therefore, more research is needed for understanding seemingly negligible influence of defect morphology on fatigue life.

4. Fatigue assessment of volumetric defects relies on assuming them as planar cracks based on the experimental observations that cracks initiate from defects usually early in fatigue life. Frost diagram (Figure 2.10) offers a quantitative way to predict this behaviour, i.e. fatigue cracking is expected to initiate early for defects that have

sufficiently high stress concentration factor. In this regard, a fundamental research can be conducted for investigating the limitations of Frost diagrams. For instance, analysing morphologically similar defects in different alloys to see whether fatigue cracking always initiate early in fatigue life. If not, this will signify that the stress concentration factor alone is inadequate for determining the transition zone for accepting volumetric defects as planar cracks.

5. Hot-isostatic pressing (HIP) is often used in metal AM for suppressing the negative effect of defects on fatigue performance. However, HIPing is above the recrystallisation temperature of Ti-6Al-4V and leads to grain coarsening, which is undesirable for high-cycle fatigue strength. Given that X-ray Computed Tomography measurements in this work revealed that the majority of the pores were located immediately beneath the free surface, laser surface polishing techniques could be investigated as an alternative post-processing treatment. These techniques could suppress the sub-surface porosity and retain the favourable fine microstructure.

6. Fatigue life initiation was found significant in this work, hence fatigue life prediction approaches considering the initiation regime could be investigated. In this regard, a classic work by Dowling [193] calculates crack initiation life using the local strains and crack propagation life using linear elastic fracture mechanics.

References

[1] Günther, J., Leuders, S., Koppa, P., Tröster, T., Henkel, S., Biermann, H., & Niendorf, T. (2018). On the effect of internal channels and surface roughness on the high-cycle fatigue performance of Ti-6Al-4V processed by SLM. *Materials & Design*, *143*, 1–11.
https://linkinghub.elsevier.com/retrieve/pii/S0264127518300509

[2] Plocher, J., & Panesar, A. (2019). Review on design and structural optimisation in additive manufacturing: Towards next-generation lightweight structures. *Materials & Design*, *183*, 108164.
https://linkinghub.elsevier.com/retrieve/pii/S0264127519306021

[3] Yin, S., Guo, W., Wang, H., Huang, Y., Yang, R., Hu, Z., Chen, D., Xu, J., & Ritchie, R. O. (2021). Strong and Tough Bioinspired Additive-Manufactured Dual-Phase Mechanical Metamaterial Composites. *Journal of the Mechanics and Physics of Solids*, *149*, 104341.
https://linkinghub.elsevier.com/retrieve/pii/S0022509621000454

[4] Mitchell, A., Lafont, U., Hołyńska, M., & Semprimoschnig, C. (2018). Additive manufacturing — A review of 4D printing and future applications. *Additive Manufacturing*, *24*, 606–626.
https://linkinghub.elsevier.com/retrieve/pii/S2214860417304013

[5] Atzeni, E., & Salmi, A. (2012). Economics of additive manufacturing for end-usable metal parts. *The International Journal of Advanced Manufacturing Technology*, *62*(9-12), 1147–1155.
http://link.springer.com/10.1007/s00170-011-3878-1

[6] Blakey-Milner, B., Gradl, P., Snedden, G., Brooks, M., Pitot, J., Lopez, E., Leary, M., Berto, F., & du Plessis, A. (2021). Metal additive manufacturing in aerospace: A review. *Materials & Design*, *209*, 110008.
https://linkinghub.elsevier.com/retrieve/pii/S0264127521005633

[7] Suresh, S. (1998). *Fatigue of Materials*. Cambridge University Press, 2 ed.
https://www.cambridge.org/core/product/identifier/9780511806575/type/book

[8] Murakami, Y., & Usuki, H. (1989). Quantitative evaluation of effects of non-metallic inclusions on fatigue strength of high strength steels. II: Fatigue limit evaluation based on statistics for extreme values of inclusion size. *International Journal of Fatigue*, *11*(5), 299–307.
https://linkinghub.elsevier.com/retrieve/pii/0142112389900558

[9] Murakami, Y., & Endo, M. (1994). Effects of defects, inclusions and inhomogeneities on fatigue strength. *International Journal of Fatigue*, *16*(3), 163–182. https://linkinghub.elsevier.com/retrieve/pii/0142112394900019

[10] Atkinson, H., & Shi, G. (2003). Characterization of inclusions in clean steels: a review including the statistics of extremes methods. *Progress in Materials Science*, *48*(5), 457–520. https://linkinghub.elsevier.com/retrieve/pii/S0079642502000142

[11] British Standards Institution (2007). *BS 7910: Guide to methods for assessing the acceptability of flaws in metallic structures*. London: BSI. OCLC: 770872248.

[12] Kasperovich, G., Haubrich, J., Gussone, J., & Requena, G. (2016). Correlation between porosity and processing parameters in TiAl6V4 produced by selective laser melting. *Materials & Design*, *105*, 160–170. https://linkinghub.elsevier.com/retrieve/pii/S0264127516306761

[13] DebRoy, T., Wei, H., Zuback, J., Mukherjee, T., Elmer, J., Milewski, J., Beese, A., Wilson-Heid, A., De, A., & Zhang, W. (2018). Additive manufacturing of metallic components – Process, structure and properties. *Progress in Materials Science*, *92*, 112–224. https://linkinghub.elsevier.com/retrieve/pii/S0079642517301172

[14] Gordon, J. V., Narra, S. P., Cunningham, R. W., Liu, H., Chen, H., Suter, R. M., Beuth, J. L., & Rollett, A. D. (2020). Defect structure process maps for laser powder bed fusion additive manufacturing. *Additive Manufacturing*, *36*, 101552. https://linkinghub.elsevier.com/retrieve/pii/S2214860420309246

[15] Biswal, R. (2019). *Impact of porosity on the fatigue performance of wire + arc additive manufactured titanium alloy*. Ph.D. Thesis, Coventry University, United Kingdom. https://pureportal.coventry.ac.uk/en/studentTheses/impact-of-porosity-on-the-fatigue-performance-of-wire-arc-additiv

[16] Herzog, D., Seyda, V., Wycisk, E., & Emmelmann, C. (2016). Additive manufacturing of metals. *Acta Materialia*, *117*, 371–392. https://linkinghub.elsevier.com/retrieve/pii/S1359645416305158

[17] Gibson, I., Rosen, D. W., & Stucker, B. (2015). *Additive manufacturing technologies: 3D printing, rapid prototyping and direct digital manufacturing*. New York London: Springer, 2nd edition ed.

[18] Yadroitsev, I., Yadroitsava, I., Plessis, A. d., & MacDonald, E. (Eds.) (2021). *Fundamentals of laser powder bed fusion of metals*. Additive manufacturing materials and technologies. Amsterdam Kidlington, Oxford Cambridge, MA: Elsevier.

[19] Chastand, V., Quaegebeur, P., Maia, W., & Charkaluk, E. (2018). Comparative study of fatigue properties of Ti-6Al-4V specimens built by electron beam melting (EBM) and selective laser melting (SLM). *Materials Characterization*, *143*, 76–81. https://linkinghub.elsevier.com/retrieve/pii/S1044580317331741

[20] Rafi, H. K., Karthik, N. V., Gong, H., Starr, T. L., & Stucker, B. E. (2013). Microstructures and Mechanical Properties of Ti6Al4V Parts Fabricated by Selective Laser Melting and Electron Beam Melting. *Journal of Materials Engineering and Performance*, *22*(12), 3872–3883. http://link.springer.com/10.1007/s11665-013-0658-0

[21] Zhao, X., Li, S., Zhang, M., Liu, Y., Sercombe, T. B., Wang, S., Hao, Y., Yang, R., & Murr, L. E. (2016). Comparison of the microstructures and mechanical properties of Ti–6Al–4V fabricated by selective laser melting and electron beam melting. *Materials & Design*, *95*, 21–31. https://linkinghub.elsevier.com/retrieve/pii/S0264127515309928

[22] Cunningham, R., Nicolas, A., Madsen, J., Fodran, E., Anagnostou, E., Sangid, M. D., & Rollett, A. D. (2017). Analyzing the effects of powder and post-processing on porosity and properties of electron beam melted Ti-6Al-4V. *Materials Research Letters*, *5*(7), 516–525. https://www.tandfonline.com/doi/full/10.1080/21663831.2017.1340911

[23] King, W. E., Barth, H. D., Castillo, V. M., Gallegos, G. F., Gibbs, J. W., Hahn, D. E., Kamath, C., & Rubenchik, A. M. (2014). Observation of keyhole-mode laser melting in laser powder-bed fusion additive manufacturing. *Journal of Materials Processing Technology*, *214*(12), 2915–2925. https://linkinghub.elsevier.com/retrieve/pii/S0924013614002283

[24] Zhao, C., Fezzaa, K., Cunningham, R. W., Wen, H., De Carlo, F., Chen, L., Rollett, A. D., & Sun, T. (2017). Real-time monitoring of laser powder bed fusion process using high-speed X-ray imaging and diffraction. *Scientific Reports*, *7*(1), 3602. http://www.nature.com/articles/s41598-017-03761-2

[25] Chen, Y., Clark, S. J., Leung, C. L. A., Sinclair, L., Marussi, S., Olbinado, M. P., Boller, E., Rack, A., Todd, I., & Lee, P. D. (2020). In-situ Synchrotron imaging of keyhole mode multi-layer laser powder bed fusion additive manufacturing. *Applied Materials Today*, *20*, 100650. https://linkinghub.elsevier.com/retrieve/pii/S2352940720300986

[26] Vilaro, T., Colin, C., & Bartout, J. D. (2011). As-Fabricated and Heat-Treated Microstructures of the Ti-6Al-4V Alloy Processed by Selective Laser Melting. *Metallurgical and Materials Transactions A*, *42*(10), 3190–3199. http://link.springer.com/10.1007/s11661-011-0731-y

[27] Xu, W., Brandt, M., Sun, S., Elambasseril, J., Liu, Q., Latham, K., Xia, K., & Qian, M. (2015). Additive manufacturing of strong and ductile Ti–6Al–4V by selective laser melting via in situ martensite decomposition. *Acta Materialia*, *85*, 74–84. https://linkinghub.elsevier.com/retrieve/pii/S1359645414008817

[28] Lütjering, G., & Williams, J. C. (2007). *Titanium*. Engineering materials and processes. Berlin ; New York: Springer, 2nd ed ed.

[29] Donachie, M. J. (2000). *Titanium: a technical guide*. Materials Park, OH: ASM International, 2nd ed ed.

[30] Ali, H., Ma, L., Ghadbeigi, H., & Mumtaz, K. (2017). In-situ residual stress reduction, martensitic decomposition and mechanical properties enhancement through high temperature powder bed pre-heating of Selective Laser Melted Ti6Al4V. *Materials Science and Engineering: A*, *695*, 211–220. https://linkinghub.elsevier.com/retrieve/pii/S0921509317304768

[31] Thijs, L., Verhaeghe, F., Craeghs, T., Humbeeck, J. V., & Kruth, J.-P. (2010). A study of the microstructural evolution during selective laser melting of Ti–6Al–4V. *Acta Materialia*, *58*(9), 3303–3312. https://linkinghub.elsevier.com/retrieve/pii/S135964541000090X

[32] Cepeda-Jiménez, C., Potenza, F., Magalini, E., Luchin, V., Molinari, A., & Pérez-Prado, M. (2020). Effect of energy density on the microstructure and texture evolution of Ti-6Al-4V manufactured by laser powder bed fusion. *Materials Characterization*, *163*, 110238. https://linkinghub.elsevier.com/retrieve/pii/S1044580319326063

[33] Murr, L. (2015). Metallurgy of additive manufacturing: Examples from electron beam melting. *Additive Manufacturing*, *5*, 40–53. https://linkinghub.elsevier.com/retrieve/pii/S2214860414000268

[34] Leuders, S., Thöne, M., Riemer, A., Niendorf, T., Tröster, T., Richard, H., & Maier, H. (2013). On the mechanical behaviour of titanium alloy TiAl6V4 manufactured by selective laser melting: Fatigue resistance and crack growth performance. *International Journal of Fatigue*, *48*, 300–307. https://linkinghub.elsevier.com/retrieve/pii/S014211231200343X

[35] Edwards, P., & Ramulu, M. (2014). Fatigue performance evaluation of selective laser melted Ti–6Al–4V. *Materials Science and Engineering: A*, *598*, 327–337. https://linkinghub.elsevier.com/retrieve/pii/S0921509314000720

[36] Simonelli, M., Tse, Y. Y., & Tuck, C. (2014). On the Texture Formation of Selective Laser Melted Ti-6Al-4V. *Metallurgical and Materials Transactions A*, *45*(6), 2863–2872. http://link.springer.com/10.1007/s11661-014-2218-0

[37] Simonelli, M., Tse, Y., & Tuck, C. (2014). Effect of the build orientation on the mechanical properties and fracture modes of SLM Ti–6Al–4V. *Materials Science and Engineering: A*, *616*, 1–11. https://linkinghub.elsevier.com/retrieve/pii/S0921509314009538

[38] Vrancken, B., Thijs, L., Kruth, J.-P., & Van Humbeeck, J. (2012). Heat treatment of Ti6Al4V produced by Selective Laser Melting: Microstructure and mechanical properties. *Journal of Alloys and Compounds*, *541*, 177–185. https://linkinghub.elsevier.com/retrieve/pii/S0925838812011826

[39] Neikter, M., Åkerfeldt, P., Pederson, R., Antti, M.-L., & Sandell, V. (2018). Microstructural characterization and comparison of Ti-6Al-4V manufactured with different additive manufacturing processes. *Materials Characterization*, *143*, 68–75. https://linkinghub.elsevier.com/retrieve/pii/S1044580317326050

[40] Li, P., Warner, D., Fatemi, A., & Phan, N. (2016). Critical assessment of the fatigue performance of additively manufactured Ti–6Al–4V and perspective for future research. *International Journal of Fatigue*, *85*, 130–143. https://linkinghub.elsevier.com/retrieve/pii/S0142112315004399

[41] E08 Committee. E466: Practice for Conducting Force Controlled Constant Amplitude Axial Fatigue Tests of Metallic Materials. Tech. rep., ASTM International. http://www.astm.org/cgi-bin/resolver.cgi?E466-15

[42] BS EN 6072. Aerospace series. Metallic materials. Test methods. Constant amplitude fatigue testing:. Tech. rep., BSI British Standards. https://linkresolver.bsigroup.com/junction/resolve/000000000030209689?restype=standard

[43] Black, J. T., Kohser, R. A., & DeGarmo, E. P. (2008). *DeGarmo's materials and processes in manufacturing*. Hoboken, NJ: Wiley, 10th ed ed.

[44] Greitemeier, D., Dalle Donne, C., Syassen, F., Eufinger, J., & Melz, T. (2016). Effect of surface roughness on fatigue performance of additive manufactured Ti–6Al–4V. *Materials Science and Technology*, *32*(7), 629–634. https://www.tandfonline.com/doi/full/10.1179/1743284715Y.0000000053

[45] Li, P., Warner, D., Pegues, J., Roach, M., Shamsaei, N., & Phan, N. (2019). Towards predicting differences in fatigue performance of laser powder bed fused Ti-6Al-4V coupons from the same build. *International Journal of Fatigue*, *126*, 284–296. https://linkinghub.elsevier.com/retrieve/pii/S0142112319301677

[46] Bagehorn, S., Wehr, J., & Maier, H. (2017). Application of mechanical surface finishing processes for roughness reduction and fatigue improvement of additively manufactured Ti-6Al-4V parts. *International Journal of Fatigue*, *102*, 135–142. https://linkinghub.elsevier.com/retrieve/pii/S0142112317302153

[47] British Standards Institution (1997). Geometric Product Specifications (GPS): surface textures profile method profile method. OCLC: 968937378.

[48] Barari, A., Kishawy, H. A., Kaji, F., & Elbestawi, M. A. (2017). On the surface quality of additive manufactured parts. *The International Journal of Advanced Manufacturing Technology*, *89*(5-8), 1969–1974. http://link.springer.com/10.1007/s00170-016-9215-y

[49] Greitemeier, D., Palm, F., Syassen, F., & Melz, T. (2017). Fatigue performance of additive manufactured TiAl6V4 using electron and laser beam melting. *International Journal of Fatigue*, *94*, 211–217. https://linkinghub.elsevier.com/retrieve/pii/S0142112316300871

[50] Kahlin, M., Ansell, H., & Moverare, J. (2017). Fatigue behaviour of notched additive manufactured Ti6Al4V with as-built surfaces. *International Journal of Fatigue*, *101*, 51–60. https://linkinghub.elsevier.com/retrieve/pii/S0142112317301809

[51] Wycisk, E., Solbach, A., Siddique, S., Herzog, D., Walther, F., & Emmelmann, C. (2014). Effects of Defects in Laser Additive Manufactured Ti-6Al-4V on Fatigue Properties. *Physics Procedia*, *56*, 371–378. https://linkinghub.elsevier.com/retrieve/pii/S187538921400265X

[52] Denti, L., Bassoli, E., Gatto, A., Santecchia, E., & Mengucci, P. (2019). Fatigue life and microstructure of additive manufactured Ti6Al4V after different finishing processes. *Materials Science and Engineering: A*, *755*, 1–9. https://linkinghub.elsevier.com/retrieve/pii/S0921509319304320

[53] Zerbst, U., Madia, M., Klinger, C., Bettge, D., & Murakami, Y. (2019). Defects as a root cause of fatigue failure of metallic components. I: Basic aspects. *Engineering Failure Analysis*, *97*, 777–792. https://linkinghub.elsevier.com/retrieve/pii/S1350630718307556

[54] Romano, S., Brückner-Foit, A., Brandão, A., Gumpinger, J., Ghidini, T., & Beretta, S. (2018). Fatigue properties of AlSi10Mg obtained by additive manufacturing: Defect-based modelling and prediction of fatigue strength. *Engineering Fracture Mechanics*, *187*, 165–189. https://linkinghub.elsevier.com/retrieve/pii/S0013794417310068

[55] Beretta, S., & Romano, S. (2017). A comparison of fatigue strength sensitivity to defects for materials manufactured by AM or traditional processes. *International Journal of Fatigue*, *94*, 178–191. https://linkinghub.elsevier.com/retrieve/pii/S0142112316301645

[56] Tammas-Williams, S., Withers, P. J., Todd, I., & Prangnell, P. B. (2017). The Influence of Porosity on Fatigue Crack Initiation in Additively Manufactured Titanium Components. *Scientific Reports*, *7*(1), 7308. http://www.nature.com/articles/s41598-017-06504-5

[57] Serrano-Munoz, I., Buffiere, J.-Y., & Verdu, C. (2018). Casting defects in structural components: Are they all dangerous? A 3D study. *International Journal of Fatigue*, *117*, 471–484. https://linkinghub.elsevier.com/retrieve/pii/S0142112318303918

[58] Hrabe, N., Gnäupel-Herold, T., & Quinn, T. (2017). Fatigue properties of a titanium alloy (Ti–6Al–4V) fabricated via electron beam melting (EBM): Effects of internal defects and residual stress. *International Journal of Fatigue*, *94*, 202–210. https://linkinghub.elsevier.com/retrieve/pii/S0142112316300767

[59] Qiu, C., Adkins, N. J., & Attallah, M. M. (2013). Microstructure and tensile properties of selectively laser-melted and of HIPed laser-melted Ti–6Al–4V. *Materials Science and Engineering: A*, *578*, 230–239. https://linkinghub.elsevier.com/retrieve/pii/S0921509313005017

[60] Tammas-Williams, S., Withers, P., Todd, I., & Prangnell, P. (2016). Porosity regrowth during heat treatment of hot isostatically pressed additively manufactured titanium components. *Scripta Materialia*, *122*, 72–76. https://linkinghub.elsevier.com/retrieve/pii/S1359646216301737

[61] Booth, G., & Moore, Philippa (2015). *The welding entineer's guide to fracture and fatigue*. Boston, MA: Elsevier, 1st edition ed.

[62] Mercelis, P., & Kruth, J. (2006). Residual stresses in selective laser sintering and selective laser melting. *Rapid Prototyping Journal*, *12*(5), 254–265. https://www.emerald.com/insight/content/doi/10.1108/13552540610707013/full/html

[63] Vrancken, B., Cain, V., Knutsen, R., & Van Humbeeck, J. (2014). Residual stress via the contour method in compact tension specimens produced via selective laser melting. *Scripta Materialia*, *87*, 29–32. https://linkinghub.elsevier.com/retrieve/pii/S1359646214002164

[64] Ahmad, B., van der Veen, S. O., Fitzpatrick, M. E., & Guo, H. (2018). Measurement and modelling of residual stress in wire-feed additively manufactured titanium. *Materials Science and Technology*, *34*(18), 2250–2259. https://www.tandfonline.com/doi/full/10.1080/02670836.2018.1528747

[65] Syed, A. K., Ahmad, B., Guo, H., Machry, T., Eatock, D., Meyer, J., Fitzpatrick, M. E., & Zhang, X. (2019). An experimental study of residual stress and direction-dependence of fatigue crack growth behaviour in as-built and stress-relieved selective-laser-melted Ti6Al4V. *Materials Science and Engineering: A*, *755*, 246–257. https://linkinghub.elsevier.com/retrieve/pii/S0921509319304691

[66] Robinson, J., Ashton, I., Fox, P., Jones, E., & Sutcliffe, C. (2018). Determination of the effect of scan strategy on residual stress in laser powder bed fusion additive manufacturing. *Additive Manufacturing*, *23*, 13–24. https://linkinghub.elsevier.com/retrieve/pii/S2214860418300654

[67] Nicoletto, G., Konečná, R., Frkáň, M., & Riva, E. (2018). Surface roughness and directional fatigue behavior of as-built EBM and DMLS Ti6Al4V. *International Journal of Fatigue*, *116*, 140–148. https://linkinghub.elsevier.com/retrieve/pii/S0142112318302299

[68] Sun, W., Ma, Y., Huang, W., Zhang, W., & Qian, X. (2020). Effects of build direction on tensile and fatigue performance of selective laser melting Ti6Al4V titanium alloy. *International Journal of Fatigue*, *130*, 105260. https://linkinghub.elsevier.com/retrieve/pii/S0142112319303640

[69] Rans, C., Michielssen, J., Walker, M., Wang, W., & Hoen-Velterop, L. 2018). Beyond the orthogonal: on the influence of build orientation on fatigue crack growth in SLM Ti-6Al-4V. *International Journal of Fatigue*, *116*, 344–354. https://linkinghub.elsevier.com/retrieve/pii/S0142112318302731

[70] Zerbst, U., Madia, M., Klinger, C., Bettge, D., & Murakami, Y. (2019). Defects as a root cause of fatigue failure of metallic components. II: Non-metallic inclusions. *Engineering Failure Analysis*, *98*, 228–239. https://linkinghub.elsevier.com/retrieve/pii/S1350630718307568

[71] Zerbst, U., Madia, M., Klinger, C., Bettge, D., & Murakami, Y. (2019). Defects as a root cause of fatigue failure of metallic components. III: Cavities, dents, corrosion pits, scratches. *Engineering Failure Analysis*, *97*, 759–776. https://linkinghub.elsevier.com/retrieve/pii/S135063071830757X

[72] Chapetti, M. D. (2022). Fracture mechanics for fatigue design of metallic components and small defect assessment. *International Journal of Fatigue*, *154*, 106550. https://linkinghub.elsevier.com/retrieve/pii/S0142112321004047

[73] Nadot, Y. (2022). Fatigue from Defect: Influence of Size, Type, Position, Morphology and Loading. *International Journal of Fatigue*, *154*, 106531. https://linkinghub.elsevier.com/retrieve/pii/S0142112321003856

[74] Southwell, R., & Gough, H. (1926). On the concentration of stress in the neighbourhood of a small spherical flaw; and on the propagation of fatigue fractures in "Statistically Isotropic" materials</i>. *The London, Edinburgh, and Dublin Philosophical Magazine and Journal of Science*, *1*(1), 71–97. http://www.tandfonline.com/doi/abs/10.1080/14786442608633614

[75] Borbély, A., Mughrabi, H., Eisenmeier, G., & Höppel, H. (2002). A finite element modelling study of strain localization in the vicinity of near-surface cavities as a cause of subsurface fatigue crack initiation. *International Journal of Fracture*, *115*(3), 227–232. http://link.springer.com/10.1023/A:1016350528652

[76] Pilkey, W. D., Pilkey, D. F., & Peterson, R. E. (2008). *Peterson's stress concentration factors*. Hoboken, N.J: John Wiley, 3rd ed ed. OCLC: ocn175286374.

[77] Sieberer, S., Viehböck, E. G., & Schagerl, M. (2022). Optical stress concentration and stress gradient monitoring during elasto-plastic fatigue tests with Digital Image Correlation. *Materials Today: Proceedings*, *62*, 2543–2548. https://linkinghub.elsevier.com/retrieve/pii/S2214785322016893

[78] Neuber, H. (2001). *Kerbspannungslehre: Theorie der Spannungskonzentration ; genaue Berechnung der Festigkeit*. Klassiker der Technik. Berlin: Springer, 4. aufl ed.

[79] Taylor, D. (2007). *The theory of critical distances: a new perspective in fracture mechanics*. Amsterdam; London: Elsevier. OCLC: 1190745376. https://search.ebscohost.com/login.aspx?direct=true&scope=site&db=e000xna&AN=212282

[80] Frost, N., & Dugdale, D. (1957). Fatigue tests on notched mild steel plates with measurements of fatigue cracks. *Journal of the Mechanics and Physics of Solids*, *5*(3), 182–192. https://linkinghub.elsevier.com/retrieve/pii/0022509657900042

[81] Frost, N. E. (1959). A Relation between the Critical Alternating Propagation Stress and Crack Length for Mild Steel. *Proceedings of the Institution of Mechanical Engineers*, *173*(1), 811–836. http://journals.sagepub.com/doi/10.1243/PIME_PROC_1959_173_065_02

[82] Murakami, Y. (2019). *Metal fatigue: effects of small defects and nonmetallic inclusions*. Waltham, MA: Elsevier, 2nd edition ed.

[83] Newman, J., Phillips, E., Swain, M., & Everett, R. (1992). Fatigue Mechanics: An Assessment of a Unified Approach to Life Prediction. In M. Mitchell, & R. Landgraf (Eds.) *Advances in Fatigue Lifetime Predictive Techniques*, (pp. 5–5–23). 100 Barr Harbor Drive, PO Box C700, West Conshohocken, PA 19428-2959: ASTM International.
http://www.astm.org/doiLink.cgi?STP24150S

[84] E08 Committee. Test Method for Measurement of Fatigue Crack Growth Rates. Tech. rep., ASTM International.
http://www.astm.org/cgi-bin/resolver.cgi?E647-15E1

[85] Suresh, S., & Ritchie, R. O. (1984). Propagation of short fatigue cracks. *International Metals Reviews*, *29*(1), 445–475.
http://www.tandfonline.com/doi/full/10.1179/imtr.1984.29.1.445

[86] Kitagawa, H., & Takahashi, S. (1976). Applicability of fracture mechanics to very small cracks or the cracks in the early stage. In *Proceedings of Second International Conference on Mechanical Behavior of Materials*, (pp. 627–631). Metals Parks, American Society for Metals (ASM).

[87] El Haddad, M. H., Smith, K. N., & Topper, T. H. (1979). Fatigue Crack Propagation of Short Cracks. *Journal of Engineering Materials and Technology*, *101*(1), 42–46.
https://asmedigitalcollection.asme.org/materialstechnology/article/101/1/42/416247/Fatigue-Crack-Propagation-of-Short-Cracks

[88] Smith, R., & Miller, K. (1978). Prediction of fatigue regimes in notched components. *International Journal of Mechanical Sciences*, *20*(4), 201–206.
https://linkinghub.elsevier.com/retrieve/pii/0020740378900826

[89] Tanaka, K., Nakai, Y., & Yamashita, M. (1981). Fatigue growth threshold of small cracks. *International Journal of Fracture*, *17*(5), 519–533.
https://link.springer.com/10.1007/BF00033345

[90] Tanaka, K., & Akiniwa, Y. (1988). Resistance-curve method for predicting propagation threshold of short fatigue cracks at notches. *Engineering Fracture Mechanics*, *30*(6), 863–876.
https://linkinghub.elsevier.com/retrieve/pii/0013794488901464

[91] Chapetti, M. (2003). Fatigue propagation threshold of short cracks under constant amplitude loading. *International Journal of Fatigue*, *25*(12), 1319–1326.
https://linkinghub.elsevier.com/retrieve/pii/S0142112303000653

[92] Murakami, Yukitaka, & Endo Masahiro (1983). Quantitative evaluation of fatigue strength of metals containing various small defects or cracks. *Engineering Fracture Mechanics*, *17*(1), 1–15.
https://linkinghub.elsevier.com/retrieve/pii/0013794483900188

[93] Murakami, Y., & Nemat-Nasser, S. (1983). Growth and stability of interacting surface flaws of arbitrary shape. *Engineering Fracture Mechanics*, *17*(3), 193–210. https://linkinghub.elsevier.com/retrieve/pii/0013794483900279

[94] Murakami, Y. and Endo, M (1986). Effects of Hardness and Crack Geometries on dKth of Small Cracks Emanating from Small Defects. In K. Miller, & E. R. De los Rios (Eds.) *The Behaviour of Short Fatigue Cracks*, vol. 1 of *EGF publication*, (pp. 275–293). London: Mechanical Engineering Publications.

[95] Tammas-Williams, S. (2016). *XCT analysis of the defect distribution and its effect on the static and dynamic mechanical properties in Ti-6Al-4V components manufactured by electron beam additive manufacture*. Ph.D. thesis, University of Manchester.

[96] Sandell, V., Hansson, T., Roychowdhury, S., Månsson, T., Delin, M., Åkerfeldt, P., & Antti, M.-L. (2021). Defects in Electron Beam Melted Ti-6Al-4V: Fatigue Life Prediction Using Experimental Data and Extreme Value Statistics. *Materials*, *14*(3), 640.
https://www.mdpi.com/1996-1944/14/3/640

[97] Leuders, S., Vollmer, M., Brenne, F., Tröster, T., & Niendorf, T. (2015). Fatigue Strength Prediction for Titanium Alloy TiAl6V4 Manufactured by Selective Laser Melting. *Metallurgical and Materials Transactions A*, *46*(9), 3816–3823.
http://link.springer.com/10.1007/s11661-015-2864-x

[98] Masuo, H., Tanaka, Y., Morokoshi, S., Yagura, H., Uchida, T., Yamamoto, Y., & Murakami, Y. (2018). Influence of defects, surface roughness and HIP on the fatigue strength of Ti-6Al-4V manufactured by additive manufacturing. *International Journal of Fatigue*, *117*, 163–179.
https://linkinghub.elsevier.com/retrieve/pii/S0142112318303050

[99] Bellows, R. (1999). Validation of the step test method for generating Haigh diagrams for Ti–6Al–4V. *International Journal of Fatigue*, *21*(7), 687–697.
https://linkinghub.elsevier.com/retrieve/pii/S0142112399000328

[100] Kumar, P., Prakash, O., & Ramamurty, U. (2018). Micro-and meso-structures and their influence on mechanical properties of selectively laser melted Ti-6Al-4V. *Acta Materialia*, *154*, 246–260.
https://linkinghub.elsevier.com/retrieve/pii/S1359645418304117

[101] Tarik Hasib, M., Ostergaard, H. E., Li, X., & Kruzic, J. J. (2021). Fatigue crack growth behavior of laser powder bed fusion additive manufactured Ti-6Al-4V: Roles of post heat treatment and build orientation. *International Journal of Fatigue*, *142*, 105955.
https://linkinghub.elsevier.com/retrieve/pii/S0142112320304874

[102] Caton, M., John, R., Porter, W., & Burba, M. (2012). Stress ratio effects on small fatigue crack growth in Ti–6Al–4V. *International Journal of Fatigue*, *38*, 36–45.
https://linkinghub.elsevier.com/retrieve/pii/S0142112311003008

[103] King, R., Stacey, A., & Sharp, J. (1996). Review of fatigue crack growth rates for offshore steels in air and seawater environments. In *Proceedings of the International Conference on Offshore Mechanics and Arctic Engineering - OMAE*, vol. 3, (pp. 341–348).
https://www.scopus.com/inward/record.uri?eid=2-s2.0-0030359907&partnerID=40&md5=d199c27e8472eaa3fc2e6255a8f5bbc6

[104] Iliopoulos, A. P., Jones, R., Michopoulos, J. G., Phan, N., & Rans, C. (2020). Further Studies into Crack Growth in Additively Manufactured Materials. *Materials*, *13*(10), 2223.
https://www.mdpi.com/1996-1944/13/10/2223

[105] Schijve, J. (Ed.) (2009). *Fatigue of Structures and Materials*. Dordrecht: Springer Netherlands.
http://link.springer.com/10.1007/978-1-4020-6808-9

[106] Elber, W. (1971). The Significance of Fatigue Crack Closure. In M. Rosenfeld (Ed.) *Damage Tolerance in Aircraft Structures*, (pp. 230–230–13). 100 Barr Harbor Drive, PO Box C700, West Conshohocken, PA 19428-2959: ASTM International.
http://www.astm.org/doiLink.cgi?STP26680S

[107] Ritchie, R. (1988). Mechanisms of fatigue crack propagation in metals, ceramics and composites: Role of crack tip shielding. *Materials Science and Engineering: A*, *103*(1), 15–28.
https://linkinghub.elsevier.com/retrieve/pii/0025541688905472

[108] McDowell, D., & Dunne, F. (2010). Microstructure-sensitive computational modeling of fatigue crack formation. *International Journal of Fatigue*, *32*(9), 1521–1542.
https://linkinghub.elsevier.com/retrieve/pii/S0142112310000162

[109] Walker, K., Liu, Q., & Brandt, M. (2017). Evaluation of fatigue crack propagation behaviour in Ti-6Al-4V manufactured by selective laser melting. *International Journal of Fatigue*, *104*, 302–308.
https://linkinghub.elsevier.com/retrieve/pii/S0142112317303043

[110] Jones, R., Raman, R. S., Iliopoulos, A., Michopoulos, J., Phan, N., & Peng, D. (2019). Additively manufactured Ti-6Al-4V replacement parts for military aircraft. *International Journal of Fatigue*, *124*, 227–235.
https://linkinghub.elsevier.com/retrieve/pii/S0142112319300611

[111] Yates, J. R., Efthymiadis, P., Antonysamy, A. A., Pinna, C., & Tong, J. (2019). Do additive manufactured parts deserve better? *Fatigue & Fracture of Engineering Materials & Structures*, *42*(9), 2146–2154.
https://onlinelibrary.wiley.com/doi/abs/10.1111/ffe.13092

[112] Yadollahi, A., Mahtabi, M., Khalili, A., Doude, H., & Newman, J. (2018). Fatigue life prediction of additively manufactured material: Effects of surface roughness, defect size, and shape. *Fatigue & Fracture of Engineering Materials & Structures*, *41*(7), 1602–1614.
http://doi.wiley.com/10.1111/ffe.12799

[113] Shamir, M., Zhang, X., & Syed, A. K. (2021). Characterising and representing small crack growth in an additive manufactured titanium alloy. *Engineering Fracture Mechanics*, *253*, 107876. https://linkinghub.elsevier.com/retrieve/pii/S0013794421003118

[114] Forman, R., & Shivakumar, V. (1986). Growth Behavior of Surface Cracks in the Circumferential Plane of Solid and Hollow Cylinders. In J. Underwood, R. Chait, C. Smith, D. Wilhem, W. Andrews, & J. Newman (Eds.) *Fracture Mechanics: Seventeenth Volume*, (pp. 59–59–16). 100 Barr Harbor Drive, PO Box C700, West Conshohocken, PA 19428-2959: ASTM International. http://www.astm.org/doiLink.cgi?STP17388S

[115] Gupta, A., Sun, W., & Bennett, C. J. (2020). Simulation of fatigue small crack growth in additive manufactured Ti–6Al–4V material. *Continuum Mechanics and Thermodynamics*, *32*(6), 1745–1761. http://link.springer.com/10.1007/s00161-020-00878-0

[116] Murakami, Y. (2012). Material defects as the basis of fatigue design. *International Journal of Fatigue*, *41*, 2–10. https://linkinghub.elsevier.com/retrieve/pii/S0142112311003161

[117] Schönbauer, B. M., & Mayer, H. (2019). Effect of small defects on the fatigue strength of martensitic stainless steels. *International Journal of Fatigue*, *127*, 362–375. https://linkinghub.elsevier.com/retrieve/pii/S0142112319302531

[118] Brandl, E., Greitemeier, D., Maier, H. J., & Syassen, F. (2012). High Cycle Fatigue Properties Of Electron Beam Melted TI-6AL-4V Samples Without And With Integrated Defects ("Effects Of Defects"). vol. 691, (p. 16). https://ui.adsabs.harvard.edu/abs/2012ESASP.691E..16B

[119] Na, J. K., Middendorf, J., Lander, M., Waller, J. M., & Rauser, R. W. (2020). Nondestructive Evaluation of Programmed Defects in Ti-6Al-4V L-PBF ASTM E8-Compliant Dog-Bone Samples. In N. Shamsaei, S. Daniewicz, N. Hrabe, S. Beretta, J. Waller, & M. Seifi (Eds.) *Structural Integrity of Additive Manufactured Parts*, (pp. 206–233). 100 Barr Harbor Drive, PO Box C700, West Conshohocken, PA 19428-2959: ASTM International. https://www.astm.org/doiLink.cgi?STP162020180095

[120] Kahlin, M., Ansell, H., & Moverare, J. (2022). Fatigue crack growth for through and part-through cracks in additively manufactured Ti6Al4V. *International Journal of Fatigue*, *155*, 106608. https://linkinghub.elsevier.com/retrieve/pii/S0142112321004552

[121] of Non-Destructive Testing, T. B. I. (2021). *BINDT Yearbook*. The British Institute of Non-Destructive Testing.

[122] E07 Committee. Guide for Nondestructive Examination of Metal Additively Manufactured Aerospace Parts After Build. Tech. rep., ASTM International. http://www.astm.org/cgi-bin/resolver.cgi?E3166-20E1

[123] Withers, P. J., Bouman, C., Carmignato, S., Cnudde, V., Grimaldi, D., Hagen, C. K., Maire, E., Manley, M., Du Plessis, A., & Stock, S. R. (2021). X-ray computed tomography. *Nature Reviews Methods Primers*, *1*(1), 18. http://www.nature.com/articles/s43586-021-00015-4

[124] Schneider, C. A., Rasband, W. S., & Eliceiri, K. W. (2012). NIH Image to ImageJ: 25 years of image analysis. *Nature Methods*, *9*(7), 671–675. http://www.nature.com/articles/nmeth.2089

[125] Otsu, N. (1979). A Threshold Selection Method from Gray-Level Histograms. *IEEE Transactions on Systems, Man, and Cybernetics*, *9*(1), 62–66. http://ieeexplore.ieee.org/document/4310076/

[126] Cunningham, R., Narra, S. P., Ozturk, T., Beuth, J., & Rollett, A. D. (2016). Evaluating the Effect of Processing Parameters on Porosity in Electron Beam Melted Ti-6Al-4V via Synchrotron X-ray Microtomography. *JOM*, *68*(3), 765–771. http://link.springer.com/10.1007/s11837-015-1802-0

[127] Stef, J., Poulon-Quintin, A., Redjaimia, A., Ghanbaja, J., Ferry, O., De Sousa, M., & Gouné, M. (2018). Mechanism of porosity formation and influence on mechanical properties in selective laser melting of Ti-6Al-4V parts. *Materials & Design*, *156*, 480–493. https://linkinghub.elsevier.com/retrieve/pii/S0264127518305173

[128] Salarian, M., & Toyserkani, E. (2018). The use of nano-computed tomography (nano-CT) in non-destructive testing of metallic parts made by laser powder-bed fusion additive manufacturing. *The International Journal of Advanced Manufacturing Technology*, *98*(9-12), 3147–3153. http://link.springer.com/10.1007/s00170-018-2421-z

[129] Lifton, J., & Liu, T. (2021). An adaptive thresholding algorithm for porosity measurement of additively manufactured metal test samples via X-ray computed tomography. *Additive Manufacturing*, *39*, 101899. https://linkinghub.elsevier.com/retrieve/pii/S2214860421000646

[130] Patterson, B. M., Escobedo-Diaz, J. P., Dennis-Koller, D., & Cerreta, E. (2012). Dimensional Quantification of Embedded Voids or Objects in Three Dimensions Using X-Ray Tomography. *Microscopy and Microanalysis*, *18*(2), 390–398. https://www.cambridge.org/core/product/identifier/S1431927611012554/type/journal_article

[131] Sundar, V., Snow, Z., Keist, J., Jones, G., Reed, R., & Reutzel, E. (2021). Flaw Identification in Additively Manufactured Parts Using X-ray Computed Tomography and Destructive Serial Sectioning. *Journal of Materials Engineering and Performance*, *30*(7), 4958–4964. https://link.springer.com/10.1007/s11665-021-05567-w

[132] British Standards Institution (2020). *6892-1: Metallic materials: tensile testing, Part 1.*. OCLC: 1258068691.

[133] Le, V.-D., Pessard, E., Morel, F., & Prigent, S. (2020). Fatigue behaviour of additively manufactured Ti-6Al-4V alloy: The role of defects on scatter and statistical size effect. *International Journal of Fatigue*, *140*, 105811. https://linkinghub.elsevier.com/retrieve/pii/S014211232030342X

[134] Laz, P., & Hillberry, B. (1998). Fatigue life prediction from inclusion initiated cracks. *International Journal of Fatigue*, *20*(4), 263–270. https://linkinghub.elsevier.com/retrieve/pii/S0142112397001369

[135] Miller, K. J., & De los Rios, E. R. (Eds.) (1986). *The Behaviour of short fatigue cracks*. No. 1 in EGF publication. London: Mechanical Engineering Publications.

[136] Miller, K. J., De los Rios, E. R., & Society, E. S. I. (Eds.) (1992). *Short fatigue cracks*. No. 13 in ESIS publication. London: European Structural Integrity Society : Mechanical Engineering Publications.

[137] He, B. Y., Soady, K. A., Mellor, B. G., Morris, A., & Reed, P. A. S. (2013). Effects of shot peening on short crack growth rate and resulting low cycle fatigue behaviour in low pressure turbine blade material. *Materials Science and Technology*, *29*(7), 788–796. http://www.tandfonline.com/doi/full/10.1179/1743284713Y.0000000230

[138] Swain, M. (1992). Monitoring Small-Crack Growth by the Replication Method. In J. Larsen, & J. Allison (Eds.) *Small-Crack Test Methods*, (pp. 34–34–23). 100 Barr Harbor Drive, PO Box C700, West Conshohocken, PA 19428-2959: ASTM International. http://www.astm.org/doiLink.cgi?STP15063S

[139] Wang, F., Williams, S., Colegrove, P., & Antonysamy, A. A. (2013). Microstructure and Mechanical Properties of Wire and Arc Additive Manufactured Ti-6Al-4V. *Metallurgical and Materials Transactions A*, *44*(2), 968–977. http://link.springer.com/10.1007/s11661-012-1444-6

[140] Biswal, R., Zhang, X., Syed, A. K., Awd, M., Ding, J., Walther, F., & Williams, S. (2019). Criticality of porosity defects on the fatigue performance of wire + arc additive manufactured titanium alloy. *International Journal of Fatigue*, *122*, 208–217. https://linkinghub.elsevier.com/retrieve/pii/S0142112319300295

[141] McAndrew, A. R., Alvarez Rosales, M., Colegrove, P. A., Hönnige, J. R., Ho, A., Fayolle, R., Eyitayo, K., Stan, I., Sukrongpang, P., Crochemore, A., & Pinter, Z. (2018). Interpass rolling of Ti-6Al-4V wire + arc additively manufactured features for microstructural refinement. *Additive Manufacturing*, *21*, 340–349. https://linkinghub.elsevier.com/retrieve/pii/S2214860417306085

[142] Biswal, R., Zhang, X., Shamir, M., Al Mamun, A., Awd, M., Walther, F., & Khadar Syed, A. (2019). Interrupted fatigue testing with periodic tomography to monitor porosity defects in wire + arc additive manufactured Ti-6Al-4V. *Additive Manufacturing*, *28*, 517–527. https://linkinghub.elsevier.com/retrieve/pii/S2214860419300892

[143] Kasperovich, G., & Hausmann, J. (2015). Improvement of fatigue resistance and ductility of TiAl6V4 processed by selective laser melting. *Journal of Materials Processing Technology*, *220*, 202–214. https://linkinghub.elsevier.com/retrieve/pii/S0924013615000278

[144] Mower, T. M., & Long, M. J. (2016). Mechanical behavior of additive manufactured, powder-bed laser-fused materials. *Materials Science and Engineering: A*, *651*, 198–213. https://linkinghub.elsevier.com/retrieve/pii/S092150931530530X

[145] Elambasseril, J., Lu, S., Ning, Y., Liu, N., Wang, J., Brandt, M., Tang, H., & Qian, M. (2019). 3D characterization of defects in deep-powder-bed manufactured Ti–6Al–4V and their influence on tensile properties. *Materials Science and Engineering: A*, *761*, 138031. https://linkinghub.elsevier.com/retrieve/pii/S0921509319308068

[146] Tammas-Williams, S., Zhao, H., Léonard, F., Derguti, F., Todd, I., & Prangnell, P. (2015). XCT analysis of the influence of melt strategies on defect population in Ti–6Al–4V components manufactured by Selective Electron Beam Melting. *Materials Characterization*, *102*, 47–61. https://linkinghub.elsevier.com/retrieve/pii/S104458031500039X

[147] Goodier, J. N. (1933). Concentration of Stress Around Spherical and Cylindrical Inclusions and Flaws. *Journal of Applied Mechanics*, *1*(2), 39–44. https://asmedigitalcollection.asme.org/appliedmechanics/article/1/2/39/1112122/Concentration-of-Stress-Around-Spherical-and

[148] Eshelby, J. D. (1957). The determination of the elastic field of an ellipsoidal inclusion, and related problems. *Proceedings of the Royal Society of London. Series A. Mathematical and Physical Sciences*, *241*(1226), 376–396. https://royalsocietypublishing.org/doi/10.1098/rspa.1957.0133

[149] Dassault Systemes. ABAQUS Version 2021. https://www.3ds.com/products-services/simulia/products/abaqus/

[150] Rotella, A., Nadot, Y., Piellard, M., Augustin, R., & Fleuriot, M. (2020). Influence of defect morphology and position on the fatigue limit of cast Al alloy: 3D characterization by X-ray microtomography of natural and artificial defects. *Materials Science and Engineering: A*, *785*, 139347. https://linkinghub.elsevier.com/retrieve/pii/S0921509320304287

[151] F42 Committee. Specification for Additive Manufacturing Titanium-6 Aluminum-4 Vanadium with Powder Bed Fusion. Tech. rep., ASTM International. http://www.astm.org/cgi-bin/resolver.cgi?F2924-14

[152] Seifi, M., Salem, A., Satko, D., Shaffer, J., & Lewandowski, J. J. (2017). Defect distribution and microstructure heterogeneity effects on fracture resistance and fatigue behavior of EBM Ti–6Al–4V. *International Journal of Fatigue*, *94*, 263–287. https://linkinghub.elsevier.com/retrieve/pii/S0142112316301451

[153] Sharma, H., Parfitt, D., Syed, A., Wimpenny, D., Muzangaza, E., Baxter, G., & Chen, B. (2019). A critical evaluation of the microstructural gradient along the build direction in electron beam melted Ti-6Al-4V alloy. *Materials Science and Engineering: A*, *744*, 182–194. https://linkinghub.elsevier.com/retrieve/pii/S0921509318316952

[154] Akgun, E., Zhang, X., Lowe, T., Zhang, Y., & Doré, M. (2022). Fatigue of laser powder-bed fusion additive manufactured Ti-6Al-4V in presence of process-induced porosity defects. *Engineering Fracture Mechanics*, *259*, 108140. https://linkinghub.elsevier.com/retrieve/pii/S0013794421005452

[155] Maskery, I., Aboulkhair, N., Corfield, M., Tuck, C., Clare, A., Leach, R., Wildman, R., Ashcroft, I., & Hague, R. (2016). Quantification and characterisation of porosity in selectively laser melted Al–Si10–Mg using X-ray computed tomography. *Materials Characterization*, *111*, 193–204. https://linkinghub.elsevier.com/retrieve/pii/S1044580315300711

[156] Romano, S., Brandão, A., Gumpinger, J., Gschweitl, M., & Beretta, S. (2017). Qualification of AM parts: Extreme value statistics applied to tomographic measurements. *Materials & Design*, *131*, 32–48. https://linkinghub.elsevier.com/retrieve/pii/S0264127517305737

[157] Atkinson, H. V., & Davies, S. (2000). Fundamental aspects of hot isostatic pressing: An overview. *Metallurgical and Materials Transactions A*, *31*(12), 2981–3000. http://link.springer.com/10.1007/s11661-000-0078-2

[158] Liu, S., & Shin, Y. C. (2019). Additive manufacturing of Ti6Al4V alloy: A review. *Materials & Design*, *164*, 107552. https://linkinghub.elsevier.com/retrieve/pii/S026412751830916X

[159] Ralf, P. A., Wenzl, J.-P., Lindecke, P., & Emmelmann, C. (2020). FE-Simulation of the influence by material defects on the endurance of additive built metal parts. *Procedia CIRP*, *94*, 378–382. https://linkinghub.elsevier.com/retrieve/pii/S2212827120313378

[160] Benedetti, M., Fontanari, V., Bandini, M., Zanini, F., & Carmignato, S. (2018). Low- and high-cycle fatigue resistance of Ti-6Al-4V ELI additively manufactured via selective laser melting: Mean stress and defect sensitivity. *International Journal of Fatigue*, *107*, 96–109. https://linkinghub.elsevier.com/retrieve/pii/S014211231730419X

[161] Snow, Z., Nassar, A. R., & Reutzel, E. W. (2020). Invited Review Article: Review of the formation and impact of flaws in powder bed fusion additive manufacturing. *Additive Manufacturing*, *36*, 101457. https://linkinghub.elsevier.com/retrieve/pii/S2214860420308290

[162] Childerhouse, T., Hernández-Nava, E., Tapoglou, N., M'Saoubi, R., Franca, L., Leahy, W., & Jackson, M. (2021). The influence of finish machining depth and hot isostatic pressing on defect distribution and fatigue behaviour of selective electron beam melted Ti-6Al-4V. *International Journal of Fatigue*, *147*, 106169. https://linkinghub.elsevier.com/retrieve/pii/S0142112321000293

[163] Romano, S., Nezhadfar, P., Shamsaei, N., Seifi, M., & Beretta, S. (2020). High cycle fatigue behavior and life prediction for additively manufactured 17-4 PH stainless steel: Effect of sub-surface porosity and surface roughness. *Theoretical and Applied Fracture Mechanics*, *106*, 102477.
https://linkinghub.elsevier.com/retrieve/pii/S0167844219307062

[164] Chern, A. H., Nandwana, P., Yuan, T., Kirka, M. M., Dehoff, R. R., Liaw, P. K., & Duty, C. E. (2019). A review on the fatigue behavior of Ti-6Al-4V fabricated by electron beam melting additive manufacturing. *International Journal of Fatigue*, *119*, 173–184.
https://linkinghub.elsevier.com/retrieve/pii/S0142112318305723

[165] Tong, J., Bowen, C. R., Persson, J., & Plummer, A. (2017). Mechanical properties of titanium-based Ti–6Al–4V alloys manufactured by powder bed additive manufacture. *Materials Science and Technology*, *33*(2), 138–148.
https://www.tandfonline.com/doi/full/10.1080/02670836.2016.1172787

[166] Léopold, G., Nadot, Y., Billaudeau, T., & Mendez, J. (2015). Influence of artificial and casting defects on fatigue strength of moulded components in Ti-6Al-4V alloy. *Fatigue & Fracture of Engineering Materials & Structures*, *38*(9), 1026–1041.
https://onlinelibrary.wiley.com/doi/10.1111/ffe.12326

[167] Pineau, A., & Antolovich, S. D. (2016). Probabilistic approaches to fatigue with special emphasis on initiation from inclusions. *International Journal of Fatigue*, *93*, 422–434.
https://linkinghub.elsevier.com/retrieve/pii/S0142112316302687

[168] Murakami, Yukitaka (2001). *Stress intensity factors handbook*. Amsterdam: Elsevier, 3rd [enl.] ed ed. OCLC: 50053100.

[169] Oguma, H., & Nakamura, T. (2013). Fatigue crack propagation properties of Ti–6Al–4V in vacuum environments. *International Journal of Fatigue*, *50*, 89–93.
https://linkinghub.elsevier.com/retrieve/pii/S0142112312000734

[170] Yoshinaka, F., Nakamura, T., Nakayama, S., Shiozawa, D., Nakai, Y., & Uesugi, K. (2016). Non-destructive observation of internal fatigue crack growth in Ti–6Al–4V by using synchrotron radiation CT imaging. *International Journal of Fatigue*, *93*, 397–405.
https://linkinghub.elsevier.com/retrieve/pii/S0142112316301360

[171] Junet, A., Messager, A., Boulnat, X., Weck, A., Boller, E., Helfen, L., & Buffiere, J.-Y. (2019). Fabrication of artificial defects to study internal fatigue crack propagation in metals. *Scripta Materialia*, *171*, 87–91.
https://linkinghub.elsevier.com/retrieve/pii/S1359646219302866

[172] for Standardization, I. O. (2003). *ISO 12107: Metallic materials — Fatigue testing — Statistical planning and analysis of data*. ISO.

[173] Akgun, E., Zhang, X., Biswal, R., Zhang, Y., & Doré, M. (2021). Fatigue of Wire+Arc Additive Manufactured Ti-6Al-4V in Presence of Process-Induced Porosity Defects. *International Journal of Fatigue*, (p. 106315).
https://linkinghub.elsevier.com/retrieve/pii/S0142112321001754

[174] Morrow, J.D. (1968). Fatigue Design Handbook - Advances in Engineering. vol. 4, (pp. 21–29). Warrandale, PA: SAE Society of Automotive Engineers.

[175] Hobbacher, A., & of Welding, I. I. (Eds.) (2016). *Recommendations for fatigue design of welded joints and components: IIW document IIW-2249-15, ex XIII-2460-13/XV-1440-13*. No. 2259-15 in IIW collection. Cham Heidelberg New York: Springer, second edition ed. OCLC: 942855409.

[176] Cao, F., Zhang, T., Ryder, M. A., & Lados, D. A. (2018). A Review of the Fatigue Properties of Additively Manufactured Ti-6Al-4V. *JOM*, *70*(3), 349–357. http://link.springer.com/10.1007/s11837-017-2728-5

[177] Jha, S. K., Szczepanski, C. J., Golden, P. J., Porter, W. J., & John, R. (2012). Characterization of fatigue crack-initiation facets in relation to lifetime variability in Ti–6Al–4V. *International Journal of Fatigue*, *42*, 248–257. https://linkinghub.elsevier.com/retrieve/pii/S0142112311003148

[178] Jordon, J., Bernard, J., & Newman, J. (2012). Quantifying microstructurally small fatigue crack growth in an aluminum alloy using a silicon-rubber replica method. *International Journal of Fatigue*, *36*(1), 206–210. https://linkinghub.elsevier.com/retrieve/pii/S0142112311002052

[179] Peters, J., & Ritchie, R. (2000). Influence of foreign-object damage on crack initiation and early crack growth during high-cycle fatigue of Ti–6Al–4V. *Engineering Fracture Mechanics*, *67*(3), 193–207. https://linkinghub.elsevier.com/retrieve/pii/S001379440000045X

[180] Taylor, D. (1999). Geometrical effects in fatigue: a unifying theoretical model. *International Journal of Fatigue*, *21*(5), 413–420. https://linkinghub.elsevier.com/retrieve/pii/S0142112399000079

[181] Liao, D., Zhu, S., Correia, J. A., De Jesus, A. M., & Berto, F. (2020). Recent advances on notch effects in metal fatigue: A review. *Fatigue & Fracture of Engineering Materials & Structures*, *43*(4), 637–659. https://onlinelibrary.wiley.com/doi/10.1111/ffe.13195

[182] Lanning, D., Nicholas, T., & Palazotto, A. (2005). The effect of notch geometry on critical distance high cycle fatigue predictions. *International Journal of Fatigue*, *27*(10-12), 1623–1627. https://linkinghub.elsevier.com/retrieve/pii/S014211230500126X

[183] Lanning, D., Nicholas, T., & Haritos, G. (2005). On the use of critical distance theories for the prediction of the high cycle fatigue limit stress in notched Ti-6Al-4V. *International Journal of Fatigue*, *27*(1), 45–57. https://linkinghub.elsevier.com/retrieve/pii/S0142112304001306

[184] Welsch, G., Boyer, R., & Collings, E. W. (Eds.) (1994). *Materials properties handbook: titanium alloys*. Materials Park, OH: ASM International.

[185] Newman, J., & Raju, I. (1981). An empirical stress-intensity factor equation for the surface crack. *Engineering Fracture Mechanics*, *15*(1-2), 185–192. https://linkinghub.elsevier.com/retrieve/pii/0013794481901168

[186] Rao, K., Yu, W., & Ritchie, R. (1988). On the behavior of small fatigue cracks in commercial aluminum-lithium alloys. *Engineering Fracture Mechanics*, *31*(4), 623–635.
https://linkinghub.elsevier.com/retrieve/pii/0013794488901051

[187] Nalla, R. K., Ritchie, R. O., Boyce, B. L., Campbell, J. P., & Peters, J. O. (2002). Influence of microstructure on high-cycle fatigue of Ti-6Al-4V: Bimodal vs. lamellar structures. *Metallurgical and Materials Transactions A*, *33*(3), 899–918.
http://link.springer.com/10.1007/s11661-002-0160-z

[188] Peters, J. O., & Lütjering, G. (2001). Comparison of the fatigue and fracture of + and titanium alloys. *Metallurgical and Materials Transactions A*, *32*(11), 2805–2818.
http://link.springer.com/10.1007/s11661-001-1031-8

[189] Lukáš, P. (1987). Stress intensity factor for small notch-emanated cracks. *Engineering Fracture Mechanics*, *26*(3), 471–473.
https://linkinghub.elsevier.com/retrieve/pii/0013794487900270

[190] Konečná, R., Kunz, L., Bača, A., & Nicoletto, G. (2017). Resistance of direct metal laser sintered Ti6Al4V alloy against growth of fatigue cracks. *Engineering Fracture Mechanics*, *185*, 82–91.
https://linkinghub.elsevier.com/retrieve/pii/S0013794417300292

[191] Waddell, M., Walker, K., Bandyopadhyay, R., Kapoor, K., Mallory, A., Xiao, X., Chuang, A. C., Liu, Q., Phan, N., & Sangid, M. D. (2020). Small fatigue crack growth behavior of Ti-6Al-4V produced via selective laser melting: In situ characterization of a 3D crack tip interactions with defects. *International Journal of Fatigue*, *137*, 105638.
https://linkinghub.elsevier.com/retrieve/pii/S0142112320301699

[192] Jones, R., Rans, C., Iliopoulos, A. P., Michopoulos, J. G., Phan, N., & Peng, D. (2021). Modelling the Variability and the Anisotropic Behaviour of Crack Growth in SLM Ti-6Al-4V. *Materials*, *14*(6), 1400.
https://www.mdpi.com/1996-1944/14/6/1400

[193] Dowling, N. E. (1979). Notched Member Fatigue Life Predictions Combining Crack Initiation and Propagation. *Fatigue & Fracture of Engineering Materials and Structures*, *2*(2), 129–138.
https://onlinelibrary.wiley.com/doi/10.1111/j.1460-2695.1979.tb01349.x

Appendix A

Tabulated results of high cycle fatigue testing

This Appendix provides tabulated high cycle fatigue testing results to support S-N diagrams given in Figure 4.16. This table was also used as the source data for the analyses made in this work. For the wire+arc additive manufactured (WAAM) samples, a remark was made to clarify whether the sample was produced using clean wires or intentionally contaminated wires to promote porosity. On the other hand, remark column in laser powder-bed fusion samples (L-PBF) correspond to additional data such as X-ray Computed Tomography prior to fatigue testing or replica measurement during fatigue testing. Please note that, all fatigue tests were under nominally similar conditions as follows:

- Load-controlled
- Axial loading
- Constant amplitude
- Stress ratio R=0.1
- Mechanically ground and polished sample surface
- In air, at room temperature
- Run-out was defined as 1e07 cycles. After reaching selected number of cycles, the run-out samples were tested at a higher load to determine crack initiating source.

Table A.1 Detailed fatigue test results of wire+arc additive manufacturing

ID	Process	Specimen geometry	σ_{max} MPa	N_f cycles	Remark[(1)]	Crack Init. source	Morphology	$\sqrt{area}$ μm
01	WAAM	Cylindrical	500	351,311	Contaminated	Surface pore	Circular	215.04
02	WAAM	Cylindrical	500	133,723	Contaminated	Surface pore	Semi-circular	100.29
03	WAAM	Cylindrical	500	714,761	Contaminated	Clustered pores	-	-
04	WAAM	Cylindrical	500	253,192	Contaminated	Clustered pores	-	-
05	WAAM	Cylindrical	500	61,667	Contaminated	Deep scratch	-	-
06	WAAM	Cylindrical	500	325,457	Contaminated	Surface pore	Circular	105.47
B-01	WAAM	Cylindrical	500	2,640,141	Clean	Microstructure	-	-
B-02	WAAM	Cylindrical	500	3,953,620	Clean	Surface pore	Semi-circular	81.24
B-03	WAAM	Cylindrical	500	6,859,239	Clean	Embedded pore	Circular	27.43
B-04	WAAM	Cylindrical	800	185,700	Clean	Microstructure	-	-
B-05	WAAM	Cylindrical	800	43,391	Clean	Microstructure	-	-
B-06	WAAM	Cylindrical	800	17,232	Clean	Shallow scratch	-	-

(1) Contaminated case refers to samples in which the feedstock wires were sprayed with an organic contaminant to promote porosity formation. For more details, please refer to the Chapter 3 - Experimental Programme.

Table A.2 Fatigue test results of wire+arc additive manufacturing obtained in a previous study [15]

(1) Contaminated case refers to samples in which the feedstock wires were sprayed with an organic contaminant to promote porosity formation. For more details, please refer to the Chapter 3 - Experimental Programme.

Table A.3 Detailed fatigue test results of laser powder-bed fusion

ID[1]	Process	Specimen geometry	σ_{max} MPa	N_f cycles	Remark	Crack Init. source	Morphology	$\sqrt{area}$ μm
NNS-1	L-PBF	Cylindrical	500	104,390	n.a.	Surface pore	Irregular	60.66
NNS-2	L-PBF	Cylindrical	400	281,588	μXCT	Surface pore	Irregular?	66.00
NNS-3	L-PBF	Cylindrical	500	59,980	μXCT	Roughness	n.a.	n.a.
NNS-4	L-PBF	Cylindrical	335	399,041	μXCT	Surface pore	Irregular	78.62
NNS-5	L-PBF	Cylindrical	400	216,797	μXCT	Surface pore	Irregular	76.8
NNS-6	L-PBF	Cylindrical	600	48,835	μXCT	Surface pores	Irregular	84.5
NNS-7	L-PBF	Cylindrical	500	44,687	μXCT	Roughness	n.a.	n.a.
NNS-8	L-PBF	Cylindrical	600	53,624	μXCT	Surface pore	Circular	68.79
NNS-9	L-PBF	Cylindrical	335	run-out	n.a	Surface pore	Circular	47.69
NNS-10	L-PBF	Cylindrical	400	66,063	μXCT	Roughness	n.a.	n.a.
NNS-11	L-PBF	Cylindrical	500	90,310	n.a	Surface pore	Semi-circular	71.17
NNS-12	L-PBF	Cylindrical	335	369,980	μXCT	Roughness	n.a.	n.a.
DF-3[2]	L-PBF	Cylindrical	535	10,000,000	Step[4]	Embedded pore	Irregular	54.15
DF-30[2]	L-PBF	Cylindrical	600	run-out	n.a.	Microstructure	n.a.	n.a.
DF-49[2]	L-PBF	Cylindrical	655	209,636	n.a.	Surface pore	Semi-circular	81.85
15-1[2]	L-PBF	Rectangular	600	102,672	n.a.	Surface pore	Irregular	42.45
15-2[2]	L-PBF	Rectangular	600	282,182	n.a.	Microstructure	n.a.	n.a.
19-T	L-PBF	Rectangular	600	71,033	Replica	Surface pore	Circular	57.80
34-T[3]	L-PBF	Rectangular	600	60,000	Replica	Surface pore	Circular	n.a.
38-1[2]	L-PBF	Rectangular	600	104,712	n.a.	Surface pore	Irregular	55.81
38-2[2]	L-PBF	Rectangular	600	101,562	n.a.	Surface pore	Semi-circular	44.87
38-3[2]	L-PBF	Rectangular	600	91,446	n.a.	Surface pore	Irregular	42.40
S-1	L-PBF	Rectangular	270	142,566	Replica	Lack-of-fusion	n.a.	n.a.
S-2	L-PBF	Rectangular	400	160,749	Replica	Surface pore	Semi-circular	135.45
S-4	L-PBF	Rectangular	400	150,543	Replica	Surface pore	Semi-circular	155.67
S-5	L-PBF	Rectangular	400	108,425	Replica	Surface pore	Irregular	107.57

(1) NNS refers to samples manufactured in Near Net Shape as discussed in Chapter 3 - Experimental Programme.

(2) The defect rich region beneath the surface (Figure 4.11) was removed during grinding and polishing step.

(3) When the crack length as seen on the surface was approximately 1.5mm, the cyclic loading was stopped at 60,000 cycles and a quasi-static tensile load was applied until failure. This procedure enabled to reveal the crack shape initiated from porosity as seen in Figure 4.23b, however, it concealed the dimensions of crack initiating pore diameter seen on the fracture surface.

(4) Step testing technique [99] was conducted to determine fatigue strength at 10^7 cycles.

Appendix B

Tabulated results of fatigue crack growth measurements

This Appendix provides raw measurements obtained using the replica technique. The data given in Tables B.1-B.4 were used as an input to generate plots presented in Section 5.3. The naming terminology to present raw data is shown in Figure B.1.

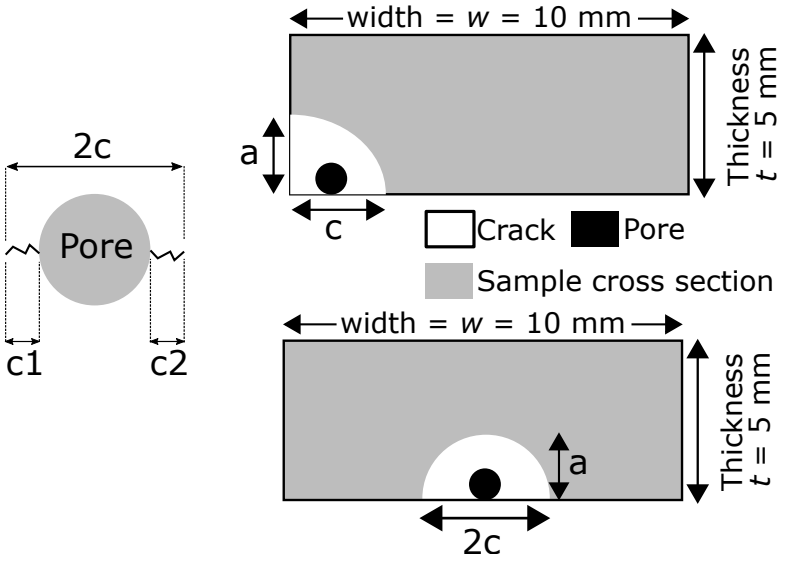

Fig. B.1 Sketch of the naming convention followed in Tables B.1-B.4

Table B.1 Sample ID = 19-T, $\Delta\sigma$ = 540 MPa

Cycles	Crack length (μm)			Crack depth (μm)
	c_1	c_2	c	a
20,000	0	0	0	0
40,000	46.04	12.47	107.05	0
60,000	309.0	141.0	498.54	364.0
65,000	n.a.	n.a.	n.a.	900.0
70,000	n.a.	n.a.	n.a.	2610.0

Table B.2 Sample ID = 34-T, $\Delta\sigma$ = 540 MPa

Cycles	Crack length (μm)			Crack depth (μm)
	c_1	c_2	2c	a
20,000	0	0	0	0
40,000	n.a.	n.a.	202.70	0
60,000	n.a.	n.a.	1492.14	1553.85

Table B.3 Sample ID = S-4, $\Delta\sigma$ = 360 MPa

Cycles	Crack length (μm)			Crack depth (μm)
	c_1	c_2	2c	a
60,000	0	0	0	0
70,000	35.78	47.21	358.0	0
80,000	89.24	71.28	435.52	0
90,000	98.32	99.93	473.25	0
100,000	154.57	156.92	586.48	0
110,000	211.92	201.24	699.93	0
115,000	n.a.	n.a.	765.53	0
120,000	n.a.	n.a.	886.89	0
125,000	n.a.	n.a.	1027.76	0
130,000	n.a.	n.a.	1141.73	484.64
135,000	n.a.	n.a.	1338.70	886.17

Table B.4 Sample ID = S-5, $\Delta\sigma$ = 360 MPa

Cycles	Crack length (μm)			Crack depth (μm)
	c_1	c_2	2c	a
53,000	77.37	0	327.37	0
63,000	90.05	0	340.06	0
73,000	135.65	0	385.65	0
83,000	214.37	43.34	523.51	0
93,000	254.42	269.21	778.65	485.47
103,000	n.a.	n.a.	1708.72	1317.12
105,500	n.a.	n.a.	2338.28	2084.63

Appendix C

Image segmentation of X-ray Computed Tomography

This appendix presents the Python code developed as part of this thesis to analyse X-ray Computed Tomography measurements. The code imports segmented image data, track pores that appear on more than one projection and selects the instance with maximum projected area, which is later used in the plotted histograms. Finally, the developed code was compared to the output of an commercially available software, namely Avizo, for verification. Since different image segmentation algorithms were used, an exact match between the commercial software and the developed code was not possible. Yet, as seen in the following, the developed code produces a reasonably accurate output both for the distribution statistics, e.g. mean, standard deviation, and as well as for the shape of the distribution.

[8]:
```
import unicodecsv
import matplotlib.pyplot as plt
from math import pi, sqrt
import pandas as pd
import numpy as np
import csv
from matplotlib.ticker import FormatStrFormatter
from matplotlib.patches import Patch
```

- FIJI was used instead of ImageJ, because the latter had **memory** issues with 1659 images.
- File → Import → Image Sequence
  - Click convert to 8-bit
  - Import as "Virtual Stack"
- Crop image 824x824 pixel
- Set scale 1 px = 7 microns
- Process → Filter
  - Gaussian Blur, r = 2px
- Image → Adjust → Threshold
  - Otsu method
- Process → Binary → Open
- Process → Binary → Close
- Analyze → Analyse Particles
  - Size threshold 200 - inf.
  - Circularity 0.5 - 1.0
  - Show: Overlay masks
  - Exclude on edges

[2]:
```
#Import number of detected pores in each slide
NNS8_count = []
with open('/Users/akgune/OneDrive - Coventry University/kodlama/EOS/NNS8_rev00/
 ↪Summary.csv','rb') as f:
    reader = unicodecsv.DictReader(f)
    for row in reader:
        NNS8_count.append(int(row['Count']))

#Create a list including slide numbers
NNS8_slides = range(1,len(NNS8_count)+1)
```

[3]:
```
#Create individual lists based on Area and Spatial Locations(X and Y)
NNS8_A = []
NNS8_X = []
NNS8_Y = []

with open('/Users/akgune/OneDrive - Coventry University/kodlama/EOS/NNS8_rev00/
 ↪Results.csv','rb') as f:
    reader = unicodecsv.DictReader(f)
    for row in reader:
```

```
        NNS8_A.append(float(row['Area']))
        NNS8_X.append(float(row['X']))
        NNS8_Y.append(float(row['Y']))

#Create two new lists
#PoreNo is number of pores in each slide in ascending order, i.e. 1 2 3 4...
#Slide2 is dummy in case a slide has more than 1 pores, than it is written more␣
 ↪than once, i.e. Slide 2, Slide 2 etc.
i = 0
j = 0
NNS8_PoreNo = []
NNS8_slides2 = []
while i < len(NNS8_count):
    if NNS8_count[i] < 2:
        NNS8_PoreNo.append(NNS8_count[i])
        NNS8_slides2.append(NNS8_slides[i])
        j += 1
    if NNS8_count[i] >= 2:
        k = 1
        while k <= NNS8_count[i]:
            NNS8_PoreNo.append(k)
            NNS8_slides2.append(NNS8_slides[i])
            k += 1
        k = 1
    i += 1

#Include slides with zero pores
i = 0
j = 1
tracker =[]
while i < len(NNS8_count):
    if NNS8_count[i]==1:
        tracker.append(j)
        j += 1
    if NNS8_count[i]==0:
        tracker.append(j)
        dummy=tracker.index(j)
        NNS8_A.insert(dummy,0.0)
        NNS8_X.insert(dummy,0.0)
        NNS8_Y.insert(dummy,0.0)
        j += 1
    if NNS8_count[i]>1:
        k = 0
        while k < NNS8_count[i]:
            tracker.append(j)
            k += 1
        j += 1
```

```
    i += 1
```

[4]:
```
#Create a MultiIndex list

i = 0
with open("track.csv", "wb") as infile:
    writer = csv.writer(infile)
    writer.writerow(["SlideNo","PoreNo", "Area", "X", "Y"])    #Write Header
    for i in zip(NNS8_slides2, NNS8_PoreNo, NNS8_A, NNS8_X, NNS8_Y):
        writer.writerow(i)                  #Write Content

z = pd.read_csv("track.csv", index_col=[0,1])
```

[5]:
```
#Drop pore repetitions

k = 1
pp = 1
while k < 1659:
    for (i,m) in zip(z.loc[k,'X'],z.loc[k,'Area']):
        for (j,n) in zip(z.loc[k+1,'X'],z.loc[k+1,'Area']):
            if (i-j) < 100:
                if (m-n) < 0:
                    z.loc[(k,pp),'Area'] = np.NaN
                else:
                    z.loc[(k+1,pp),'Area'] = np.NaN
            pp += 1
    k += 1
    pp = 1

zed = z.dropna()
```

[6]:
```
#### Drop slides without any detected pores
NNS8_A0 = []
NNS8_SlideNo0 = []
for (i,j) in zip(zed.loc[:,'Area'],zed.index.get_level_values(level='SlideNo')):
    if i > 0 and i < 17000:
        NNS8_A0.append(i)
        NNS8_SlideNo0.append(j)

NNS8_X0 = []
for (i,j) in zip(zed.loc[:,'X'],zed.loc[:,'Area']):
    if i > 0 and j < 17000:
        NNS8_X0.append(i)

NNS8_Y0 = []
for (i,j) in zip(zed.loc[:,'Y'],zed.loc[:,'Area']):
    if i > 0 and j < 17000:
```

```
        NNS8_Y0.append(i)
```

[55]:
```
NNS8_dPcorr = [2.0*sqrt(i/pi) for i in NNS8_A0]
mean = np.mean(NNS8_dPcorr)
std = np.std(NNS8_dPcorr)
#print mean, std, max(NNS8_dPcorr)

d_CIP = (74.0+69.2)/2.0
d_CIPa = [39, 40, 48, 48, 65, 71]

plt.rcParams.update({'font.size': 14,'figure.dpi':100})
fig, ax = plt.subplots(figsize=(7,5))
counts, bins, patches = ax.hist(NNS8_dPcorr, facecolor='#bdbdbd',␣
 ↪edgecolor='black')
#ax.set_ylabel('Pore Population')
ax2 = ax.twinx()
ax2.set_ylim([0,5])
ax2.spines['right'].set_color('red')
ax2.tick_params(axis='y', colors='red')
ax2.yaxis.label.set_color('red')
counts, bins, patches = ax2.hist(d_CIP, bins, facecolor='red',␣
 ↪edgecolor='black', alpha=0.7)
#ax2.set_ylabel('Crack Initiating Pore')
# Set the ticks to be at the edges of the bins.
ax.set_xticks(bins)
# Set the xaxis's tick labels to be formatted with 1 decimal place...
ax.xaxis.set_major_formatter(FormatStrFormatter('%.0f'))
ax.set_xlabel("Pore diameter, microns",family="sans-serif",  fontsize=16)
ax.set_ylabel("No. of pores in gauge section",family="sans-serif",  fontsize=16)
ax.tick_params(axis='both',which='major', direction="out", bottom="on",␣
 ↪length=6, labelsize=14)
ax.tick_params(axis='both',which='minor', direction="out", bottom="on",␣
 ↪length=6, labelsize=14)
ax2.tick_params(axis='both',which='major', direction="out", bottom="on",␣
 ↪length=6, labelsize=14)
ax2.tick_params(axis='both',which='minor', direction="out", bottom="on",␣
 ↪length=6, labelsize=14)
ax2.set_ylabel("No. of crack initiating pores",family="sans-serif",  fontsize=16)
plt.xlim([23.7,82.2])
legend_elements = [Patch(facecolor='#bdbdbd', edgecolor='k',label='Pore size␣
 ↪population'),
                   Patch(facecolor='red', edgecolor='k',label='Crack initiating␣
 ↪pores')]
plt.legend(handles=legend_elements, bbox_to_anchor=(0., 1.02, 1., .102),␣
 ↪loc='lower left',
           ncol=1, mode="expand", borderaxespad=0.)
```

```
ax.annotate("",
            xy=(80, 12), xycoords='data',
            xytext=(74, 12), textcoords='data', size = 16,
            arrowprops=dict(arrowstyle="simple",
                            connectionstyle="arc3", color="red"),
            )
fig.tight_layout()
plt.show()
fig.savefig("NNS8_poreDia.pdf", format="pdf",dpi=1000)
```

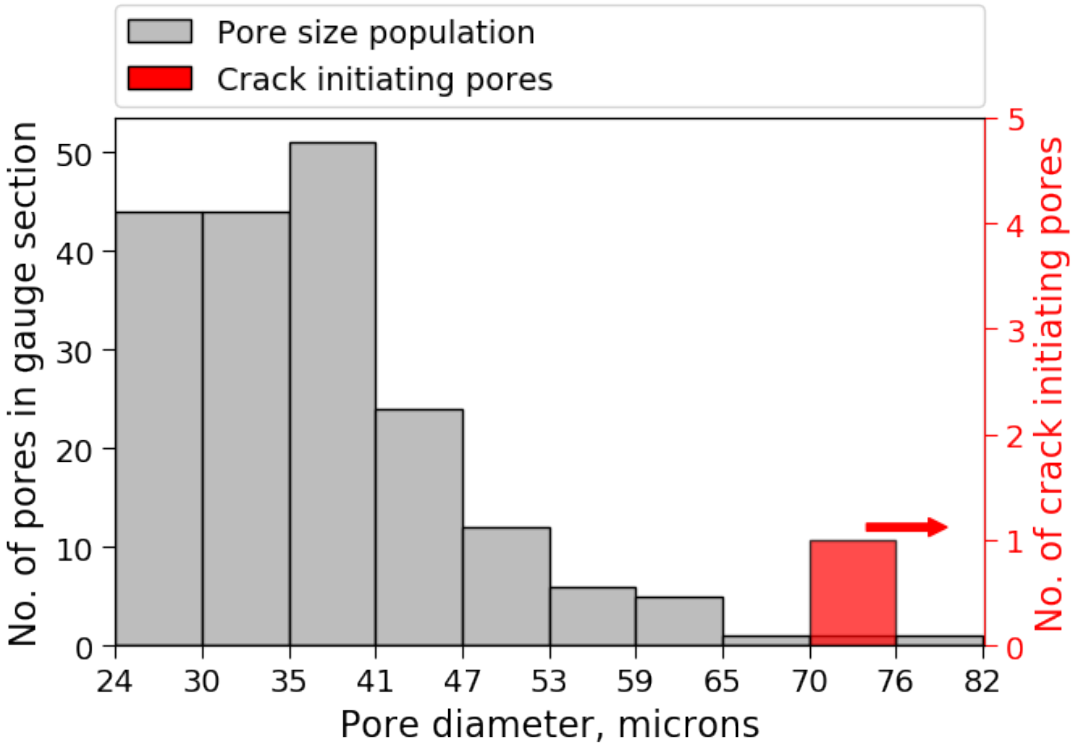

[74]:
```
Avizo_EqDia = []
with open('/Users/akgune/OneDrive - Coventry University/kodlama/EOS/NNS8_rev00/
 ↪Avizo.csv','rb') as f:
    reader = unicodecsv.DictReader(f)
    for row in reader:
        Avizo_EqDia.append(float(row['EqDiameter']))

plt.rcParams.update({'font.size': 14,'figure.dpi':100})
fig, ax = plt.subplots()
counts, bins, patches = ax.hist(Avizo_EqDia, facecolor='#bdbdbd',␣
 ↪edgecolor='black', label='Commerical software')
```

```
ax.hist(NNS8_dPcorr, bins=bins, facecolor='k', edgecolor='black', label='This␣
 ↪work')
meanA = np.mean(Avizo_EqDia)
stdA = np.std(Avizo_EqDia)

df = pd.DataFrame(index = ['Commercial','Thesis'], columns = ['Mean pore␣
 ↪diameter','Standard deviation','Largest pore diameter','Number of pores'])
df.loc['Commercial'] = [meanA,stdA,max(Avizo_EqDia),len(Avizo_EqDia)]
df.loc['Thesis'] = [mean,std,max(NNS8_dPcorr),len(NNS8_dPcorr)]
pd.options.display.float_format = '{:.2f}'.format

display(df.head())

# Set the ticks to be at the edges of the bins.
ax.set_xticks(bins)
# Set the xaxis's tick labels to be formatted with 1 decimal place...
ax.xaxis.set_major_formatter(FormatStrFormatter('%.0f'))
ax.set_xlabel("PORE DIAMETER, microns",family="sans-serif",  fontsize=12)
ax.set_ylabel("# OF PORES IN GAUGE SECTION",family="sans-serif",  fontsize=12)
ax.tick_params(axis='both',which='major', direction="out", bottom="on",␣
 ↪length=6, labelsize=12)
ax.tick_params(axis='both',which='minor', direction="out", bottom="on",␣
 ↪length=6, labelsize=12)
plt.xlim([23.7,86])
plt.ylim([0,60])
plt.legend()
plt.show()
```

	Mean pore diameter	Standard deviation	Largest pore diameter	\
Commercial	40.41	11.05	85.17	
Thesis	37.08	10.30	82.09	

	Number of pores
Commercial	206
Thesis	189

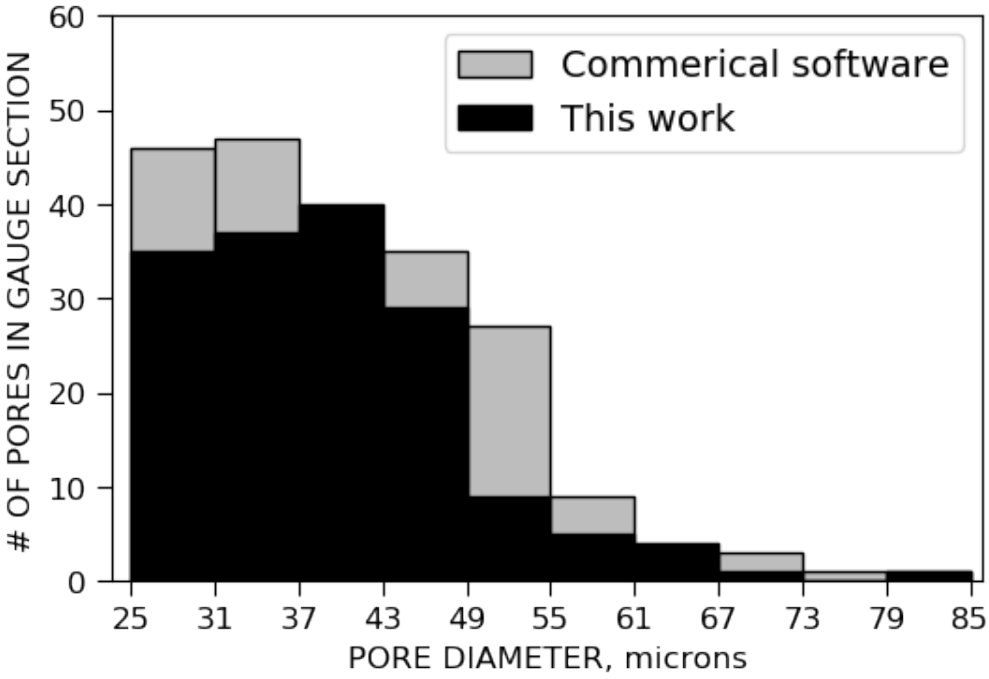
Commerical software
This work
OF PORES IN GAUGE SECTION
PORE DIAMETER, microns
0
10
20
30
40
50
60
25
31
37
43
49
55
61
67
73
79
85

Appendix D

X-ray Computed Tomography Measurements

Introduction

This Appendix provides statistics of pore population measured in each sample. The same chronology presented in main text was followed: first, pore size population is presented as detected in gauge volume of a test sample. Afterwards, this population was categorised as surface pores and embedded pores, which the latter refers to pores 200 μm away from the surface. Then pore size statistics from each category is shown. Finally, number of detected pores along the build direction and spatial location are presented.

NNS Sample no.2

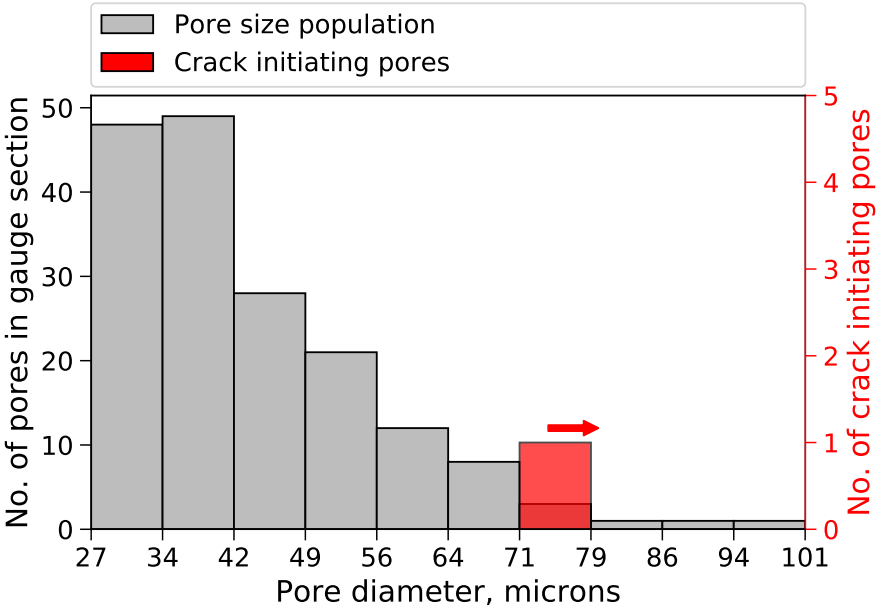

Fig. D.1 Pore size distribution in near-net shape sample no. 2

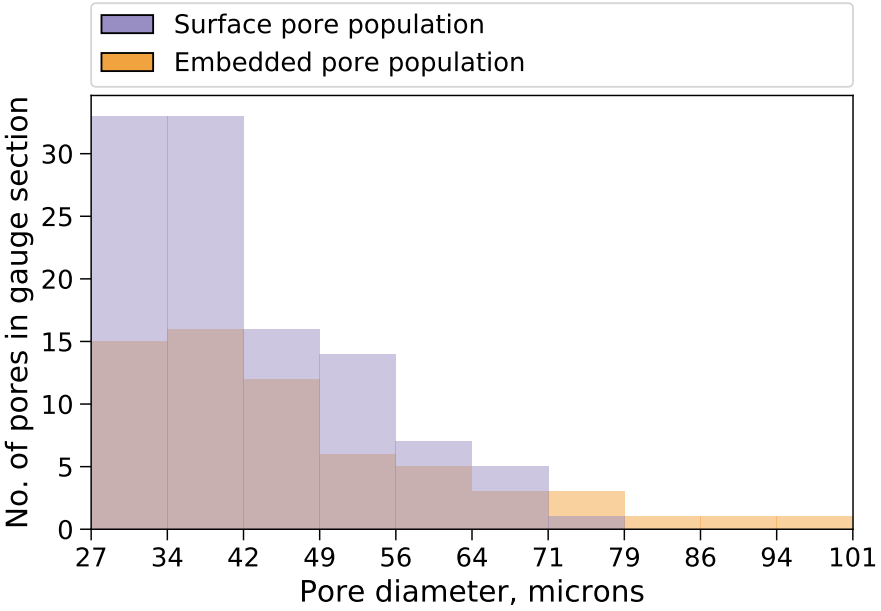

Fig. D.2 Pore size distribution divided according to location in near-net shape sample no. 2

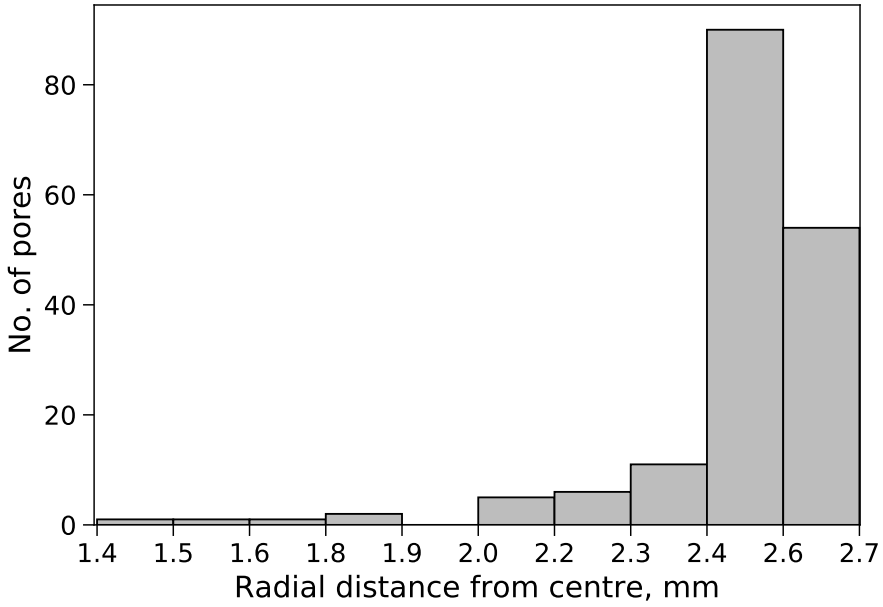

Fig. D.3 Pore spatial distribution in near-net shape sample no. 2

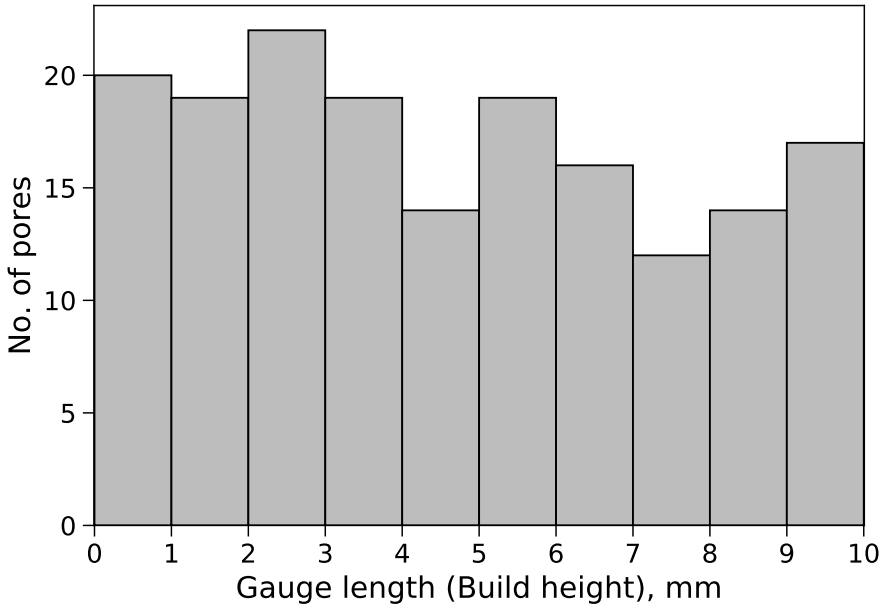

Fig. D.4 Pore distribution along the gauge length in near-net shape sample no. 2

NNS Sample no.3

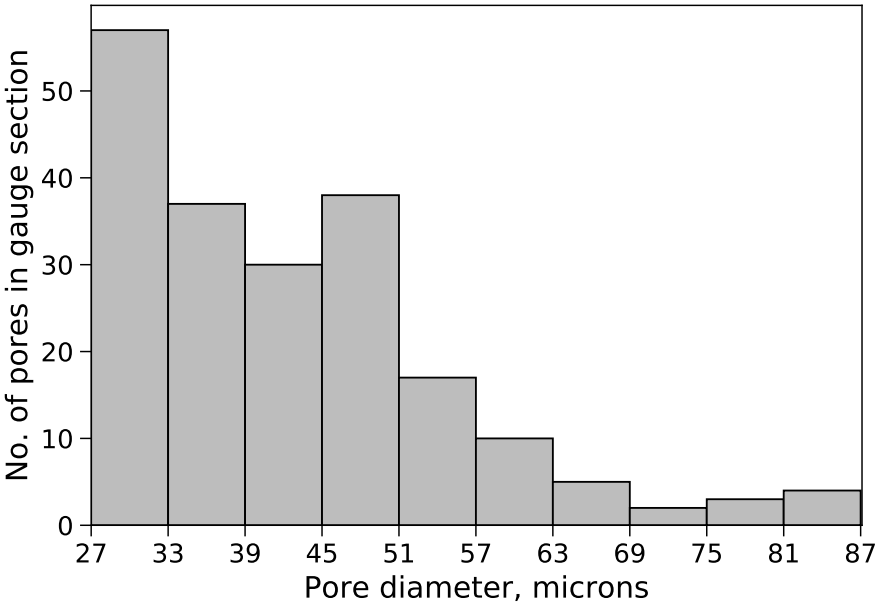

Fig. D.5 Pore size distribution in near-net shape sample no. 3

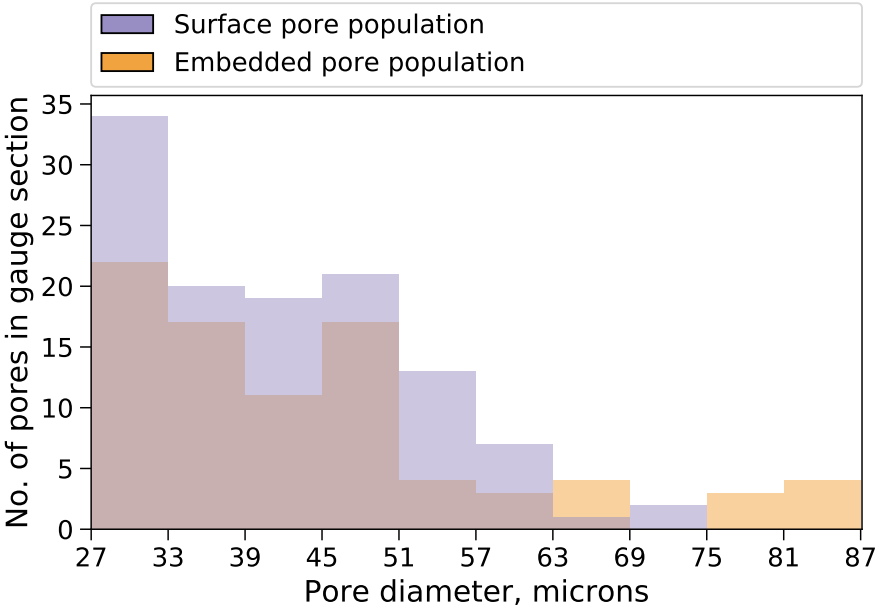

Fig. D.6 Pore size distribution divided according to location in near-net shape sample no. 3

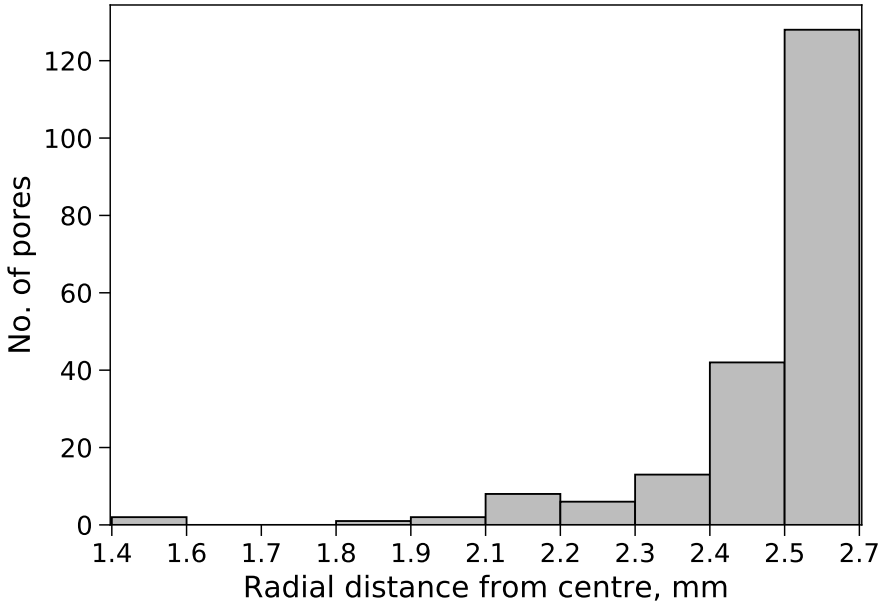

Fig. D.7 Pore spatial distribution in near-net shape sample no. 3

Fig. D.8 Pore distribution along the gauge length in near-net shape sample no. 3

NNS Sample no.4

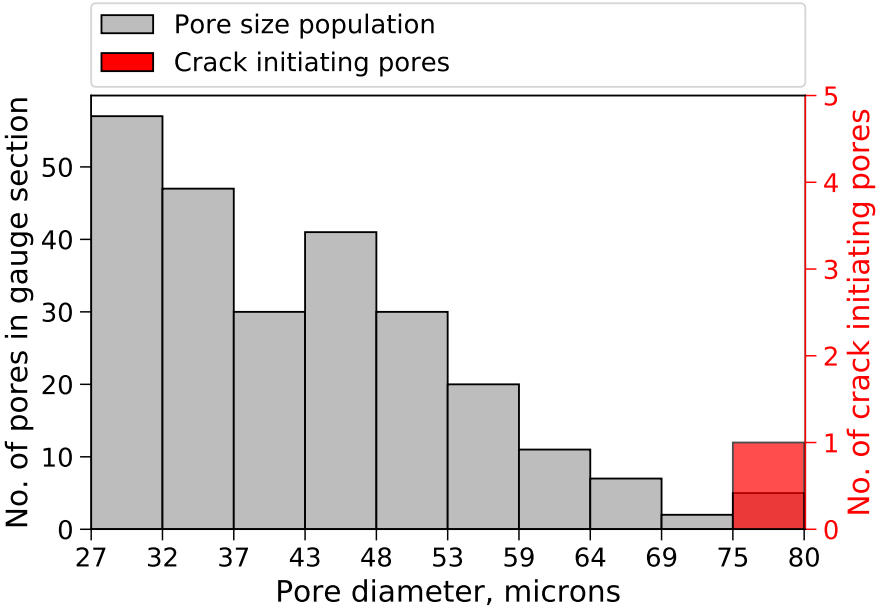

Fig. D.9 Pore size distribution in near-net shape sample no. 4

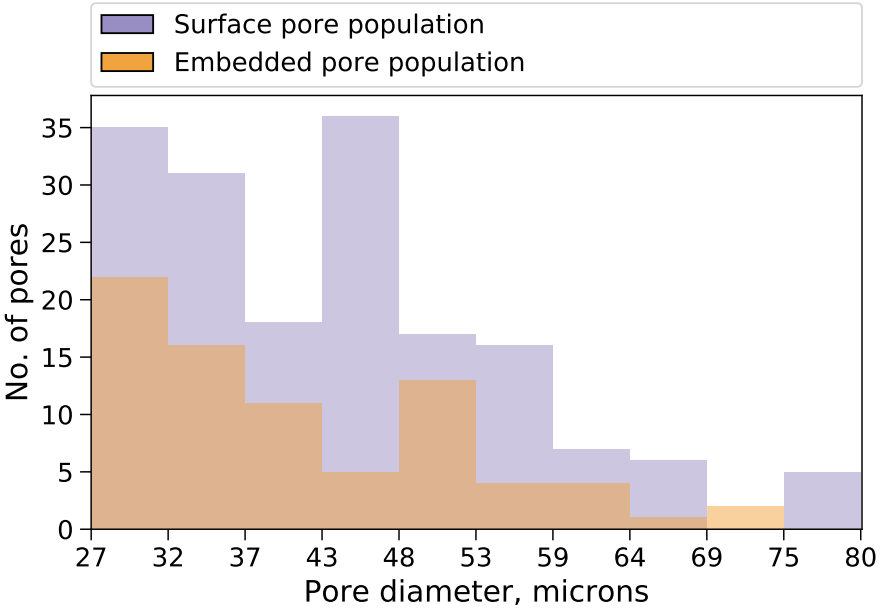

Fig. D.10 Pore size distribution divided according to location in near-net shape sample no. 4

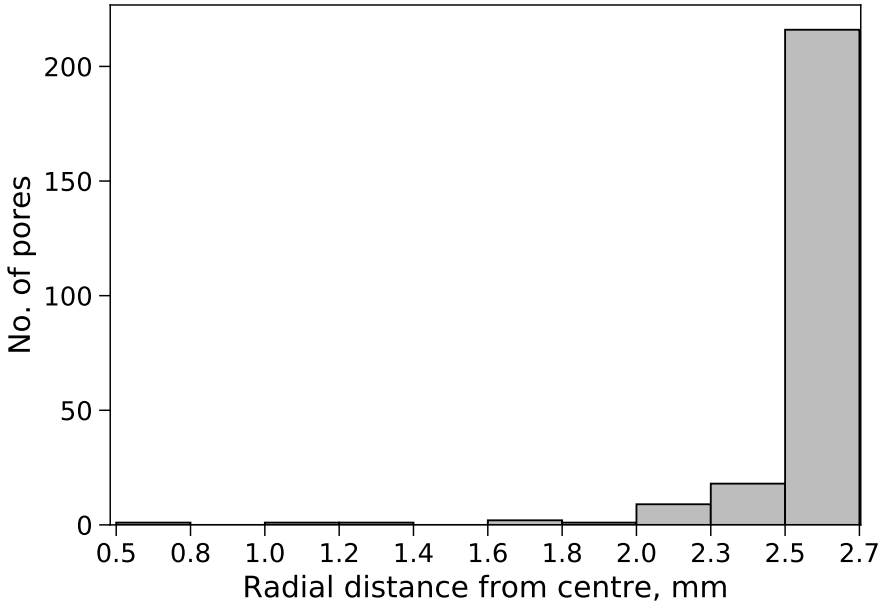

Fig. D.11 Pore spatial distribution in near-net shape sample no. 4

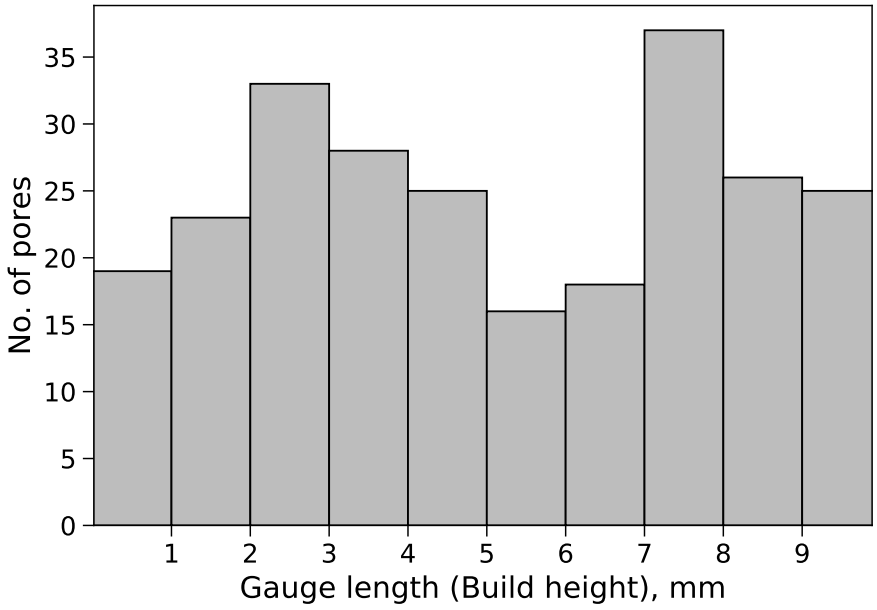

Fig. D.12 Pore distribution along the gauge length in near-net shape sample no. 4

NNS Sample no.5

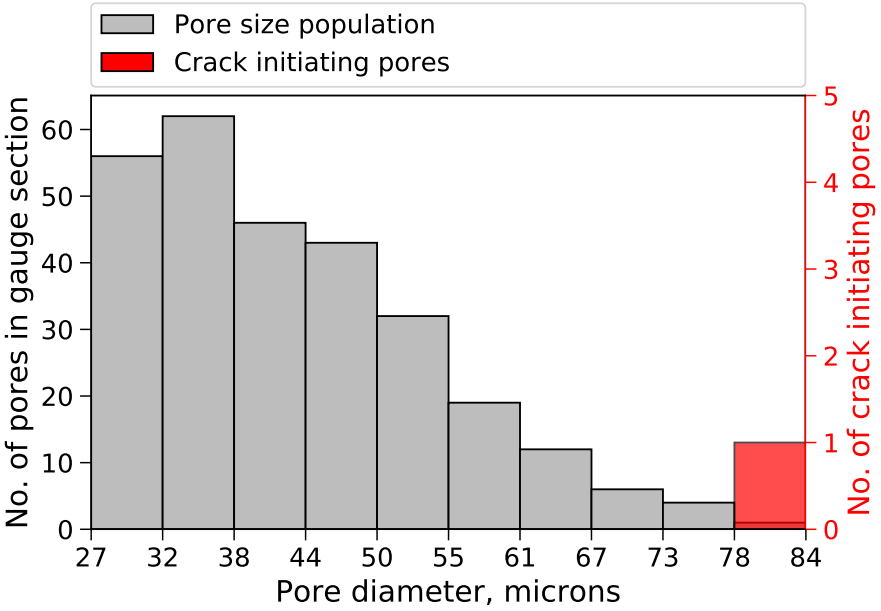

Fig. D.13 Pore size distribution in near-net shape sample no. 5

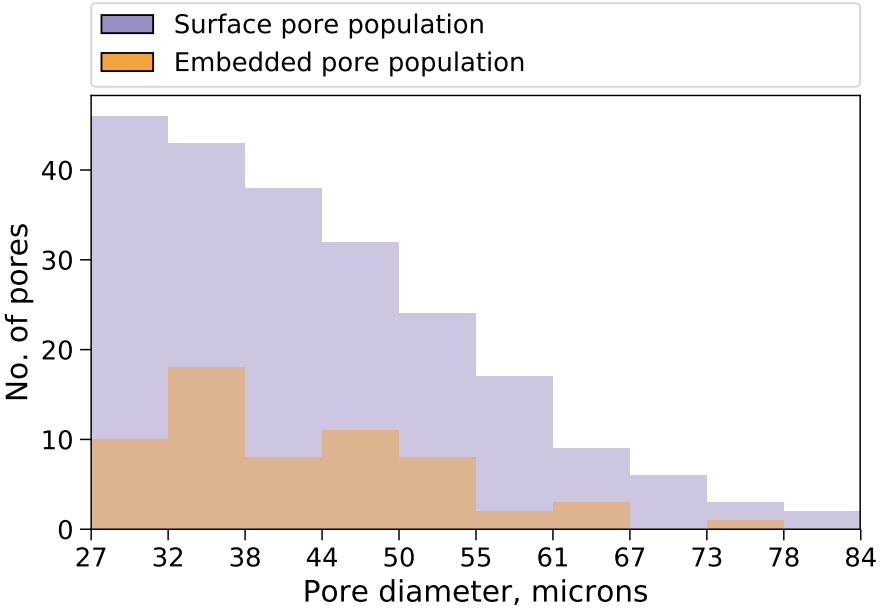

Fig. D.14 Pore size distribution divided according to location in near-net shape sample no. 5

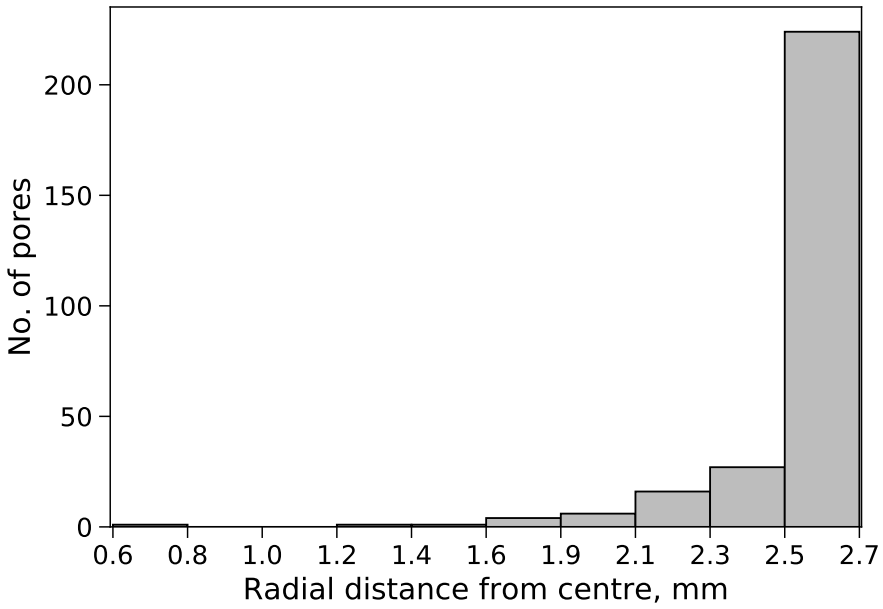

Fig. D.15 Pore spatial distribution in near-net shape sample no. 5

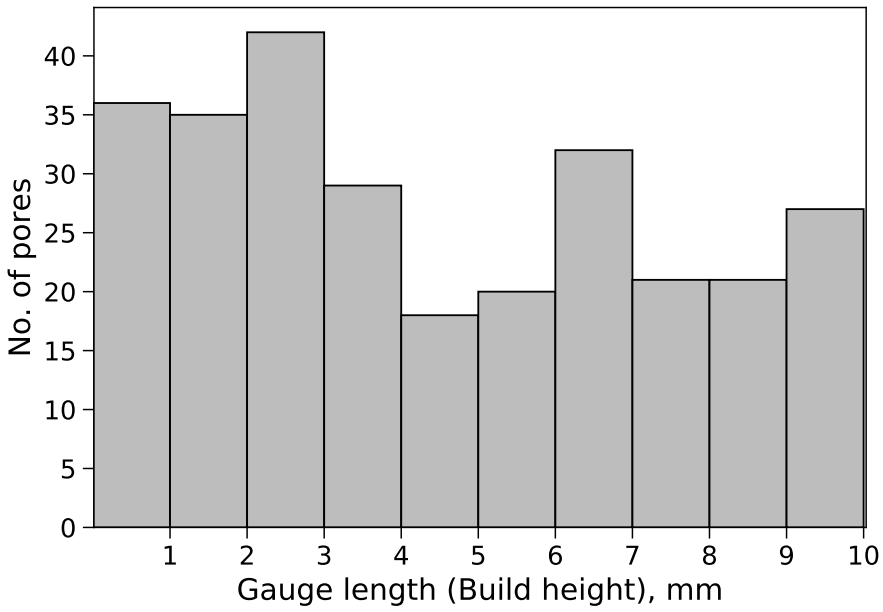

Fig. D.16 Pore distribution along the gauge length in near-net shape sample no. 5

NNS Sample no.6

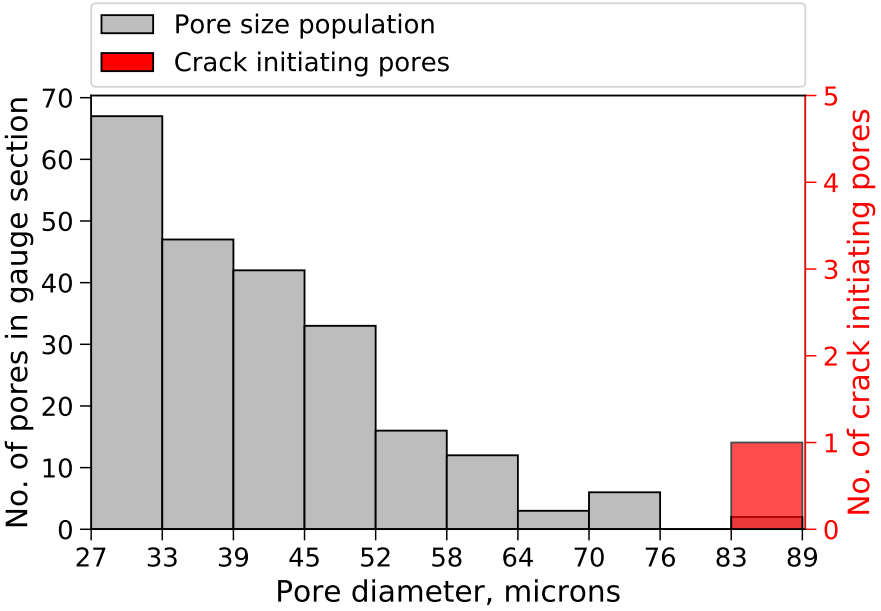

Fig. D.17 Pore size distribution in near-net shape sample no. 6

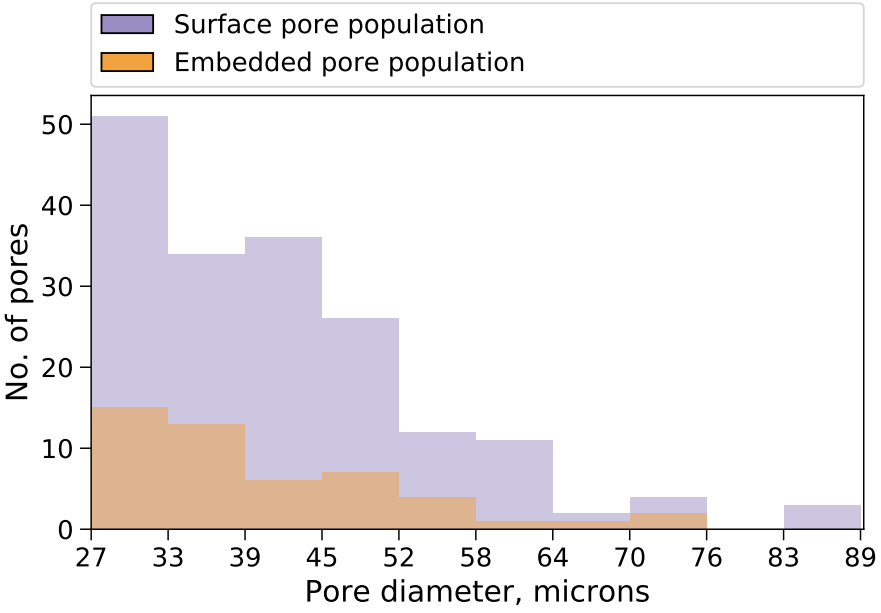

Fig. D.18 Pore size distribution divided according to location in near-net shape sample no. 6

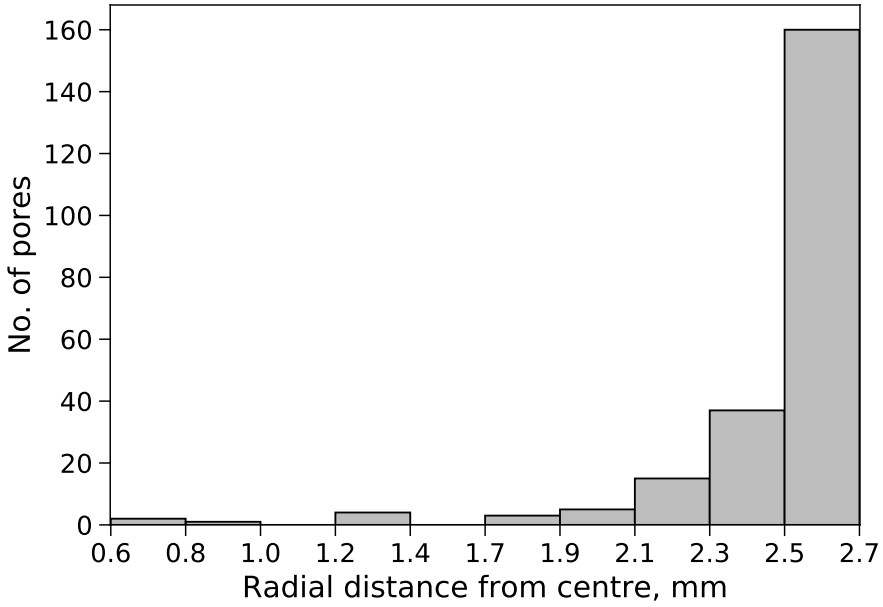

Fig. D.19 Pore spatial distribution in near-net shape sample no. 6

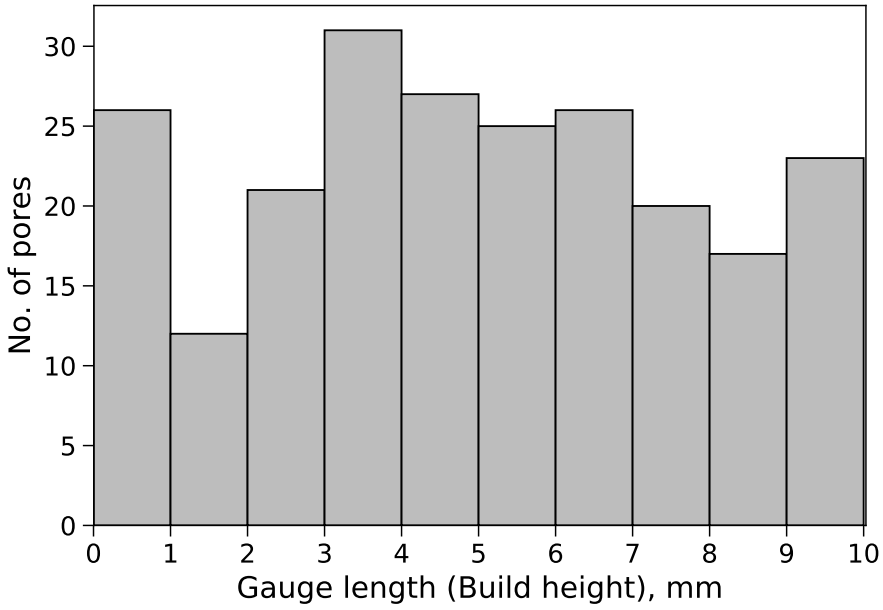

Fig. D.20 Pore distribution along the gauge length in near-net shape sample no. 6

NNS Sample no.7

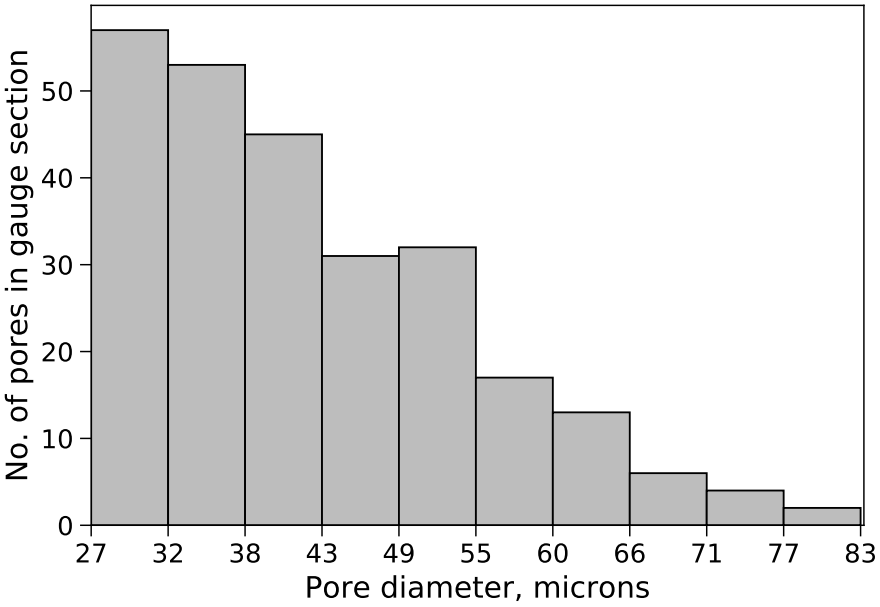

Fig. D.21 Pore size distribution in near-net shape sample no. 7

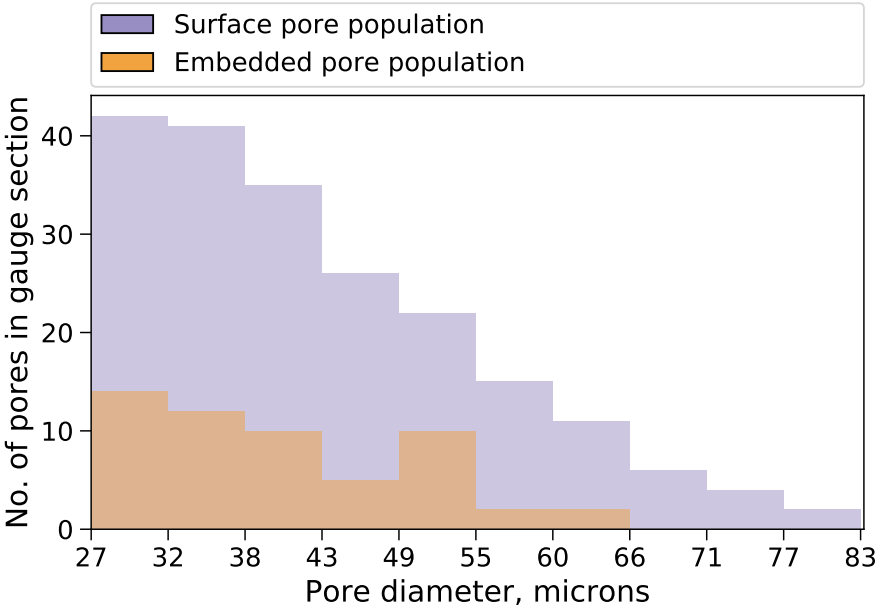

Fig. D.22 Pore size distribution divided according to location in near-net shape sample no. 7

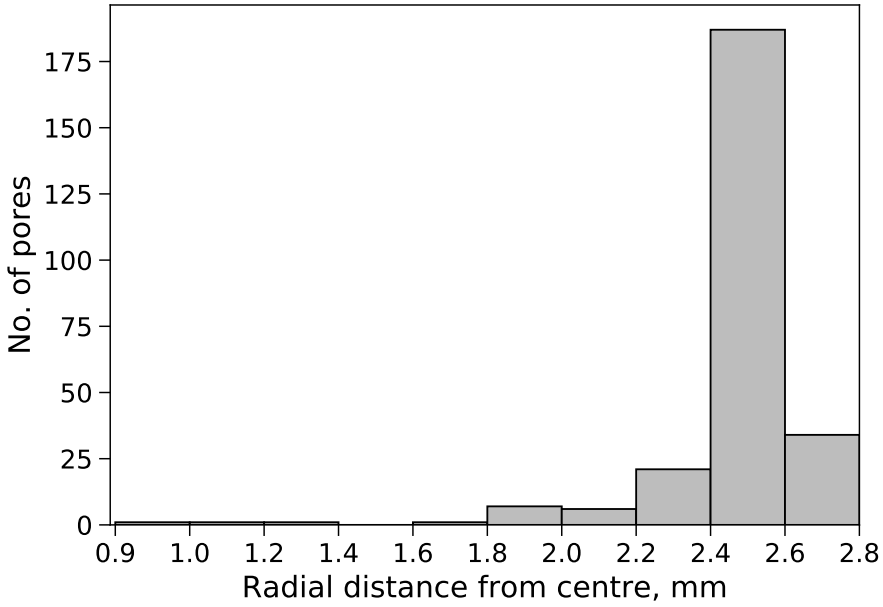

Fig. D.23 Pore spatial distribution in near-net shape sample no. 7

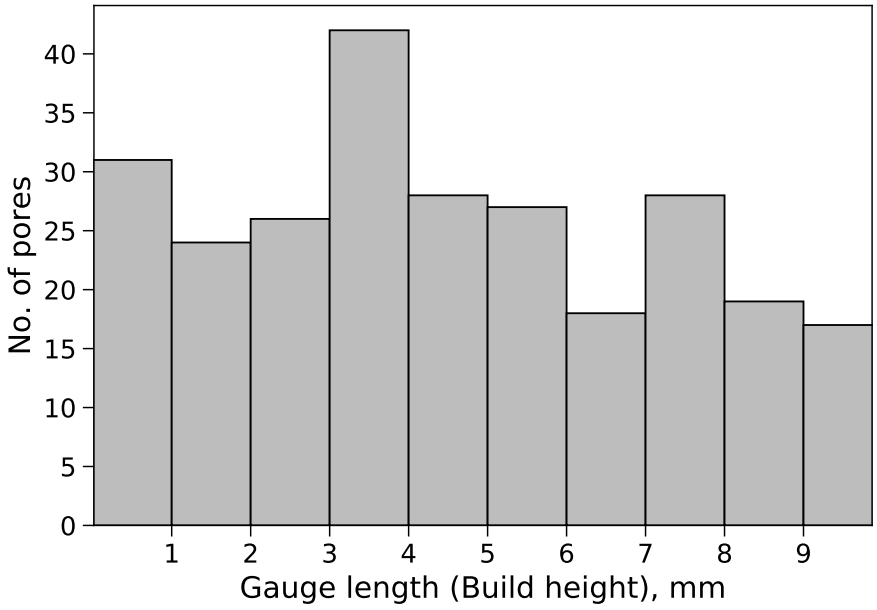

Fig. D.24 Pore distribution along the gauge length in near-net shape sample no. 7

NNS Sample no.10

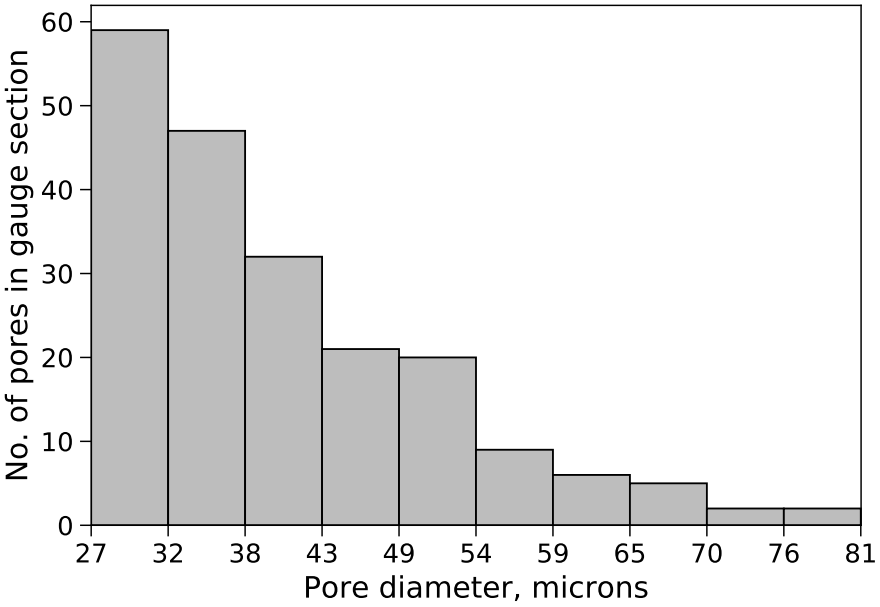

Fig. D.25 Pore size distribution in near-net shape sample no. 10

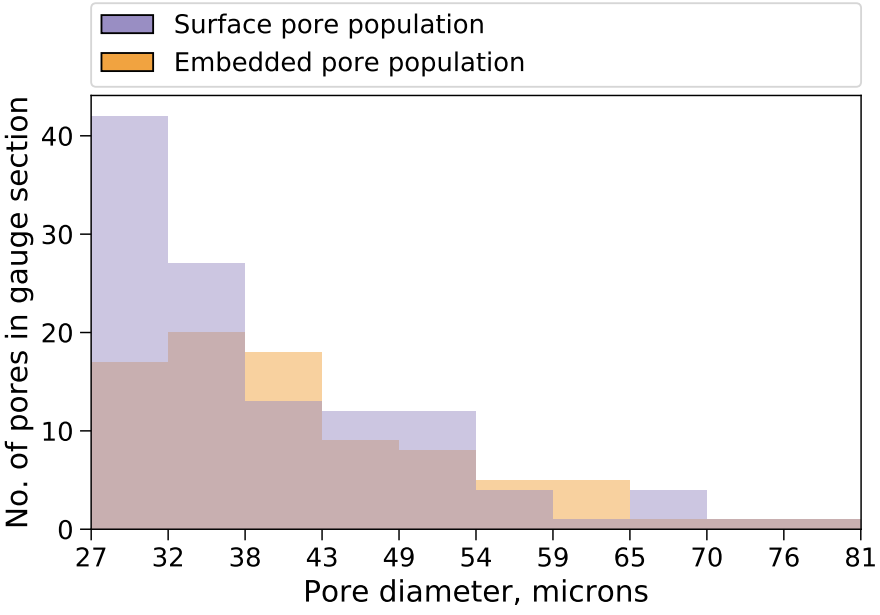

Fig. D.26 Pore size distribution divided according to location in near-net shape sample no. 10

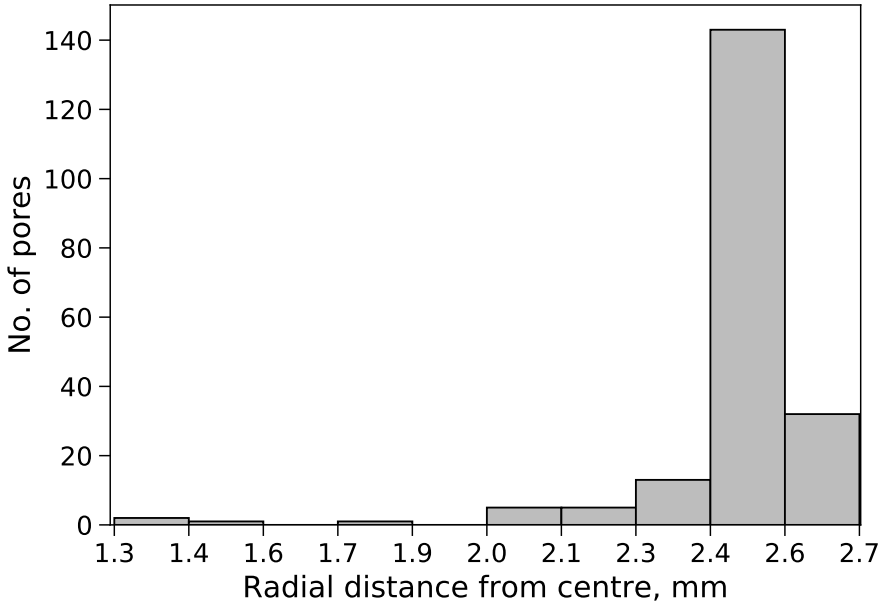

Fig. D.27 Pore spatial distribution in near-net shape sample no. 10

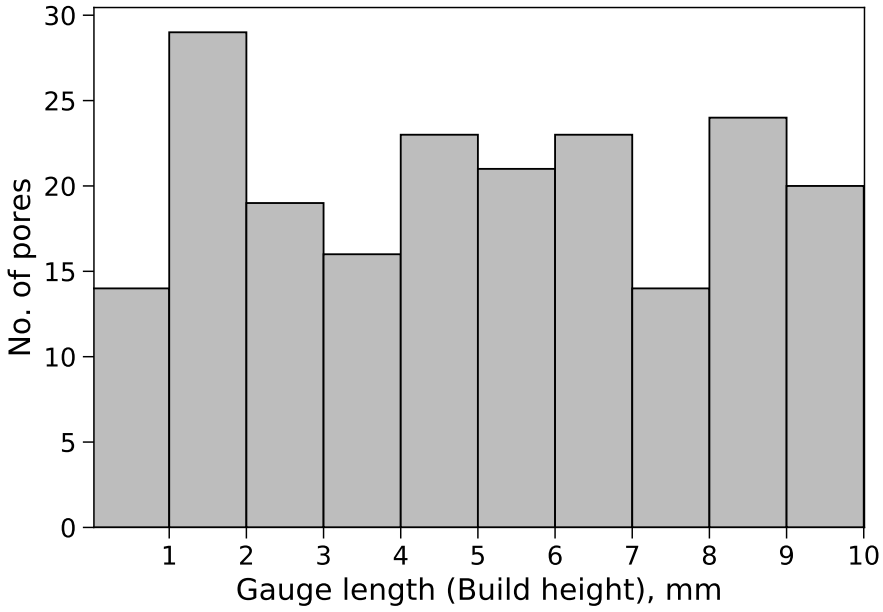

Fig. D.28 Pore distribution along the gauge length in near-net shape sample no. 10

NNS Sample no.12

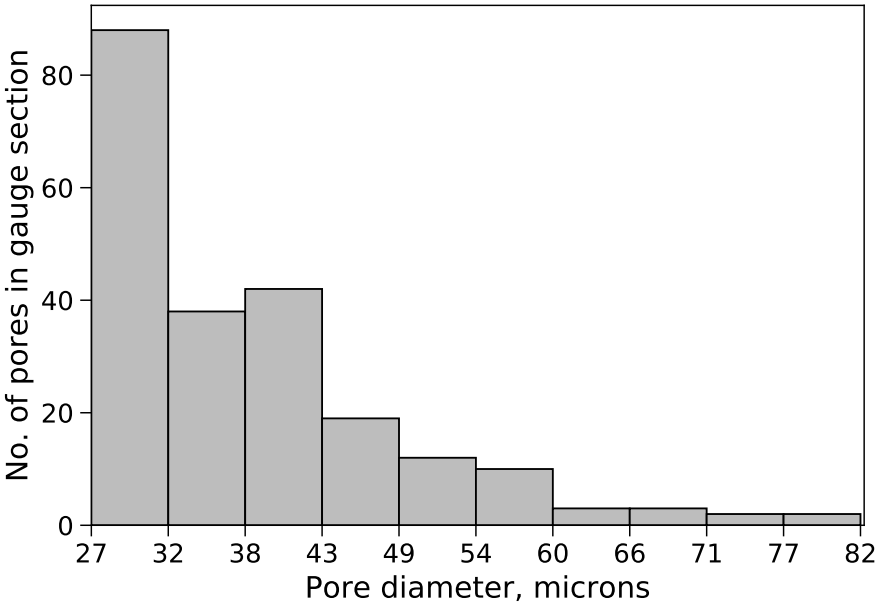

Fig. D.29 Pore size distribution in near-net shape sample no. 12

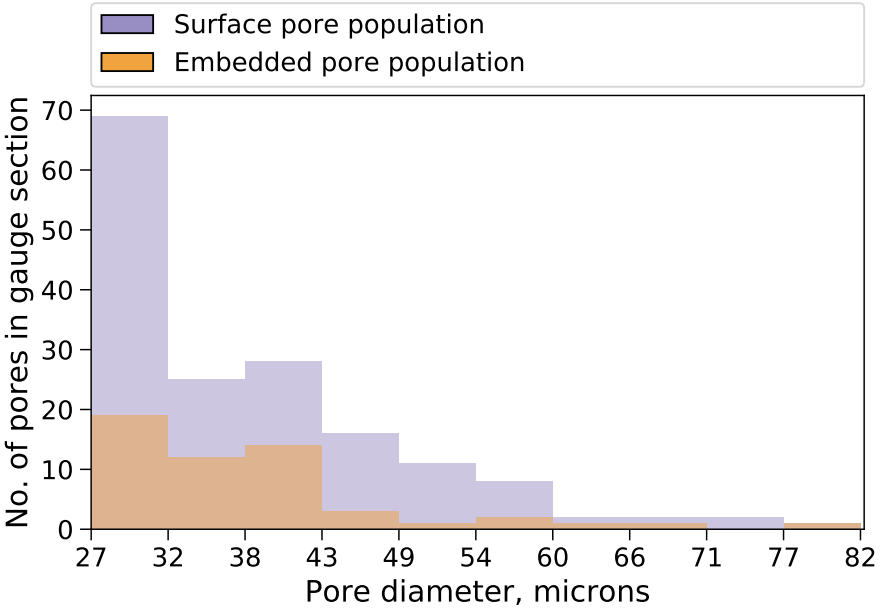

Fig. D.30 Pore size distribution divided according to location in near-net shape sample no. 12

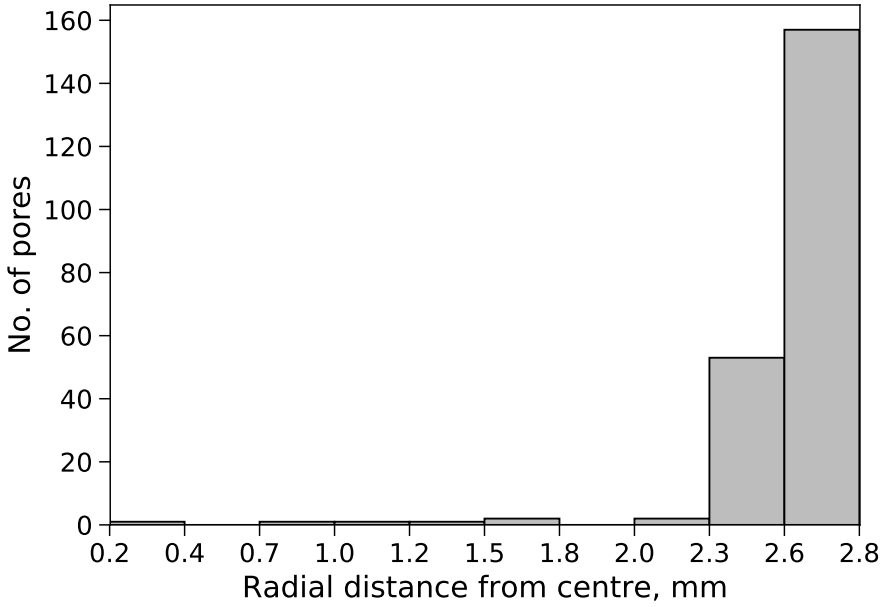

Fig. D.31 Pore spatial distribution in near-net shape sample no. 12

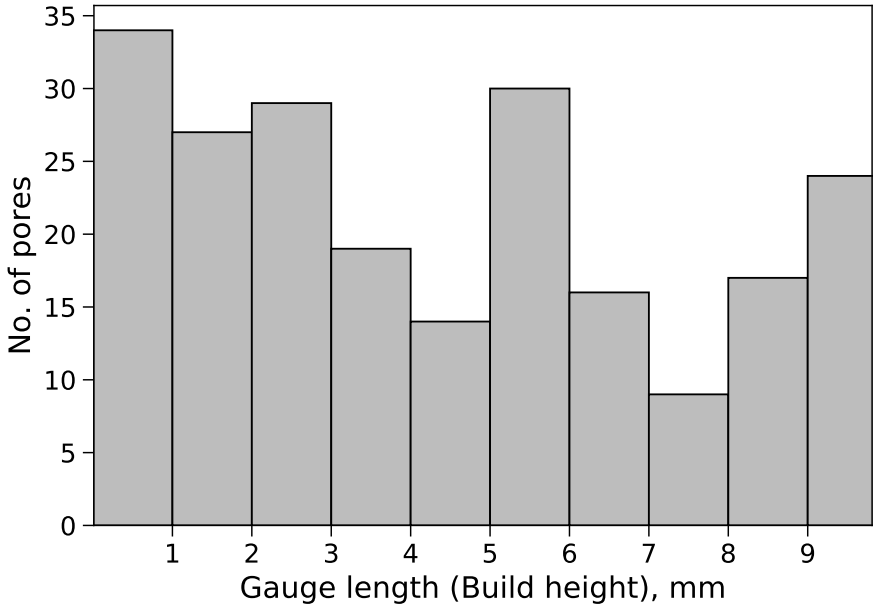

Fig. D.32 Pore distribution along the gauge length in near-net shape sample no. 12